AN INVESTIGATION OF HYDROGEN-RELATED PHENOMENON AND COMPENSATION IN ZnSe GROWN BY MOLECULAR BEAM EPITAXY

DISSERTATION

Submitted to the Eberly College of Arts and Sciences

of

West Virginia University

In Partial Fulfillment of the Requirements for

The Degree of Doctor of Philosophy

by

Zhonghai Yu

Morgantown, West Virginia

June 1996

To my wife, Qingcheng

ACKNOWLEDGMENT

I would like to express my deep gratitude to my research adviser, Dr. Thomas H. Myers, for making this research possible through his guidance, support and encouragement over the past years. I would like to acknowledge Dr. Nancy Giles for her continuous support of this research and helpful discussions. I would like to thank Dr. Larry Halliburton for sharing equipment during my research work. I would also like to thank Dr. Richard Treat for his continuous encouragement. I would like particularly to acknowledge fellow graduate students Steven Buczkowski, Lauren Hirsch, Christina Petcu, Monica Moldovan and Scott Setzler for their participation and contributions to this work. In particular, with Prof. Giles' direction, Christina Petcu assisted me in making preliminary photoluminescence measurements on ZnSe by operating the equipment in Prof. Giles' laboratory, while Monica Moldovan performed all the room temperature PL measurements reported in Ch. 4 and all the PL measurements in Ch. 5, again in Prof. Giles' laboratory. Scott Setzler performed the electron paramagnetic resonance measurements discussed in Ch. 5 under the direction of Prof. Halliburton. Lauren Hirsch performed the FTIR measurements while Steven Buczkowski assisted in all aspects of film growth and performed the Hall measurements on the ZnSe samples. The work from Mr. Carl Weber, Mr. Craig Giffin, and Mr. Tom Milam of the Physics Department Machine Shop is gratefully acknowledged.

I would like to thank Dr. B. R. Cooper and Dr. C. D. Stinespring for serving on my committee. I want to extend my appreciation to the faculty, staff and graduate students of the physics department, especially to Ms. Sherry Puskar, Ms. Tammy Richards, Ms. Siobhan Byrne and Ms. Margaret Mattson, for their help and support during my study and research. I would also like to thank Qingcheng Zhu for her help in preparing the references and index of this dissertation.

The work presented in this dissertation was supported by West Virginia / NSF EPSCoR program and II-VI, Inc., (Saxonburg, PA).

TABLE OF CONTENTS

Page

ACKNOWLEDGMENT iii
TABLE OF CONTENTS v
LIST OF TABLES vii
LIST OF FIGURES viii

Chapter

I. INTRODUCTION 1
- 1.1 Overview 1
- 1.2 ZnSe: Basic Properties and Applications 4
- 1.3 Problems with ZnSe 11
  - 1.3.1 Substrate Issues 12
  - 1.3.2 ZnSe Growth 15
  - 1.3.3 Doping and Compensation in ZnSe 20
  - 1.3.4 Defect Density 31
  - 1.3.5 Ohmic Contacts 37
- 1.4 Statement of the Problem 37

II. GROWTH AND CHARACTERIZATION 41
- 2.1 MBE System 41
  - 2.1.1 Chamber and Source Flange Design 43
  - 2.1.2 Pumping System 48
  - 2.1.3 Substrate Manipulation 54
  - 2.1.4 Nitrogen Source and Hydrogen Source 56
- 2.2 Characterization 61
  - 2.2.1 *In-situ* Techniques 62
    - 2.2.1.1 Reflection High Energy Electron Diffraction (RHEED) 62
    - 2.2.1.2 Mass Spectroscopy 71
  - 2.2.2 *Ex-situ* Techniques 72
    - 2.2.2.1 Photoluminescence (PL) 72
    - 2.2.2.2 Fourier Transform Infrared (FTIR) Spectroscopy 78
    - 2.2.2.3 Secondary Ion Mass Spectrometry (SIMS) 80
    - 2.2.2.4 Optical Microscopy 81
    - 2.2.2.5 Other Techniques 83
- 2.3 Typical Growth Sequence 84

III. REDUCTION OF TWIN-RELATED DEFECTS....88
3.1 Substrate Cleaning Using Atomic Hydrogen....88
3.2 Experimental Procedures....90
3.3 Results....91
3.3.1 RHEED....91
3.3.2 UV Fluorescent Microscopy of ZnSe....91
3.3.3 Photoluminescence....97
3.4 Discussion....99
3.4.1 Defect Reduction by Atomic Hydrogen Cleaning of Substrate....99
3.4.2 Effect of Twin-related Defects on Nitrogen Doping....104
IV. HYDROGEN-RELATED PHENOMENON....107
4.1 Role of Hydrogen in Semiconductors....107
4.2 Experimental Procedures....109
4.3 Results....111
4.3.1 Reflection High Energy Electron Diffraction....111
4.3.2 Secondary Ion Mass Spectrometry....112
4.3.3 Fourier Transform Infrared Spectroscopy....117
4.3.4 Photoluminescence....122
4.3.5 Hall Measurements....128
4.4 Discussion....129
4.4.1 Hydrogen Incorporation in ZnSe....129
4.4.2 Nitrogen Compensation in ZnSe by Hydrogen....132
V. ADDITIONAL FTIR, PL AND EPR STUDIES: IMPLICATIONS FOR COMPENSATION PROCESSES....137
5.1 Evidence of Compensation Sources....137
5.1.1 FTIR Measurements....137
5.1.2 PL Measurements....142
5.1.3 EPR Measurements....144
5.2 Discussion of Compensation Processes in ZnSe....147
VI. CONCLUSIONS....150

REFERENCES....153
APPENDIX A: List of Growth Conditions for ZnSe Samples....164
ABSTRACT....168

ABSTRACT

Both compensation and hydrogen-related phenomenon in ZnSe grown by MBE have been systematically investigated in this study. Atomic hydrogen is demonstrated to effectively clean GaAs substrates for subsequent growth of ZnSe by molecular beam epitaxy. Significant reduction of micro-defects in both undoped and nitrogen doped ZnSe is achieved using atomic hydrogen cleaning of GaAs substrate prior to ZnSe growth without any other treatment. The density of stacking faults in ZnSe is less than $1x10^4$ cm^{-2} in layers grown with atomic hydrogen cleaning, while it is greater than $1x10^7$ cm^{-2} in layers grown with conventional thermal cleaning. Optical microscopy is shown to be a useful technique to image non-radiative defects such as stacking faults. Low-temperature photoluminescence (PL) spectra of undoped ZnSe are dominated by excitonic transitions for the low dislocation density samples in contrast to the high level of defect-related emission from high defect density samples. Similar PL and Hall measurements for nitrogen-doped ZnSe layers with comparable nitrogen concentrations grown with both cleaning procedures indicate that compensation of nitrogen doping in ZnSe is not affected by the presence of micro-defects. Hydrogen is incorporated into ZnSe during MBE growth using a thermally-cracked atomic hydrogen source. It is found that the hydrogen incorporation is strongly nitrogen-related, and the incorporation is significant only when both atomic hydrogen and atomic nitrogen are present during growth. The observation of vibrational absorption bands using Fourier transform infrared spectroscopy in ZnSe:N,H samples indicates the presence of N-H bonding in these layers. Absorption bands occurring at 3193 cm^{-1} and 783 cm^{-1} correspond to the stretching mode and wagging mode of the N-H bond. The isotope shift due to exchanging hydrogen with deuterium is also observed, resulting in an absorption band at 2368 cm^{-1}. This is in excellent agreement with the predictions of the harmonic oscillator approximation. The

low incorporation of molecular hydrogen in nitrogen-doped ZnSe grown by MBE implies that the hydrogen is not the source of nitrogen compensation in ZnSe grown by conventional MBE technique. A substitutional nitrogen absorption band is observed for the time in as-grown ZnSe materials. The integrated absorption for the substitutional nitrogen signal does not linearly increase with the nitrogen concentration in the layer as measured by SIMS. The discrepancy implies that a very large amount of incorporated nitrogen is either not in the substitutional site or is in another charge state which does not contribute to the p-type doping in ZnSe. A Se vacancy signal is observed by electron paramagnetic resonance measurement in both undoped and nitrogen-doped ZnSe. The Se vacancies are estimated to be in the range of 10^{17} to 10^{18} cm^{-3}. PL result indicates that a donor at a level of as deep as 0.3 eV possibly exists in heavily nitrogen-doped ZnSe. It is suggested that the nitrogen compensation in ZnSe can be from Se vacancy-related defects at doping levels lower than 10^{18} cm^{-3}, while it can be limited by the nitrogen solubility at levels greater than 10^{18} cm^{-3}.

APPROVAL OF THE EXAMINING COMMITTEE

Bernard R. Cooper, Ph. D.	Date
Nancy C. Giles, Ph. D.	Date
Larry E. Halliburton, Ph. D.	Date
Charter. D. Stinespring, Ph. D.	Date
Thomas H. Myers, Ph. D. (Chairman)	Date

LIST OF TABLES

Page

Table 1.1 Fundamental properties of ZnSe 8

Table 1.2 II-VI laser diode development milestones........9

Table 2.1 Vapor pressure, oven temperature, and beam equivalent pressure (BEP) of typical source materials used in MBE growth........49

Table 2.2 Vacuum pumps used in the MBE system at WVU 53

Table 2.3 Mass current of residual gases in vacuum system after bakeout........53

Table 2.4 Typical PL signals observed in ZnSe........74

Table 2.5 Binding energies for acceptors in ZnSe grown by MBE........75

Table 2.6 SIMS measurement conditions used for ZnSe 81

Table 2.7 Specifications of GaAs substrate used for ZnSe growth........87

Table 2.8 GaAs substrate etching procedure for ZnSe growth 87

Table 4.1 Samples grown with various hydrogen/nitrogen configurations........111

Table 4.2 Hydrogen, deuterium and nitrogen concentrations in ZnSe for various growth conditions........116

LIST OF FIGURES

Page

Fig. 1.1 Lattice structure of zincblende ZnSe. 5

Fig. 1.2 Energy band structure of ZnSe (Taken from Ref. 2). 7

Fig. 1.3 Schematic diagram of a II-VI laser diode structure involving ZnMgSSe by Sony (Taken from Luo *et al.*[21]). 10

Fig. 1.4 Lattice constant *vs*. bandgap energy for a variety of II-VI semiconductors. Lattice constant of GaAs is indicated for the lattice matching with ZnSe. 13

Fig. 1.5 Growth matrix of T_G and beam-equivalent pressure ratio BPR of Zn to Se, which provides growth reference for Zn-stabilized or Se-stabilized growth, and spotty or streaky pattern from the growth surface (Taken from DePuydt *et al.*[74]). 16

Fig. 1.6 Typical PL spectra of ZnSe:N with various doping level at 10 K (a) [N] < $6x10^{17}$ cm^{-3}, (b) [N] = $1.5x10^{18}$ cm^{-3}, and (c) [N] = $1.3x10^{19}$ cm^{-3} (Taken from Qiu *et al.*[85]). 23

Fig. 1.7 Se vacancy complex in ZnSe:N involving the association of the V_{Se} double donor and a nitrogen acceptor (Taken from Hauksson *et al.*[13]). 25

Fig. 1.8 Model for DAP recombination process in nitrogen-doped ZnSe involving both a shallow donor (26 meV) and a deep donor (44 meV). The nitrogen acceptor is labeled N (Taken from Hauksson *et al.*[13]). 26

Fig. 1.9 Lattice relaxation induced compensating donor in ZnSe:N (a) ideal zincblende lattice for ZnSe, (b) double-broken-bond (DBB) state resulting from the breaking of two Zn-Se bonds and the formation of a Se-Se bond (Taken from Park and Chadi[18]). 29

Fig. 1.10 SIMS profile of a ZnSe:N structure grown by GSMBE, indicating the nitrogen doping related hydrogen incorporation (Taken from Ho *et al.*[34]). 32

Fig. 1.11 Schematic of three dimensional arrangement of defects in a ZnSe laser structure. S1 and S2 are stacking faults originated at II-VI/GaAs interface, T1 and T2 are threading dislocations bound to stacking faults, and D1 and D2 are dislocation network patches nucleated at threading dislocations and developed into the active layer (Taken from Hua *et al.*[62]). 34

Fig. 2.1 Mass spectra of (a) an unbaked vacuum system, and (b) a vacuum

system with the signature of an air-leak. 42

Fig. 2.2 Front view of the MBE system used in this study. 44

Fig. 2.3 Schematic diagram of an MBE system. In addition to the main chamber, source flange, load-lock and pumping system, other important components include the temperature control unit, the vacuum control unit and the characterization unit. 45

Fig. 2.4 Diagram of an MBE source flange (a) a cross sectional view with the cooling shroud for ovens also shown, and (b) a bottom view where a maximum of seven ovens can be installed. 47

Fig. 2.5 Operating pressure range for a variety of vacuum pumps. 50

Fig. 2.6 Schematic diagram of substrate cooling shroud. 52

Fig. 2.7 Assembly diagram of substrate block. 55

Fig. 2.8 Emission spectrum of rf plasma atomic/radical nitrogen source. 58

Fig. 2.9 Cracking efficiency of the atomic hydrogen source (Taken from Ref. 124). 60

Fig. 2.10 Schematic diagram of Ewald sphere intersecting with a 2-D reciprocal lattice for a perfect two-dimensional surface. (Taken from Lagally in Ref. 127). 63

Fig. 2.11 Schematic diagram of a GaAs (100)-c(4x4) surface reconstruction (a) with additional 25% As coverage, (b) with additional 50% As coverage (Taken from Ref. 9). 65

Fig. 2.12 Schematic diagram of RHEED setup in MBE system. 67

Fig. 2.13 Schematic diagram of QMS system. 70

Fig. 2.14 Schematic of possible PL recombination processes. 73

Fig. 2.15 Schematic of photoluminescence measurement setup. 76

Fig. 2.16 Schematic of a Hall measurement setup. 82

Fig. 3.1 RHEED pattern of (100) GaAs substrate in both [100] and [110] azimuth: (a) as-etched surface; (b) after conventional thermal cleaning; (c) after atomic hydrogen cleaning. 92

Fig. 3.2 Optical fluorescence micrograph of undoped ZnSe/GaAs grown (a) with conventional thermal cleaning, (b) with atomic hydrogen cleaning. The micrographs represent an area of 125 μm by 88 μm. 93

Fig. 3.3 Optical fluorescence micrograph of nitrogen doped ZnSe/GaAs grown (a) with conventional thermal cleaning, (b) with atomic hydrogen cleaning. The micrographs represent an area of 125 μm by 88 μm. 95

Fig. 3.4 Atomic force images of ZnSe/GaAs grown (a) with conventional thermal cleaning, (b) with atomic hydrogen cleaning. The micrographs represent an area of 3 μm by 3 μm. 96

Fig. 3.5 Low-temperature photoluminescence spectra of undoped ZnSe/GaAs grown (a) with conventional thermal cleaning, (b) with atomic hydrogen cleaning (intensities shown are enhanced by factor of two). 98

Fig. 3.6 RHEED of ZnSe grown on GaAs after the growth of (a) 0 s, (b) 10 s, (c) 30 s, (d) 1 min., (e) 2 min., and (f) 5 min. The electron beam is in the [110] azimuth. 102

Fig. 3.7 Low-temperature photoluminescence spectra of nitrogen-doped ZnSe/GaAs grown (a) with conventional thermal cleaning, (b) with atomic hydrogen cleaning. The observed shift is due to different nitrogen concentration in the samples. 105

Fig. 4.1 Secondary ion mass spectrometry depth profile of nitrogen-doped ZnSe. The drop in nitrogen concentration near the ZnSe/GaAs interface corresponds to the undoped ZnSe buffer layer..113

Fig. 4.2 Secondary ion mass spectrometry depth profile of (a) ZnSe:N,H, (b) ZnSe:N,D. The drop in concentrations near the ZnSe/GaAs surface corresponds to the undoped ZnSe buffer layer while the drop near the sample surface in (a) corresponds to switching from atomic to molecular nitrogen during the growth. 114

Fig. 4.3 Fourier transform infrared spectroscopy spectrum of ZnSe:N,H. The absorption bands at 783 cm^{-1} and 3193 cm^{-1} correspond to the N-H bond wagging mode and stretching mode, respectively................................119

Fig. 4.4 Fourier transform infrared spectroscopy spectrum of ZnSe:N,D. The absorption band at 2368 cm^{-1} corresponds to the stretching mode of N-D bond...120

Fig. 4.5 Photoluminescence spectra of ZnSe:N (dashed line) and ZnSe:N,H (solid line). The PL feature in ZnSe:N is a typical lineshape of

heavily nitrogen-doped ZnSe, and the new feature (representing a deeper level) in ZnSe:N,H is hydrogen related. 123

Fig. 4.6 Low-temperature PL spectrum of ZnSe grown under an atomic hydrogen flux.. 124

Fig. 4.7 Photoluminescence spectrum of ZnSe and ZnSe:H at room-temperature. 126

Fig. 4.8 Photoluminescence spectrum of ZnSe:N_2 at low-temperature. The strong nitrogen acceptor bound exciton and DAP feature indicate the nitrogen incorporation in the sample. 127

Fig. 4.9 Model of hydrogen bonding in ZnSe:N,H (a) center-bonding site, (b) anti-bonding site (Taken from Wolk *et al.*(104)). 133

Fig. 4.10 Secondary ion mass spectrometry depth profile of ZnSe:N,D_2. The level of deuterium indicates that the hydrogen incorporation in molecular form is significantly lower than in atomic form. 135

Fig. 5.1 Room-temperature FTIR spectrum of (a) ZnSe:N, (b) ZnSe:N and (c) ZnSe:N,D. Spectra are arbitrarily shifted along the absorbance axis for display. 139

Fig. 5.2 Integrated absorption *vs.* nitrogen concentration in ZnSe:N. Dots represent experimental values while the line is a projection for a linear increase in integrated absorption as nitrogen concentration increases. 140

Fig. 5.3 Photoluminescence spectra of ZnSe:N for (a) above bandgap excitation (325 nm line) at 4.8 K, (b) below bandgap excitation (457 nm line) at 4.8 K and (c) below bandgap excitation (457 nm line) at 85 K. 143

Fig. 5.4 Electron paramagnetic resonance signal of ZnSe samples. Samples 9601 and 9602 are undoped, while 9603 and 9609 are nitrogen-doped. The Se vacancies are estimated to be $2x10^{18}$ cm^{-3} and $7x10^{17} cm^{-3}$ in samples 9602 and 9603, respectively. 146

CHAPTER I

INTRODUCTION

1.1 Overview

Zinc selenide is a II-VI compound semiconductor with the zincblende crystal structure and a direct bandgap.[1,2] The II-VI semiconductors could form the basis for a variety of efficient light-emitting devices spanning the entire range of the visible spectrum since their direct bandgaps range from the infrared to the ultraviolet.[3] Research on the wide bandgap II-VI compound semiconductors began in the early 1960's alongside the initial developments in semiconductor optoelectronics. Despite the fact that the direct-bandgap II-VI semiconductors offered the most promise for realizing visible laser diodes (LD) and efficient light-emitting-diode (LED) displays, major obstacles soon emerged with these materials. These can be broadly defined in terms of the structural and electronic quality of the material.[3-7] In contrast, over the past thirty years development of the narrower gap III-V semiconductors, such as gallium arsenide and related III-V alloys, has progressed quite rapidly. The infrared semiconductor laser, utilizing III-V semiconductor materials, provides the optical source for fiber communication link and compact-disk players, and is one of the essential components for today's information technology.[8] In the development of III-V compound semiconductor applications, modern growth techniques using non-equilibrium epitaxy methods such as molecular beam epitaxy (MBE) and metalorganic chemical vapor deposition (MOCVD) were developed and produced spectacular success with the III-V compounds.[9] These new growth methods were also applied to the studies of II-VI compounds.[9,10]

Among the traditional problems encountered with II-VI semiconductors, one of the most troubling was the inability to successfully produce both n-type and p-type doping.[3,4] It is typically easy to produce one type of doping, and extremely difficult to

achieve the other. The problem is a fundamental one in wide bandgap compound semiconductors, which tend to be natural "semi-insulators" because of the strong polar nature in their bond formation.[2] Although it is a simple task to incorporate donor-like substitutional impurities into ZnSe, useful p-type doping proved extremely difficult. The breakthrough for p-type doping in ZnSe occurred when nitrogen was used as the dopant through a plasma source in 1990.[11,12]

Although the levels of p-type doping obtainable in ZnSe using atomic nitrogen is sufficient to demonstrate light emitting devices, it has proven difficult to increase net carrier concentration beyond 1×10^{18} cm^{-3}.[3,4] The doping level actually decreases when the nitrogen concentration is further increased due to compensation in the material. The mechanism of compensation in ZnSe is still not fully understood although several models have been proposed.[13-19] It is generally believed that the p-type doping limitation of ZnSe is in part responsible for the high threshold and resultant overheating during laser operation because of the high contact resistivity of the p-type ZnSe layer in the laser structure.[4]

The short operating lifetime of laser diodes is also a major concern for commercialization of these devices.[3,4,6,7] Degradation in ZnSe-based devices is caused by the generation of extended defects, leading to non-radiative recombinations similar to problems existing in III-V lasers.[3,5] In early growths, defect densities as high as 10^8 cm^{-2} existed in the II-VI layers, partially due to the lattice mismatch between ZnSe and GaAs substrate.[3] Improvement in the growth of devices reduced the defect density to a level of 10^5 cm^{-2} by techniques such as using a lattice-matched system[7] and growing a GaAs buffer layer.[20] Even with a perfectly lattice-matched system, however, device lifetime is still a problem.[7] The problem is complicated by the fact that defects propagate during the device operation, and the degradation process is irreversible.[21] The

mechanism of how defects are generated and propagate in II-VI devices is not fully understood at the present time.

Hydrogen is very important in the growth and processing of semiconductor materials and devices.[22-25] The presence of hydrogen can be both beneficial and detrimental. The use of atomic hydrogen to clean substrates has proven to be very effective in removing surface contaminants,[26-32] while recently, the observation of hydrogen passivation of nitrogen in MOCVD[33] and gas source MBE (GSMBE)[34] growth of p-type ZnSe indicates that hydrogen presents a problem in those techniques for nitrogen-doped ZnSe growth. To date the best quality of ZnSe films and devices are grown by MBE.[3] Considerable effort has been devoted to the optimization of growth parameters for the improvement of p-type doping and to achieve a low defect density in ZnSe-based materials and devices.[3,4] However, potential effects of hydrogen on material properties in MBE growth of ZnSe have not been systematically investigated. Hydrogen is a major residual gas even in a well-baked MBE system. Even though this hydrogen is at levels of 10^{-9} to 10^{-10} Torr during growth, it has been known to cause significant compensation problems in other materials systems. For example, severe hydrogen compensation of Mg in GaN has been observed[159] under standard MBE growth conditions.

Thus, this study consists of three main thrusts - understanding and controlling the major defects that occur during growth; understanding the role of hydrogen in the growth and compensation of ZnSe; and a determination of compensation processes in ZnSe. The latter goal was extremely ambitious, but by combining the work in this dissertation with that performed in other laboratories both at WVU and elsewhere, a consistent picture begins to emerge. Experiments were planned to investigate effects of hydrogen in the processing of ZnSe thin films by MBE. The first part of this study investigated using atomic hydrogen to clean the GaAs substrate prior to ZnSe growth. ZnSe films grown on

substrates prepared with two cleaning procedures were compared. A significant reduction of micro-defects in ZnSe films grown on GaAs substrates cleaned with atomic hydrogen was obtained. Details of this work are described in Ch. III. The second part of this study investigated how hydrogen atoms are incorporated in MBE grown ZnSe and the role of hydrogen in the compensation process in nitrogen-doped ZnSe. Hydrogen is present during MBE growth in either atomic or molecular form. It is found that a high hydrogen incorporation occurs only when both atomic hydrogen and atomic nitrogen are present during the growth. Chapter IV presents these results through various characterizations of samples prepared with different growth conditions. For the third thrust, Fourier transform infrared spectroscopy (FTIR), photoluminescence (PL) and electron paramagnetic resonance (EPR) measurements give new information on compensation processes. Evidence of native defects such as the Se vacancy is observed using EPR measurements made in Prof. Halliburton's laboratory on ZnSe samples grown as part of this dissertation. PL measurements made in Prof. Giles' laboratory indicate that a deep level donor about 0.3 eV below the conduction band may contribute to the DAP band in heavily nitrogen-doped ZnSe. FTIR measurements indicate that while nitrogen may be on a lattice site, it is in at least two different states. These results are discussed together in Ch. V to shed light on compensation processes in ZnSe. Since the equipment was extensively used in this study, Ch. II is devoted to the background description of the MBE system and characterization tools. In the remainder of this chapter, the basic properties and applications of ZnSe will be discussed, and problems existing in the development of ZnSe-based materials and devices are reviewed. Finally, the statement of the problem for this study is addressed.

1.2 ZnSe: Basic Properties and Applications

Zinc selenide is a compound formed by combining the elements Zn (group II) and

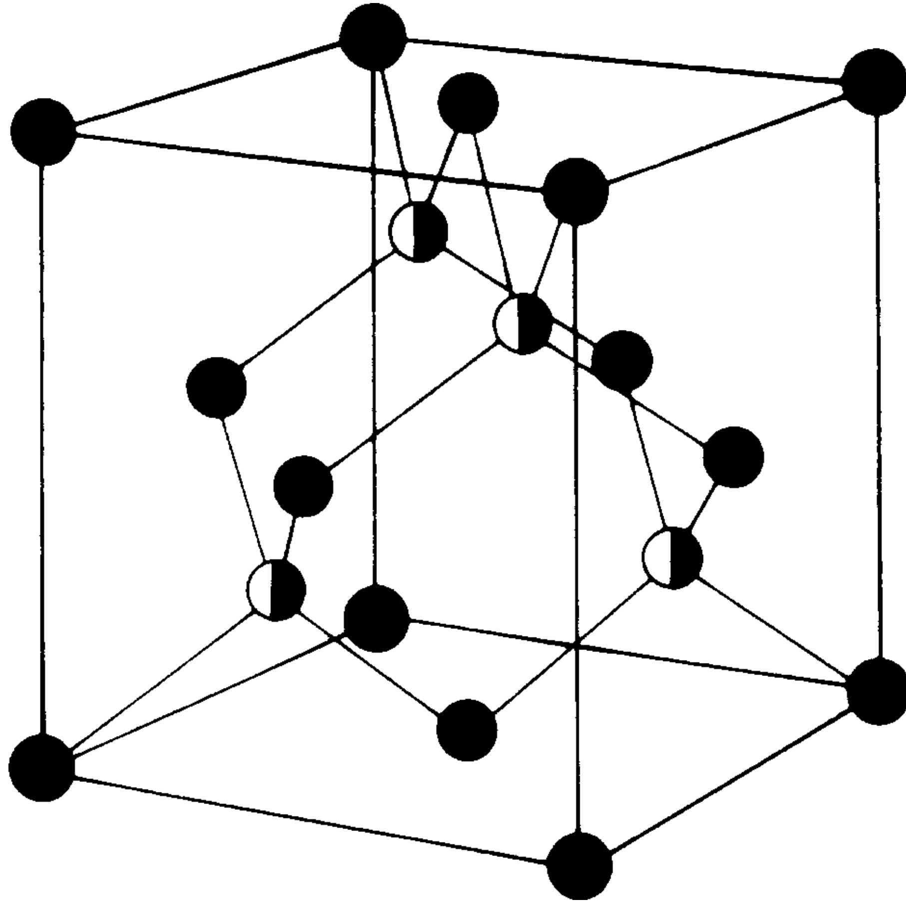

Fig. 1.1 Lattice structure of zincblende ZnSe.

Se (group VI).[1] Zinc and selenium are both on interpenetrating face-centered cubic (fcc) lattices with one occupying half of the tetrahedral holes in the other's lattice. Each zinc (selenium) atom is surrounded by four selenium (zinc) neighbors, so the structure has fourfold coordination. This structure is known as the zincblende structure and is shown in Fig. 1.1. A summary of fundamental properties of ZnSe is listed in Table 1.1. The energy band structure of ZnSe is schematically shown in Fig. 1.2 (without spin-orbit interaction).[2] The bandgap is 2.7 eV at room-temperature between Γ_1 and Γ_{15}.

ZnSe is attractive for applications in optoelectronics and photonics due to its wide bandgap of 2.7 eV.[3,4] Emission wavelengths in the range of 450 nm to 550 nm can be obtained from devices made by ZnSe and related compounds. While the major initial driving force behind the wide bandgap II-VI research effort was the display applications envisioned for short-wave LD and LED devices, the primary need at present is in the area of optical storage.[3,8] Rapid advances in optical recording have now reached the fundamental limit of the lasers that are currently used, namely that the storage density is limited by the size of the diffraction spot which is proportional to the square of the laser wavelength. A reduction of a factor of two in wavelength from the currently used infrared laser to a blue light laser is expected to provide a more than fourfold advantage in data storage-area density. The commercial market for blue diode lasers and LEDs is very bright. The sales of optical data storage devices for 1995 were $3.7 billion, and are expected to reach $5.1 billion by 1997.[8] An additional portion can be added by taking market share away from the huge magnetic data storage market which is projected to reach $35 billion by 1997.[8] The market for other applications such as optical data communication, flat-panel displays, laser printing, traffic lights and sensor applications are increasing with the maturation of these devices.[3,4,8]

In the early 90's, progress was made on the multilayer structures such as quantum wells and superlattices,[10] including the identification of potentially useful hetero-

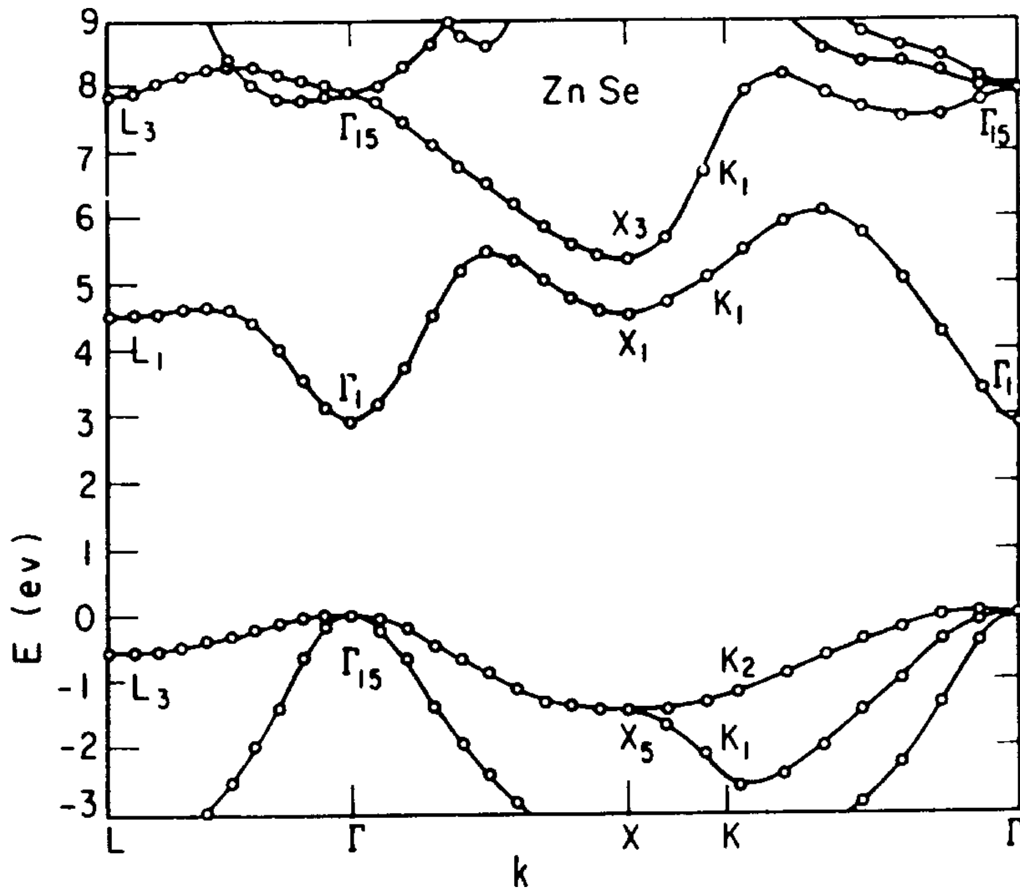

Fig. 1.2 Energy band structure of ZnSe (Taken from Ref. 2).

Table 1.1 Fundamental Properties of ZnSe

Lattice structure	zincblende, wurtzite (not typical)
Lattice constant	a = 5.6687 Å (zincblende)
	a = 4.01 Å, c = 6.54 Å (wurtzite)
Band gap (0 K)	2.8218 eV
Band gap (300 K)	2.70 eV
dEg/dT	-5×10^{-4} eV K^{-1}
dEg/dP	0.7×10^{-6} eV cm^2 kg^{-1}
Electron effective mass	0.13
Hole effective mass	heavy hole: 0.78 - 1.09
	light hole: 0.145
Electron mobility	200 cm^2 V^{-1} s
Hole mobility	20 cm^2 V^{-1} s
Refractive index	2.43 at 0.55 µm
Dielectric constant	$\varepsilon_r = 7.1$
	$\varepsilon_\infty = 5.4$
Thermal conductivity	0.19 W cm^{-1} K^{-1}
Thermal expansion coefficient	7.0×10^{-6} K^{-1}
Molecular weight	144.34 amu
Density	5.42 g cm^{-3}
Melting point	1520 °C

structures for light-emitting applications[21] along with the advances in the control of material purity and defects. When the doping advance was combined with the knowledge accumulated from research into the physics of II-VI heterostructures and the materials advances associated with MBE, the stage was finally set for the first serious consideration of prototype injection laser diodes. Pulsed lasing was first demonstrated at cryogenic temperatures by Haase *et al.* in 1991.[35] After that, efforts have been made in searching for diode lasers with practical working conditions, mainly a lower lasing threshold, a longer lifetime and high operating temperatures.[3,4,6,7] Progress toward a practical commercial device over the past several years has been substantial, and a laser operating at room-temperature for as long as 100 hours was announced by Sony in January of 1996.[36] Major breakthroughs in the development of ZnSe-based laser diode are listed in Table 1.2.

Table 1.2: II-VI Laser Diode Development Milestones

1990	Demonstration of ZnSe/ZnCdSe quantum well for blue-green lasers
1990	p-Type doping of ZnSe using atomic nitrogen source
1991	Demonstration of first ZnSe-based laser diode
1992	Blue-green ZnSe laser operating at liquid nitrogen temperature
1993	Blue-green laser operating at room-temperature
1994	Blue-green laser operating at room-temperature for 1 hour
1995	Blue-green laser operating at room-temperature for 4.3 hours
1996	Blue-green laser operating at room-temperature for 101.5 hours

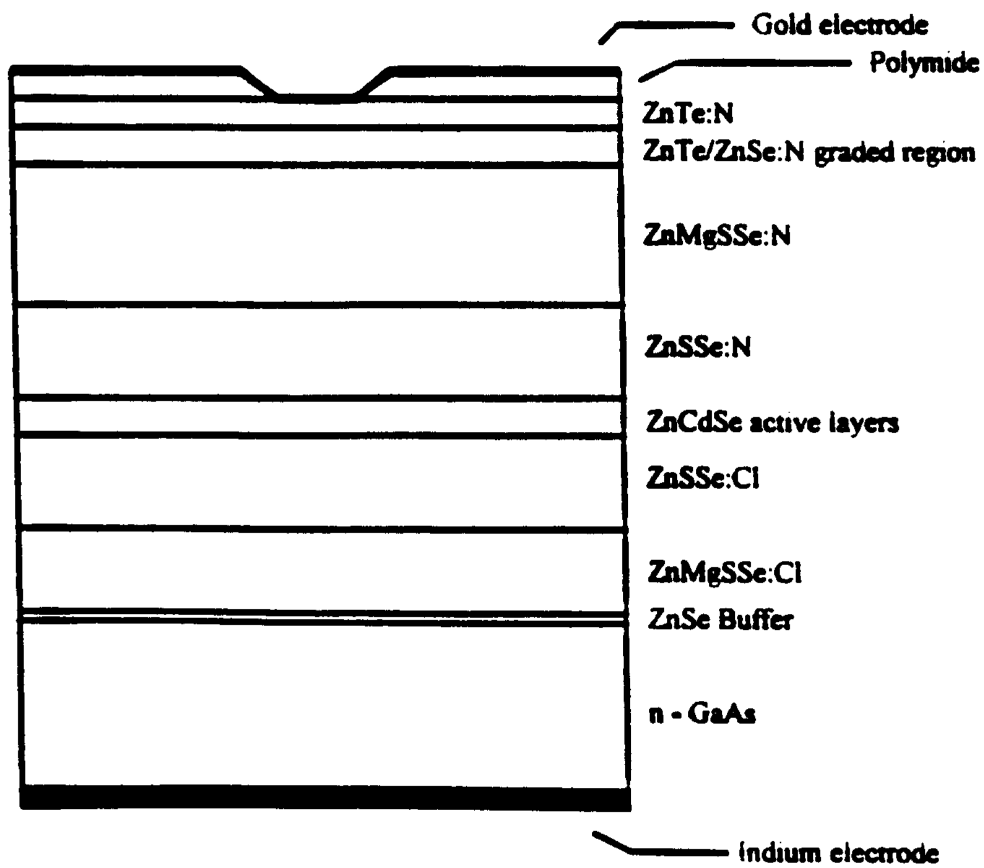

Fig. 1.3 Schematic diagram of a II-VI laser diode structure involving ZnMgSSe by Sony (Taken from Luo *et al.*[(21)]).

The structure of the ZnSe II-VI laser diode used by Sony is illustrated in Fig. 1.3,[4] in which GaAs is used as the substrate. Both GaAs and ZnSe buffer layers are grown prior to the ZnSSe layer growth in order to minimize the extended defect density. The ZnSSe layer provides a lattice-matched growth between the substrate and the ZnMgSSe cladding layer, which provides separate light confinement.[37] A single ZnSSe/ZnCdSe quantum well serves as the active layer and provides electron confinement of the laser cavity. A ZnTe/ZnSe multiple quantum well (MQW) structure is used for the p-type ohmic contact grading layer to the Pd/Pt/Au electrode.

1.3 Problems with ZnSe

In the development of ZnSe II-VI laser diodes, three basic problems are responsible for the difficulties in the realization of commercial devices.[4,21] The first is the limitation of p-type doping in ZnSe due to high compensation at high doping levels.[4,5,21] This limitation results in higher contact resistance and lower carrier injection in the laser structure, and results in higher threshold currents with resultant overheating during device operation.[4,21] The second is the high extended-defect density in II-VI epilayers,[3,4] which causes the generation and propagation of non-radiative recombination defects in the active region, and ultimately, device failure within a short time. The third is the non-ohmic contact on p-type ZnSe,[4,5] which will also result in overheating and higher threshold voltage. Improvements are possible in the design of laser structures to further increase the output power and efficiency by optimizing the quantum well active layer for better electron confinement and emitting light wavelength. Waveguiding and cladding layers can also be modified to get better light confinement and less light loss.[3,5,21] However, without major improvements in the basic problems mentioned above, device performance can not be improved even with new structures.[6,7]

This section will review studies on the development of ZnSe related to material growth and

qualities.

1.3.1 Substrate Issues

In epitaxial growth, lattice-matching between the epilayer and the substrate is crucial for obtaining high-quality films.[9] The lattice parameter versus bandgap for various semiconductors is shown in Fig. 1.4. ZnSe has a lattice constant of 5.6687 Å. A close match is GaAs and Ge, which have lattice constants of 5.6532 Å and 5.6575 Å, respectively. A practical method of growing high quality bulk ZnSe single crystal has not yet been realized.[5,21] The most common and commercially available substrate material used for the growth of ZnSe is GaAs.[5,21] GaAs is an attractive substrate material for heteroepitaxial growth of ZnSe primarily because of the relatively small lattice-constant mismatch with GaAs (~0.25%).[3,5] Secondly, the lattice-matched heterointerface between n-ZnSe and n^+-GaAs shows ohmic behavior in the current-voltage characteristic down to 77 K, implying that an n^+-GaAs substrate will serve as a good ohmic electrode to n-ZnSe in an n-ZnSe/n^+GaAs LED or LD structure.[9] Thirdly, high quality GaAs is commercially available and inexpensive as a consequence of the development of III-V semiconductor materials and devices over the last several decades.[5,21] Presently, most of the ZnSe-based light-emitting devices (LED and LD) are fabricated using GaAs as the substrate material.[3,5]

Ge and Si also have been studied for the heteroepitaxial substrate materials.[38-42] Ge is closely lattice-matched with ZnSe (0.17%). ZnSe has been grown on both Ge substrates and MBE-grown Ge epilayers (grown on Si substrate).[39] With the presence of a ZnSe/Ge superlattice incorporated in the buffer layer of the Ge epilayer, the quality of the subsequent ZnSe was greatly improved. Although Si is lattice-mismatched with ZnSe (4%), ZnSe has been grown on (100) and (111) Si substrates.[40-42] When ZnSe is

grown on Si, the Si atoms tend to react with Se atoms to form an amorphous layer of $SiSe_x$.[41]

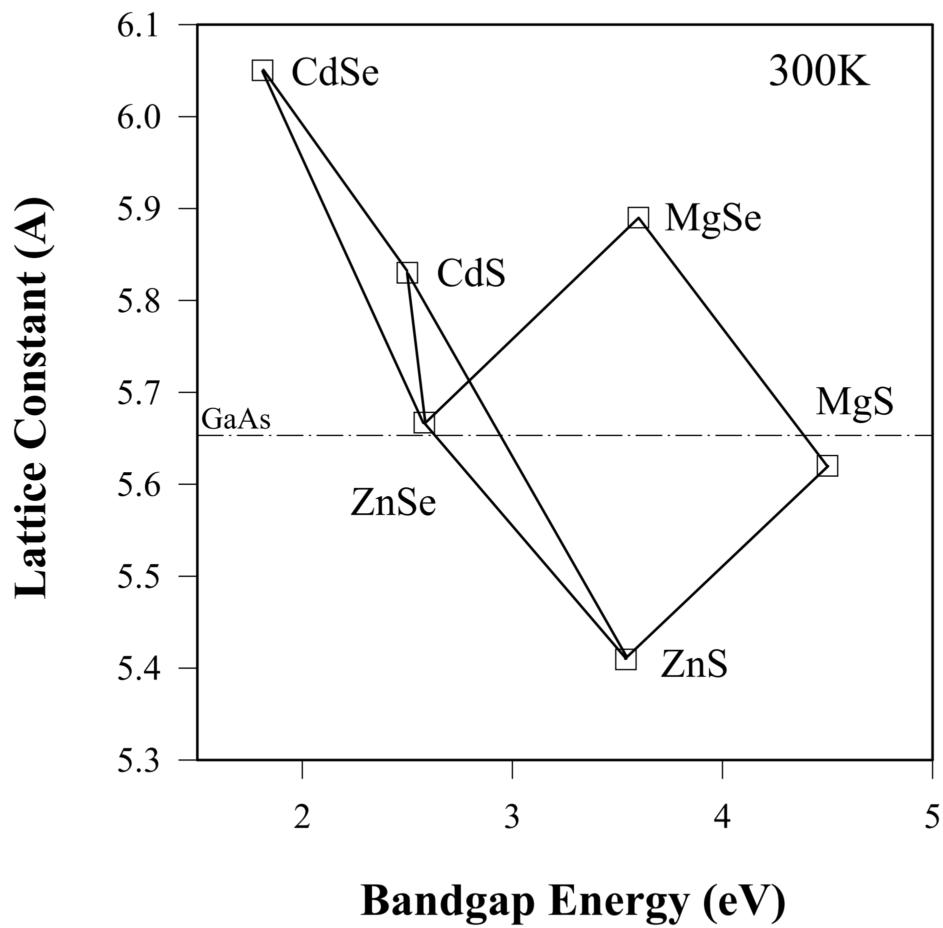

Fig. 1.4 Lattice constant *vs*. bandgap energy for a variety of II-VI semiconductors. Lattice constant of GaAs is indicated for the lattice matching with ZnSe.

By either depositing ZnSe on Si at room temperature and then performing solid-phase recrystallization, or depositing an As monolayer on Si prior to ZnSe growth, the interaction between Si and Se can be prevented and very uniform ZnSe films are obtained.[41] GaP[43] has also been used as substrate for the growth of ZnSe using MBE since the lattice mismatch is only about 4%. A disordered layer was found in the vicinity of the interface between the substrate and the epilayer. The crystalline quality for ZnSe grown on GaP was found to depend on the layer thickness. At a sufficiently thick (>1.5 μm) layer, the crystallinity is comparable to the layers grown on GaAs substrates.[43] While it has been demonstrated that a variety of substrates other than GaAs can be used for epitaxial growth of ZnSe, practical devices have only been reported for ZnSe on GaAs.

To date, most of the ZnSe LED and LD devices are fabricated on GaAs substrates. The small lattice-mismatch between ZnSe and GaAs, however, does result in interface states, dislocations, and other structural defects due to the lattice relaxation which can be the nucleation sites for other defects during and after growth.[3,5] The ideal candidate for ZnSe epitaxial growth to completely eliminate the lattice mismatch would be single crystal ZnSe substrate. Unfortunately, high-quality ZnSe substrates with useful large area are not commercially available, and small supplies in laboratory scale are very expensive.[5,21] Nevertheless, vital progress had been made in improving bulk ZnSe quality.[7] Recently, several groups have reported the realization of ZnSe-based LEDs grown on ZnSe substrates.[44-47] Laser diodes grown on ZnSe, with pulse lasing near room-temperature and continuous-wave lasing at 77K, have also been reported.[47] Yet homoepitaxial growth on ZnSe substrates does not reduce the defect density in the interface, which is about 10^4 cm^{-2} in the best growth conditions for both GaAs and ZnSe substrates.[6,7] Apparently the key to success will depend on understanding growth and nucleation as well as lattice-matching.

1.3.2 ZnSe Growth

Intensive studies of wide bandgap II-VI bulk materials started in the 1960s,[2] but electrooptic devices were never made. It was not possible to achieve conducting ZnSe from the bulk growth, since the very high temperatures[2] (about 800-1200 ºC) used for the bulk growth resulted in the compensation of impurities via native defects, and the resulting materials exhibited very high resistivities. The application of non-equilibrium growth techniques such as MBE for the growth of epilayers, and ultimately heterostructures of ZnSe-based materials alleviated the problem of controlling impurity incorporation and defect generation due to the significantly lower growth temperature than that used for bulk growth.[9] MBE is by far the simplest growth technique for performing a non-equilibrium epitaxial growth.[5] The use of MBE for the growth of ZnSe-based materials has proved to be very successful using both elemental and compound sources of the constituent species.[5,9] Other growth methods such as MOCVD,[4] metalorganic vapor phase epitaxy (MOVPE),[12] and gaseous source ultrahigh vacuum epitaxy technologies, such as metalorganic MBE (MOMBE)[48,49] or GSMBE[11,50,51] have also been attempted.

The objective of growth is to obtain high quality materials with good crystallinity, low defect density, high purity, smooth interfaces and controllable conductivity.[9] While traditional crystal growth techniques driven by thermodynamics were not able to achieve all of these requirements, non-equilibrium growth MBE driven by kinetics is applicable.[5,9] During MBE growth, species are evaporated from Knudsen-cells and directed to the substrate.[9] The compound formation is determined by the relative sticking coefficient of the constituent elements to the substrate surface, the vapor pressure difference between the constituent elements and the growing compound, the substrate temperature and the substrate surface conditions.[9] In the case of ZnSe grown

on a GaAs substrate, the vapor pressure of both Zn and Se are very high, while that of ZnSe is very

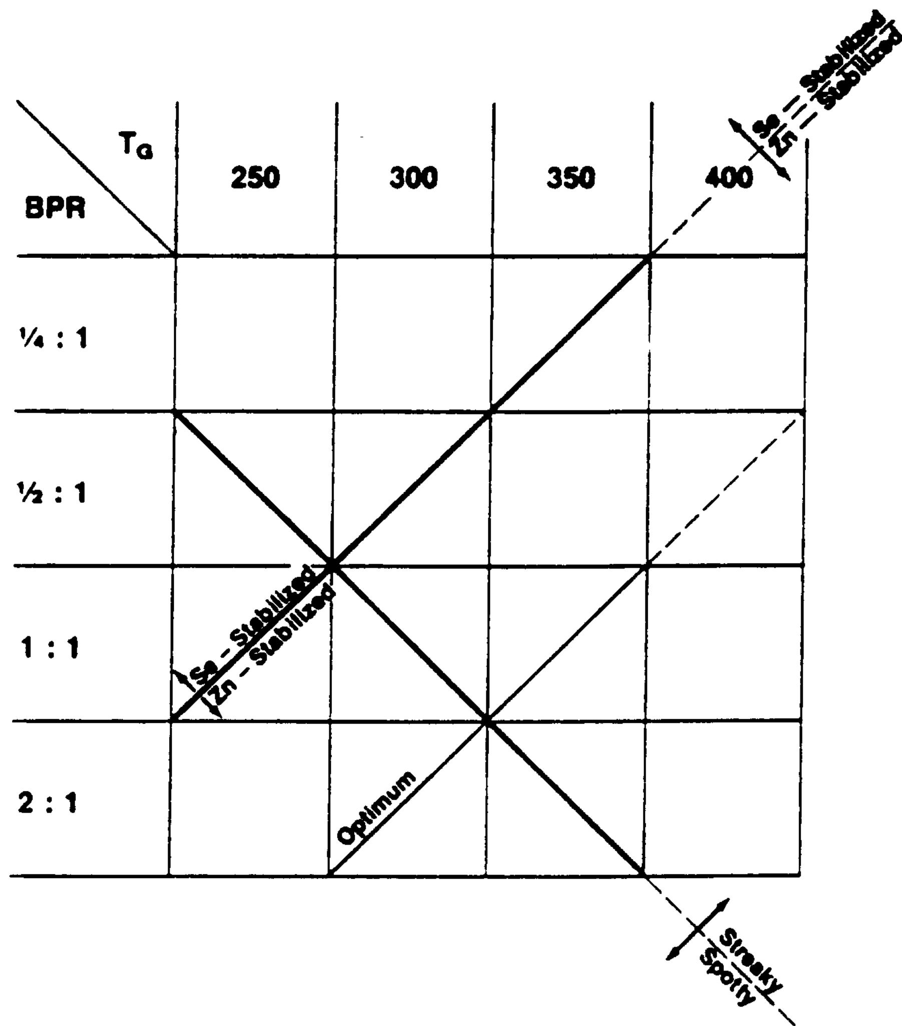

Fig. 1.5 Growth matrix of T_G and beam-equivalent pressure ratio BPR of Zn to Se, which provides growth reference for Zn-stabilized or Se-stabilized growth, and spotty or streaky pattern from the growth surface (Taken from DePuydt *et al.*[74]).

low. Hence, the re-evaporation of ZnSe is not a problem at a typical growth temperature (~ 300 °C) in MBE. However, since the sticking coefficient for each species is generally not the same, it is necessary to stabilize the flux from each of the effusion cell to its equilibrium condition for the uniform growth.[9] In practice, systematic investigation has been made in optimizing the growth conditions to achieve the expected high quality films.[52-54] The most important growth parameters are growth temperature, Zn-to-Se beam flux ratio and substrate surface state prior to ZnSe growth. Subsequent film quality can be examined by low-temperature photoluminescence (PL), Hall measurements and other characterization techniques.

DePuydt and coworkers[52] have systematically studied the effects of growth temperature (T_G) and Zn/Se beam-equivalent pressure ratio (BPR) on the growth of undoped ZnSe on (100) GaAs substrate using reflection high energy electron diffraction (RHEED) to monitor the surface reconstruction during growth. They generated a growth matrix as shown in Fig. 1.5, in which the Se-stabilized condition and the Zn-stabilized condition were determined by the combination of T_G and BPR. The Zn-stabilized condition corresponds to a C(2x2) surface reconstruction and Se-stabilized condition corresponds to a (2x1) reconstruction in RHEED. The transition between the two stabilized surface regimes is indicated in Fig. 1.5. Meanwhile, another line was defined as the transition from a spotty to a streaky RHEED pattern. It is generally believed that the spotty pattern indicates a three-dimensional growth while the streaky pattern indicates a two-dimensional growth. The conditions labeled as the optimum line in Fig. 1.5 were suggested because the best quality undoped ZnSe samples were grown by the conditions indicated by this line, which indicated a Zn-stabilized condition with the T_G and BPR configuration parallel to the Se-to-Zn transition line. Note that while the best quality occurs for Zn-rich conditions, later discussions will indicate that optimal N-doping conditions are actually Se-rich.

The substrate surface is always important for epitaxial growth.[9] For the MBE growth of ZnSe on GaAs substrate, the normal procedure of substrate preparation is a solvent degrease followed by an acid etch and thermal anneal in UHV at ~ 600 °C to remove the native oxide.[5,9,52] The ideal surface reconstruction suitable to ZnSe growth has been investigated broadly with various approaches, such as substrate treatment with different chemicals[48] and preheat procedures,[29,55] GaAs and/or ZnSe buffer layer[56,57] growth prior to ZnSe epilayer growth, misoriented substrates,[58] and the use of high index substrates.[59 Models have been proposed for the surface stoichiometry effects on ZnSe grown on GaAs.[60-62] Tamargo *et al.*[60] used a simple model based on counting the valence electrons at the interface. They predicted that surfaces with an equal number of the constituent atoms available for formation of interface bonds will produce ideal, abrupt interfaces with overall electronic balance, and a reduction of interface states. Samples grown with a GaAs (3x1) reconstruction, which is nearly stoichiometric (slightly As-rich), exhibit the highest quality. The Ga-rich (4x3) surface was also reported to result in a low density of interface states for ZnSe growth.[63] It was speculated that the ZnSe/GaAs interfaces exhibiting the lower interface state densities were associated with the presence of an interfacial layer of Ga_2Se_3.[61,63,64] Transmission electron microscopy (TEM) cross-sectional dark-field and high-resolution images of heterojunctions formed on (4x3) reconstructed GaAs surfaces indicated the presence of a uniform band, which was interpreted as an interfacial compound having an average thickness of two monolayers. Image simulations strongly supported the identification of zincblende Ga_2Se_3 as the interfacial layer formed on As-deficient GaAs epilayers.[63]

Photo-assisted MBE growth of ZnSe on GaAs substrate has been studied by various research groups due to its success in the growth of CdTe and HgCdTe.[65-69] An ultraviolet (UV) light source is used for the irradiation on sample surface during ZnSe growth. Effects of the photon irradiation on the growth of ZnSe on GaAs include: (a)

reduced growth temperature from the non-irradiated growth,[67] and (b) enhanced adatom migration.[68] The growth rate reduction is due to the increased desorption rate of Se adatoms with the photon enhancement, resulting in the decrease of the minority surface species (Se).[69] There is a controversial result regarding the surface morphology of ZnSe epilayer by photo-assisted MBE. Ichikawa *et al.*[68] reported a reduction of hillock density of epilayers from 10^6 to 10^4 cm^{-2}, while Ohishi *et al.*[66] observed an inferior surface morphology indicating enhanced three-dimensional growth by the photo-irradiation.

While solid sources are generally used in the MBE growth of ZnSe on GaAs, gaseous sources can be used to replace the high vapor pressure elemental solid sources for better composition control and reproducibility from the high controllability of the gas supply.[48-51] In the GSMBE growth, elemental Zn and the gas H_2Se (which is thermally cracked) are used as sources for the growth of ZnSe.[50,51] It is found that the two-dimensional growth regime of ZnSe films can extend down to 150 °C, while the growth rate decreases with increasing growth temperature, and increases with the H_2Se flow rate increasing up to 4 sccm.[51] The surface morphology of ZnSe films is smooth when the H_2Se cracking temperature is below 1000 °C.[50,51] These results are similar to the solid source MBE growth of ZnSe when a cracked Se source is used.[70,71] It is estimated that the activation energy of Se desorption is about 0.15 eV for the thermally cracked H_2Se source, while for Se source without cracking, in which polyatomic Se species participate in the growth, it is 0.65 eV.[51] The low activation energy is attributed to Se atoms which are the dominant Se species for the cracked H_2Se or Se sources. Se monomers desorb at lower substrate temperatures than polyatomic Se species from an uncracked Se source. The unintentionally doped ZnSe grown by GSMBE shows an n-type conductivity with residual impurities of In and Cl in these ZnSe layers, originating from the H_2Se source.[51]

1.3.3 Doping and Compensation in ZnSe

Electrooptic devices require controllable concentrations of activated p- and n-type dopants. For the wide bandgap II-VI family, materials can be easily doped one type but not both.[3,5,21] Specifically, ZnSe is easily doped n-type, while p-type conductivity is very difficult to achieve due to high compensation in the material.[5,9]

ZnSe can be made n-type by using Ga,[9] In,[9] I_2,[72] or Cl (from $ZnCl_2$) as the doping source.[34,73-76] The highest level of donor incorporation has been achieved using Cl with carrier concentrations near 10^{20} cm^{-3} through techniques such as MBE,[73-75] planar doping with MBE,[76] and GSMBE.[34] The donor level is relatively shallow (~28 meV)[5] and the crystal quality remains very high for significant donor incorporation. Hydrogen does not appear to passivate Cl atoms and affect the electrical conductivity.[34] Most optical devices reported thus far utilize Cl for the n-type dopant species in ZnSe-based binaries, ternaries and quaternaries.[5]

In the quest of p-type ZnSe, an effective dopant was not found until the use of atomic nitrogen.[11,12] For the II-VI Zn-chalcogenides such as ZnSe, elements in column I (such as Li) and column V of the periodic table are potential candidates for acceptors.[5] Li was incorporated into ZnSe using MBE with resulting carrier concentrations up to a level of 10^{17} cm^{-3}.[77] However, the relatively small size of the atom allows substantial interstitial incorporation and significant lattice diffusion, particularly at room-temperature and during device operation. Thus Li is precluded as a technologically viable p-type acceptor.[5] Both arsenic[78] and phosphorus[79] were investigated for the p-type doping of ZnSe. In the case of As, very high levels (~10^{17} to 10^{21} cm^{-3}) of impurity incorporation are achieved using either Zn_3As_2 or an As cracker for a source of As.[78] Arsenic is easily incorporated into ZnSe as indicated by secondary ion mass spectrometry (SIMS) and photoluminescence spectra which show that the shallow acceptor levels are

present. In all cases, however, the ZnSe:As layers were found to be highly resistive. Similar results were reported for the use of phosphorus as a p-type dopant.[79] Theoretical work by Chadi[17] using first-principle pseudopotential calculations suggested that the presence of either As or P within the ZnSe lattice actually forms two distinct atomic states, a shallow effective-mass state with a small lattice relaxation and deep state with large lattice distortion resulting from the breaking of a Zn-impurity bond. Consequently, the high resistivity of ZnSe:As or ZnSe:P layers could be due to the presence of the shallow-deep acceptor states appearing during the use of As or P as acceptor species, instead of native defect self-compensation processes. The calculation also indicates that whether in the fourfold coordinated state with small lattice relaxation or in the large lattice-relaxed state, nitrogen would behave as a shallow acceptor. Thus Chadi postulated that nitrogen could be the optimum acceptor for ZnSe.

Using nitrogen as the p-type acceptor species was initiated by Park and coworkers.[11] Nitrogen incorporation levels in the 10^{15} - 10^{16} cm^{-3} range were obtained through the use of N_2 gas at relatively high flow levels during the MBE growth of ZnSe.[80,81] However, further incorporation of nitrogen is limited by the very low "cracking efficiency" of molecular nitrogen. The major technological breakthrough was the implementation of a radio frequency (rf) plasma cell in conjunction with ultrapure nitrogen gas during the MBE growth of ZnSe.[11] A plasma source built by Oxford Applied Research operates at 13.5 MHz under conditions of molecular flow using nitrogen gas, and provides a source of atomic nitrogen to the ZnSe growth front. By characterization of the nitrogen flow ejected from the plasma source it was found that an appreciable flux of neutral nitrogen atoms are generated.[82] The incorporation of nitrogen in ZnSe using an rf plasma source was first confirmed by the presence of donor-to-acceptor pair (DAP) transitions dominating the PL spectra of the ZnSe:N layers. The p-type conductivity was determined by capacitance-voltage (C-V) measurements, with

the net acceptor concentrations around the $3x10^{17}$ range.[11] Following the success of the rf plasma source for nitrogen-doped ZnSe, both electron cyclotron resonance (ECR) plasma[83] and microwave[84] sources were also found to give rise to p-type ZnSe:N. The realization of p-type conductivity of ZnSe:N led the II-VI wide bandgap semiconductor applications to a new stage: blue-green ZnSe-based LEDs and LDs were then demonstrated and improved.[35]

Although nitrogen-doped ZnSe can be used to demonstrate the fabrication of devices, highly p-type ZnSe:N is still hard to achieve.[3,4] As the amount of incorporated nitrogen atoms is increased, either by reducing the substrate temperature or increasing the nitrogen flux or plasma power, self-compensation was also seen to increase.[85] At low doping concentrations, the net acceptor concentration (N_A-N_D) increases linearly with increasing nitrogen doping concentration. At a certain nitrogen concentration depending on growth conditions, the net acceptor concentration saturates with a maximum value of about $1x10^{18}$ cm^{-3}. After that the (N_A-N_D) actually decreases while the nitrogen concentration increases.[86,87] It was generally believed that the limitation is caused by self-compensation in p-type doping of ZnSe.[86] PL measurements indicated that low concentration (N_A-N_D less than 10^{17}) samples have a shallow DAP emission peak at 2.696 eV while the high concentration (N_A-N_D greater than 10^{17}) layers have a dominant deep DAP emission peak at 2.678 eV. At the saturating level (N_A-N_D around 10^{17}), both shallow and deep DAP emission peaks occur.[87] The typical PL spectra for different doping levels of ZnSe:N layers are illustrated in Fig. 1.6. Various techniques[86-88] such as secondary ion mass spectrometry, ion beam analysis and resonant nuclear reaction have confirmed that high nitrogen concentrations can be achieved during growth. Nitrogen concentrations as high as $1.5x10^{20}$ cm^{-3} have been obtained in oversaturated samples. By using ion channeling to identify the nature of the compensation centers, no interstitial atoms (N, Zn, Se) were present even in the heavily doped samples.[88] Thus, all nitrogen

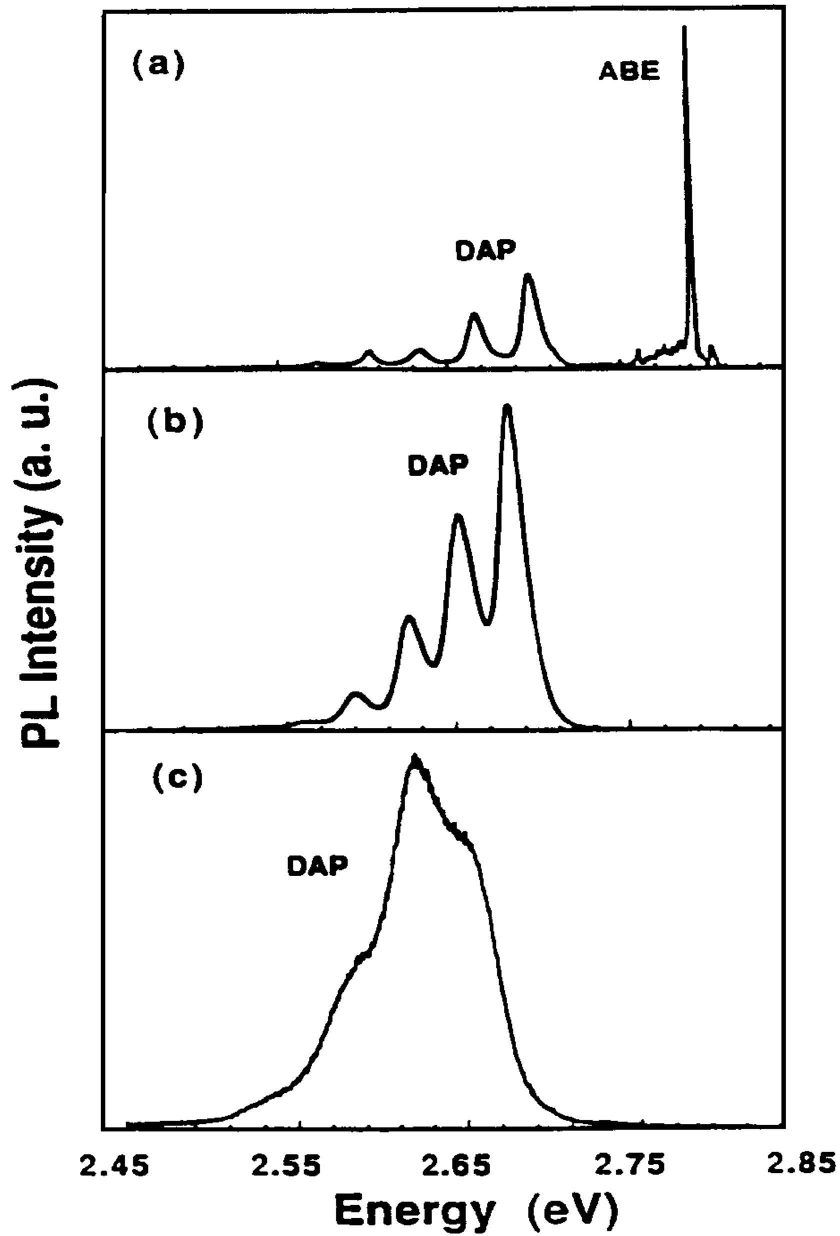

Fig. 1.6 Typical PL spectra of ZnSe:N with various doping level at 10 K
(a) [N] < $6x10^{17}$ cm^{-3}, (b) [N] = $1.5x10^{18}$ cm^{-3}, and (c) [N] = $1.3x10^{19}$ cm^{-3}
(Taken from Qiu *et al.*[85]).

atoms appear to be incorporated on ZnSe lattice sites.

Several competing theoretical models have been proposed to explain the compensation mechanisms in nitrogen-doped ZnSe. One of these models is the native-defect-induced compensation center, which was first proposed by Hauksson *et al.*[13] The proposed center consists of a double-charged Se vacancy, which acts as a deep donor about 300 meV below the conduction band,[89] in conjunction with a nitrogen acceptor at the next-nearest-neighbor site. The resulting complex, as showed in Fig. 1.7, acts as a singly-charged donor. They suggested that this V_{Se}-Zn-N_{Se} complex is the deep donor observed from the DAP photoluminescence spectrum of nitrogen-doped ZnSe.[13] The recombination processes with the involvement of both shallow and deep donors are illustrated in Fig. 1.8. The nitrogen acceptor in ZnSe is about 110 meV above the valence band. At low temperatures, the shallow donor-acceptor pair recombination gives a DAP peak at 2.696 eV. The binding energy of the shallow donor is estimated to be 26 meV. Another DAP peak occurs at 2.678 eV, an energy shift of 18 meV, which could correspond to a deep donor with a binding energy of 44 meV if the same acceptor level as the shallow DAP is assumed. They also observed an increase in the deep DAP band as the Zn/Se flux ratio is increased, and a (N_A-N_D) increase as the substrate temperature decreased. Both trends are consistent with a possible variation in Se vacancies in the doped layers as the growth conditions changed. Similar results have been reported by other groups.[87,90,91] Zhu *et al.*[87] measured temperature dependent PL spectra from nitrogen-doped ZnSe epilayers with different net acceptor concentrations, suggesting the ionization energies of 110 meV for a nitrogen acceptor, 30 meV for a shallow donor and 55±5 meV for a deep N-associated donor.

Optically detected magnetic resonance (ODMR) signals have been measured in nitrogen-doped ZnSe.[92] The shallow donor has a resonance at g=1.11. The deep donor, however, shows a resonance at g=1.38, and is anisotropic. In higher nitrogen

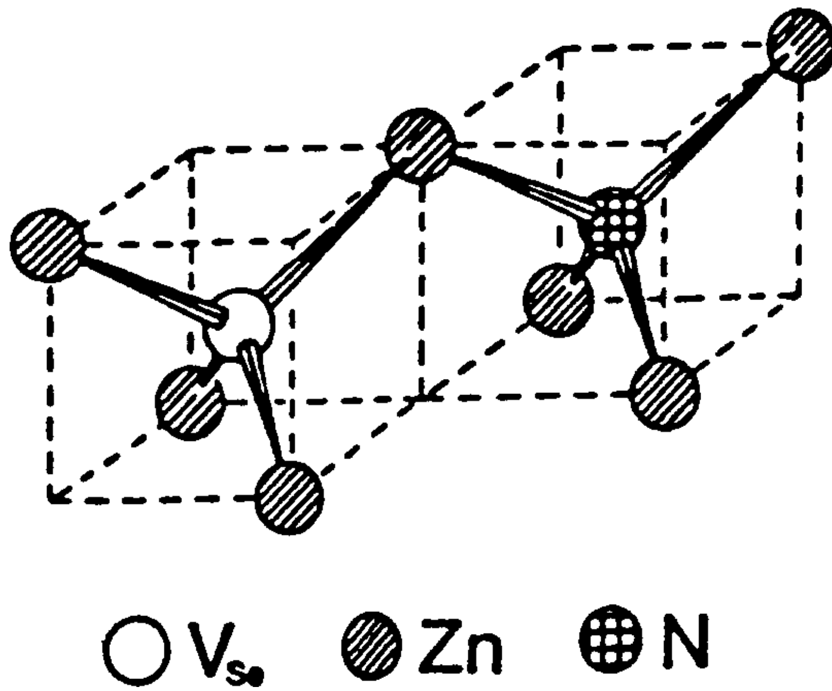

Fig. 1.7 Se vacancy complex in ZnSe:N involving the association of the V_{Se} double donor and a nitrogen acceptor (Taken from Hauksson *et al*.[(13)]).

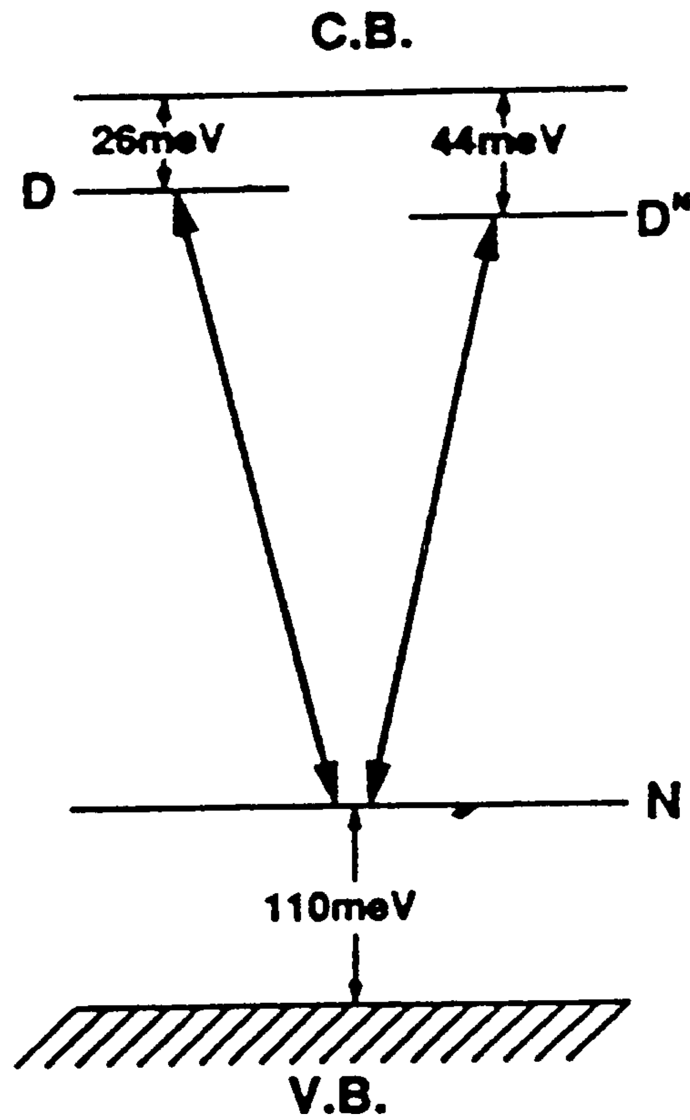

Fig. 1.8 Model for DAP recombination process in nitrogen-doped ZnSe involving both a shallow donor (26 meV) and a deep donor (44 meV). The nitrogen acceptor is labeled N (Taken from Hauksson *et al.*[(13)]).

concentration samples with dominant deep DAP emission peak, the shallow donor signal is absent similar to the suppression of the shallow DAP transitions. The g=1.38 resonance has been associated with the compensating donor (V_{Se}-Zn-N_{Se}). Another signal at g=2.00 was isotropic at 9 GHz and was originally assigned to a deep nitrogen acceptor.[92] This center was later re-examined by Kennedy *et al*.[93] It is found that this g=2.00 peak is anisotropic at 24 GHz with trigonal symmetry, and could be due to another deep donor complex, possibly V_{Se}-Cu or V_{Se}-Ag, present in the samples at levels of $\leq 1x10^{15}$ cm^{-3}. The presence of three donors in nitrogen-doped ZnSe is also consistent with spin-flip Raman measurements.[94,95] The Raman spectra, obtained while in resonance with the donor-bound excitons (D^0X), indicate three donors with the same g-values as those observed by ODMR.

Theoretical calculations using the first-principle total-energy method on ZnSe by Laks *et al.*[14] had concluded that native defects alone cannot be responsible for the difficulties in p-type doping of ZnSe. This work indicated native defect concentrations in MBE-grown stoichiometric ZnSe are too low to compensate at levels seen. While deviation from stoichiometry in ZnSe can produce large amounts of native defects these, however, should compensate both n-type and p-type materials. In contrast, Garcia and Northrup[15] indicate that the Se vacancy may indeed be important in ZnSe. They calculated the formation energy of the dopant-Se-vacancy complex and found that the lattice relaxation associated with Se vacancy will lower the formation energy of acceptor-V_{Se} complex significantly. However, their calculation indicated that the dopant-Zn-interstitial complex had even lower formation energy than the dopant-Se-vacancy complex, which should make it more abundant. For either complex, the maximum hole concentration is estimated to be in the 10^{18} cm^{-3} range by carrying out the growth of ZnSe under more Se-rich conditions although the solubility of the acceptor dopant is more favorable under Zn-rich conditions.

Various types of lattice-relaxation induced defects have been proposed as another way to account for p-type doping compensation in ZnSe.[16-19] An acceptor has two atomic configurations: a metastable effective-mass state with a small lattice relaxation labeled a^0, and a deep A^0 state with a large lattice distortion which is responsible for most of the acceptors in ZnSe.[16,17] Among the column V dopant candidates, nitrogen is found to give rise to a shallow acceptor state in either the small or large-lattice relaxed limits, and hence is a more suitable acceptor dopant for ZnSe.[17] Another model of lattice relaxation is illustrated in Fig. 1.9. In a zincblende structure, the distortions along the [111] bond axis lead to the rupture of host bonds (Zn-Se bond in the case of ZnSe). The bond breaking energy is found about 0.3-0.4 eV for the +2 charge state of the broken-bond. This state did not give a clear minimum in the total energy and the atoms slowly relaxed back to their ideally bonded positions. However, the bond breaking energy is significantly reduced when free holes are present. Two Zn-Se bonds are broken and a Se-Se dimer bond is formed as shown in Fig. 1.9 (b). The symmetry of the double-broken-bond (DBB) complex is σ_{1h}, and the N impurity maintains a fourfold coordinated symmetry. If the N atom of the complex is replaced by a Se atom, the lattice distortion would place one electron in each of the two Zn dangling bonds thereby making the DBB state a double donor. With the N present, however, the complex is only a single donor, which can passivate a second N atom not associated with the complex, and the total energy is lowered by nearly 0.2 eV compared to the configuration of isolated DBB with distant neighbor N. Therefore, the formation of a DBB defect complex with a N acceptor is favorable in ZnSe:N. It is also found that the Zn-N bond length for the DBB defect is 0.07 Å shorter than for substitutional N, which is larger than the actual lattice constant measured in nitrogen-doped ZnSe,[96] thus providing a possible explanation for the larger than expected lattice constant reduction with doping.

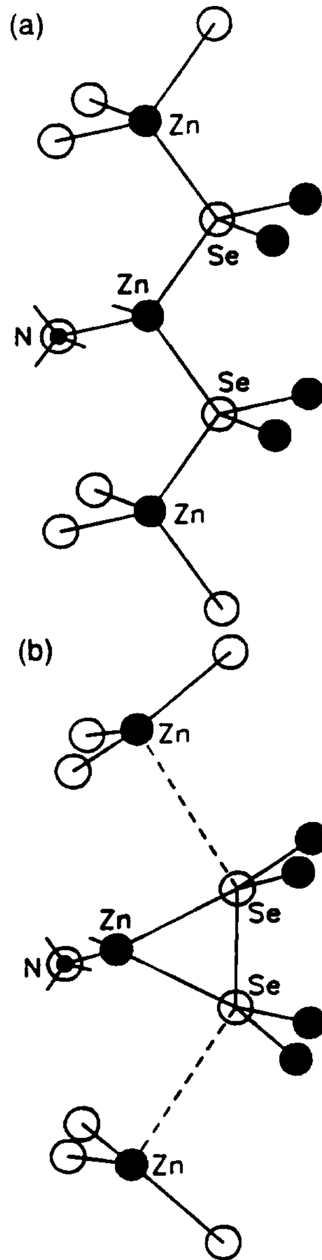

Fig. 1.9 Lattice relaxation induced compensating donor in ZnSe:N (a) ideal zincblende lattice for ZnSe, (b) double-broken-bond (DBB) state resulting from the breaking of two Zn-Se bonds and the formation of a Se-Se bond (Taken from Park and Chadi[18]).

In contrast to many of the above-mentioned predictions, it is found experimentally that the incorporated N atoms are located primarily at the substitutional sites, and that both Zn and Se atoms are located at the substitutional sites.(88,97,98) Therefore, compensation in heavily nitrogen-doped ZnSe is unlikely to be caused by such donors as N_{int} or N_{Se}-Zn_{int}, but more probably by complex defects which include the donor-type complexes such as V_{Se}-Zn-N_{Se}, N_{Zn}-N_{Se}, and/or DBB-N_{Se}. A cluster of N_{Se} such as $(N_{Se})_n$-Zn may also play a role as a deep donor.(97)

Acceptor dopant solubility in ZnSe has also been examined as the source of the p-type doping limit in ZnSe.(99-102) Laks *et al.*(101) calculated the solubilities of Li and Na in both ZnSe and ZnTe. They found that Li solubility in ZnTe is 10-1000 times larger than in ZnSe, while the solubility of Na is very low in both materials. Above the solubility limits, second phase formation can occur. These results are in agreement with experimental observations of Li as acceptor dopant in ZnSe.(77,103) The solubilities for Na, Li, and N in ZnSe are calculated to be 4×10^{15}, 6×10^{18}, and 2×10^{19} cm^{-3} at a growth temperature of 250 °C, respectively.(101) For similar growth conditions, the acceptor concentration in ZnTe is about one order higher than in ZnSe.(99,100) These results again indicate that nitrogen is the better choice for an acceptor in ZnSe. However, it is not clear what the second phase may be for nitrogen at the solubility limit. If this represents some type of “lattice solubility”, then the second phase may be represented by defect formation.

Hydrogen passivation of dopants in silicon and III-V based compound semiconductors is routinely observed.(33,34,104) It was speculated that the use of hydrogen-containing gas species and the presence of hydrogen during growth may also give rise to a similar acceptor passivation phenomenon for the II-VI materials. In epitaxial growth techniques utilizing gaseous sources, hydrogen typically plays a major role either as a carrier gas, as part of the dopant molecule (for example NH_3), or as a decomposition by-

product. Hydrogen may also be the source for dopant passivation in the wide bandgap II-VI semiconductors.[5] Fourier transform infrared studies of ZnSe:N grown by MOVPE[104] using NH_3 as the dopant source and H_2 gas as the carrier gas indicated the existence of N-H bonds in ZnSe:N films. In this case, the ZnSe:N layers were highly resistive, in agreement with that from MOCVD[33] studies. GSMBE[34] growth of ZnSe was performed to investigate the hydrogen incorporation and the electrical passivation of both n and p-type dopants for ZnSe. It is found that the hydrogen incorporation closely tracks the nitrogen incorporation which was intentionally varied. In Fig. 1.10, the SIMS profile is shown for a ZnSe:N layer grown by GSMBE. Films grown with a nitrogen plasma source, in conjunction with GSMBE, are typically found to be highly resistive, indicating the potential passivation of acceptors by hydrogen. In contrast, however, ZnSe grown by GSMBE and doped with Cl did not indicate any deleterious effects from the presence of hydrogen at the growth front and does not appear to be electrically passivated.[34] The difficulties encountered for achieving p-type conductivity in ZnSe during growth using MOCVD, MOVPE and GSMBE suggest that hydrogen is effectively incorporated into the lattice when ZnSe is doped with nitrogen. Alternate doping sources are required to eliminate the hydrogen species prior to incorporation.

1.3.4 Defect Density

Among the practical issues in ZnSe-based LED and LD development, the high defect density in epilayers of ZnSe and its alloys is the most severe problem not effectively solved to date.[5-7,21] There are two types of defects in ZnSe-based device structures. First, point defects in the strained (Zn,Cd)Se active quantum well region provide undesired nonradiative recombination and release highly local electronic energy into the lattice. Second, a specific form of a stacking fault-like defect, bounded by

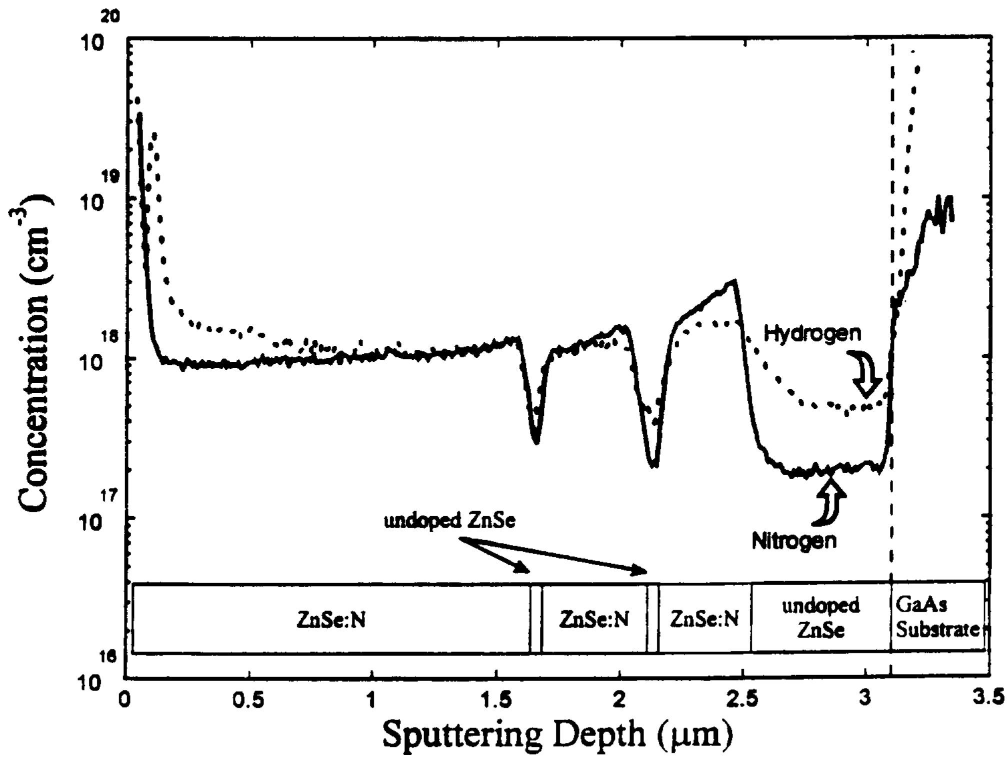

Fig. 1.10 SIMS profile of a ZnSe:N structure grown by GSMBE, indicating the nitrogen doping related hydrogen incorporation (Taken from Ho *et al.*[34]).

threading dislocations, can be generated at the II-VI /III-V interface during growth. The presence of extended defects such as these stacking faults and associated threading dislocations combine with point defects to produce growth of dislocation networks within the active region. These dislocation networks act to reduce the optical gain by nonradiative recombinations and ultimately end the lasing process.[5] Therefore, a primary concern is the reduction of the density of point defects as well as the number of extended defects within the device. The origins of these defects have been investigated using electroluminescence (EL) and transmission electron microscopy in an attempt to determine if they are intrinsic to the material or due to the growth method.

Dark line defects are observed in degraded ZnSe-based devices.[105-109] The dark line defects are located in the quantum well (QW) active region and are observed in EL,[105,106] PL[108] and cathodoluminescence (CL)[110,111] microscopy images. TEM[105-109] examination found that these dark line defects are dislocation patches which are nucleated at threading dislocations. The threading dislocations originated at stacking faults nucleated at or near the II-VI/GaAs interface. A schematic diagram of this defect complex is illustrated in Fig. 1.11. These stacking faults are observed as the most common defects in II-VI light emitting device structures, including nondegraded areas,[107] and are believed to be formed during the MBE growth. Tanimura *et al.*[112] investigated the paired stacking faults structure in a ZnSe epilayer grown on a GaAs (100) buffer layer with a fault density of about 10^8 cm^{-2}. They observed that the stacking faults are extrinsic and form on (111) and ($\bar{1}\bar{1}1$) planes with the same polarities as determined by convergent-beam electron diffraction. The two stacking faults meet at a point which is at or within a few atomic layers of the interface between ZnSe and GaAs. Three possible formation processes were proposed for the paired stacking faults in ZnSe epilayer on GaAs. The first is propagation of defects from the GaAs buffer layer. Since

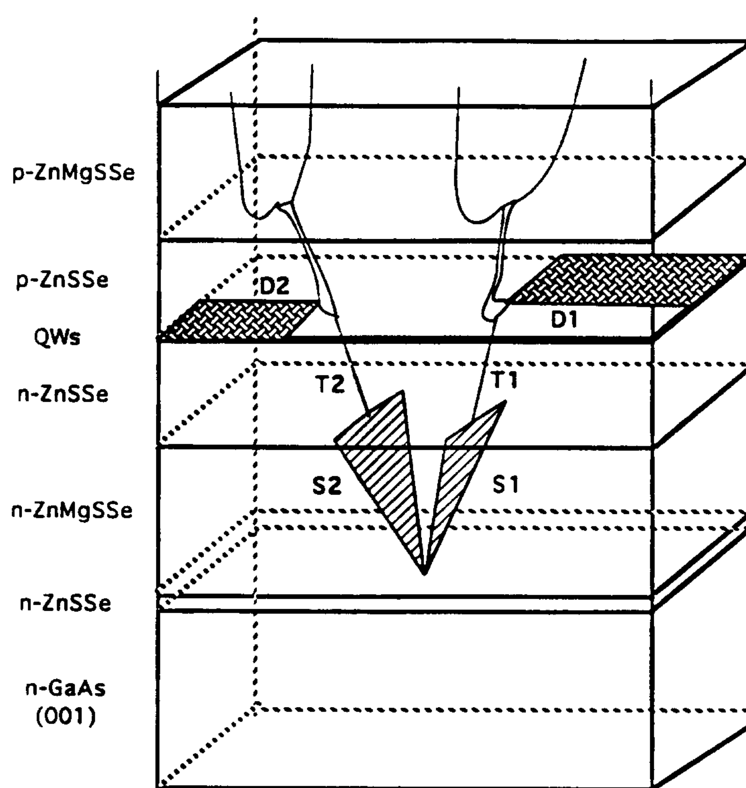

Fig. 1.11 Schematic of three dimensional arrangement of defects in a ZnSe laser structure. S1 and S2 are stacking faults originated at II-VI/GaAs interface, T1 and T2 are threading dislocations bound to stacking faults, and D1 and D2 are dislocation network patches nucleated at threading dislocations and developed into the active layer (Taken from Hua *et al.*[(62)]).

no defects are observed in the GaAs buffer layer, this source was ruled out in this case. Second, defects could be introduced from the surface of the ZnSe layer. Since the ZnSe epilayer is subject to a compressive stress, dislocations from surface Frank-Read sources in ZnSe/GaAs heteroepitaxial system could be introduced. To release the compressive stress, half-loop perfect dislocations can form in the ZnSe epilayer thinner than the critical thickness. The dislocations move on the {111} glide planes of ZnSe crystal, and then reach the ZnSe/GaAs interface. The half-loop dislocations extend to the Shockley partial dislocations on two {111} planes. Then the two coupled stacking faults can form in the ZnSe epitaxial layer. Third, defects can be formed during nucleation at the ZnSe/GaAs interface. A lattice imperfection such as an antiphase boundary can be introduced in the ZnSe layer due to steps of the surface of the GaAs buffer layer. Dislocations can be introduced to terminate the unstable imperfection in ZnSe epilayer and extend on two {111} planes, then the paired stacking faults can also form in ZnSe epitaxial layer. Other possibilities are that the stacking faults nucleate at sites of incomplete oxide removal or other phase formation, such as Ga_2Se_3.

Similar structures of stacking faults are observed in other II-VI/GaAs systems.[56,113] The ternary alloy ZnSSe[56,113] and the quaternary alloy ZnMgSSe[113] grown on GaAs substrates show the paired stacking faults also in epilayer just above the interface of II-VI/GaAs. Nucleation of paired stacking faults at the upper levels of II-VI structures including ZnCdSe / ZnSSe / ZnMgSSe, however, is rarely found to occur. Therefore, the formation of stacking faults is extrinsic and most likely associated with the nucleation and/or initial growth stage of the II-VI layers.

It is expected that the stacking faults density could be reduced through the optimization of nucleation and initial growth of II-VI epilayers.[5,56] The lowest density of stacking faults in II-VI layers grown on GaAs substrates prior to this study was about 10^6 cm^{-2}. To allow fabrication without a single defect in a laser device, the density of

stacking faults must be below 10^3 cm^{-2}, which means three orders of magnitude decrease from the present level.[108] Substrate surface treatment prior to epilayer growth has been studied to obtain the optimized initial surface states in achieving the low stacking faults density.[56,57,61,62,114-116] Kuo *et al.*[56] found that ZnSe films grown on a Ga-rich GaAs substrate surface produce the highest density of stacking faults (10^8 cm^{-2}), while on an As-rich surface, the fault density is reduced when the initial stages of growth is in a layer-by-layer 2D growth mode.[56,57] The density could be further decreased by exposing the substrate to Zn flux for 1-2 minutes prior to ZnSe growth. The film/substrate interface roughness also plays a role in determining the density of stacking faults. Samples with a rough ZnSe/GaAs interface contain a high density of Frank partial dislocations of ~5×10^7 cm^{-2}. The roughness of the GaAs surface is believed to result from incomplete oxide desorption or improper surface treatment of the GaAs substrate that induces the formation of point defects. The effect of surface roughness can be minimized by growing an As-stabilized GaAs buffer layer on the GaAs substrate prior to the growth of II-VI films. At the optimized condition, which is a combination of As-rich surface, followed by an As-stabilized GaAs buffer layer and an 1-2 minutes Zn exposure prior to ZnSe growth, a stacking fault density as low as ~1×10^4 cm^{-2} can be obtained.[56,62] It is also found that the doping concentration affects the stacking fault density,[96,114,116] increasing with increasing nitrogen concentration.[114,116]

In contrast to above discussion, Ga-rich surface has also been reported as the preferred GaAs surface for ZnSe growth.[61,115] Qiu *et al.*[61] observed a dramatic interface state density reduction for ZnSe grown on an As-deficient GaAs epilayer from C-V measurements, while the exposure of Se flux to GaAs substrate at 500 °C is reported to yield a uniform and flat ZnSe epilayer grown at 300 °C.[115]

1.3.5 Ohmic Contacts

Making low-resistance ohmic contacts to p-type II-VI compounds is extremely difficult because of the very deep valence band position in these materials. Since the valence band maximum for ZnSe is about 6.4 eV below the vacuum level and no metal has a work function larger than 5.6 eV, it is impossible to make simple metal contacts with negligible Schottky-barrier heights to p-type ZnSe. Several non-conventional approaches to solve this problem have developed thus far:

(a) the use of a ZnTe/ZnSe graded contact scheme;[(117)]

(b) the use of a semimetallic HgSe grown directly on the top of the ZnSe heterostructure;[(118,119)]

(c) the growth of a highly nitrogen-doped, highly defective, low temperature layer of ZnSe;[(120)]

(d) injection of holes from a graded III-V layer on p-type GaAs designed such that the valence band offset is reduced.[(121)]

While these methods improved the device performance dramatically, further improvement of contact techniques is needed. The laser diode most recently reported by Sony with the record lifetime of 100 hours still had a operating voltage of 11V, far away from practical requirements.

1.4 Statement of the Problem

As discussed in the previous section, two major problems hindering the development of ZnSe II-VI light-emitting devices presently are the high density of extended defects in II-VI epitaxial layers grown on GaAs substrates, and the high degree of compensation in nitrogen-doped ZnSe at higher doping levels. The importance of hydrogen in the growth and processing of semiconductor materials and devices had led extensive studies in many important material systems, such as Si and GaAs. The

understanding and use of hydrogen provide additional controllability of material and device qualities. However, understanding of hydrogen in ZnSe-based material remains sparse. The remainder of this session outlines the principle problems addressed by this study.

(1) Can the twin-related defects be eliminated in ZnSe epitaxial layers and, if so, how does this affect the compensation process? It has been continuously debated whether the stacking fault defects related to microscopic twinning are intrinsic to the II-VI material system or are due to non-optimized growth conditions in MBE growth. Although progress has been seen in reducing micro-defects through optimization of the interface prior to II-VI epilayer growth reducing defect nucleation, a significant breakthrough has not been achieved yet. Since improvements in lowering micro-defects are proceeding, albeit slowly, it is generally believed that this defect property is not intrinsic to the material. In the development of substrate preparation techniques for epitaxial growth, atomic hydrogen has been proven very effective in removing surface contaminants for substrates such as Si, GaAs and InP. Since the defect density is very sensitive to substrate surface prior to the epilayer growth, a surface cleaned with atomic hydrogen may be favorable for the low defect density growth of ZnSe. Undoped and nitrogen-doped ZnSe films grown on GaAs substrates using both atomic hydrogen and conventional thermal cleaning are compared for micro-defect densities, which are revealed from the ultraviolet fluorescent microscopic images directly, and indirectly in photoluminescence spectra, where defect related transitions can be determined. Extended defects have been related to high nitrogen concentrations in ZnSe. However, whether heavy doping causes high defect density or high defect density results in compensation is not clear. The nitrogen-doped samples grown with atomic hydrogen cleaning and conventional thermal cleaning can provide useful information in understanding this relation.

(2) Does hydrogen account for nitrogen compensation in ZnSe? Hydrogen incorporation is observed in MOCVD, MOVPE and GSMBE grown nitrogen-doped ZnSe. The resulting ZnSe:N films are found high resistive, and N-H bonding is confirmed in layers grown by MOCVD and MOVPE. Thus hydrogen passivation of nitrogen occurs in doped films using those growth methods. Hydrogen is introduced into growth through the precursor or carrier gas during MOCVD, MOVPE, or GSMBE growth. The nature of the passivation process can not be determined since the hydrogen source contributed to passivation can not be uniquely determined. The fact that hydrogen can passivate nitrogen in ZnSe easily brings it to the topic of compensation in ZnSe. Is the passivation process occurring in MOCVD and GSMBE growth similar to compensation processes occurring in conventional MBE growth? If the two processes proceed in a same mechanism, then how does hydrogen affect nitrogen doping, in what form and to what level? The answers to those questions can not be deduced from observations that have been reported.

It is clear that hydrogen compensation of acceptors occurs in other material systems under standard MBE growth conditions.[159] It is conceivable that such a process is occurring for ZnSe as well. As the compensation process is complicated and may be the result of more than one contributed mechanism, it is necessary to isolate one source from the other in the identification of compensation signatures if possible. This can be realized in a conventional MBE growth of ZnSe since nitrogen and hydrogen sources can be configured with either an atomic or molecular form. A variety of configurations can be arranged to focus on one factor at one time. Thus the corresponding process of a specific compensation or passivation signature can be ultimately determined.

(3) What are the compensation mechanisms at work in ZnSe? Although several models have been proposed for the compensation mechanism in nitrogen-doped ZnSe, supportive evidence is not readily available for all cases. Se vacancies are necessary for

the formation of several compensating complexes in ZnSe. Although the observation of Se vacancies in MBE grown ZnSe thin films has been reported using ODMR technique, the question remains, " Are there enough Se vacancies in ZnSe to account for compensation at doping level as high as 10^{19} cm^{-3}? " In addition, nitrogen solubility in ZnSe is calculated to be $4x10^{19}$ cm^{-3}. Yet nitrogen concentrations as high as 10^{20} cm^{-3} are attainable in ZnSe, and nitrogen is found to occupy only substitutional sites by several techniques. Why are the additional nitrogen atoms not effective as dopants? Consideration of data collected in three separate laboratories, that of Prof. Giles, Halliburton, and Myers, indicate a consistent picture emerging. By using electron paramagnetic resonance measurement in Prof. Halliburton's laboratory, a level of 10^{17} to 10^{18} cm^{-3} Se vacancies was found in ZnSe samples. PL measurements in Prof. Giles' laboratory implied that a deep donor at a level about 0.3 eV below conduction band may contribute to a DAP emission in heavily nitrogen-doped ZnSe. Fourier transform infrared measurement indicated that substitutional nitrogen must undergo a change in charge state at very high doping levels. A compensation process in nitrogen-doped ZnSe was suggested based on these results.

Through systematic investigation of hydrogen effects in nitrogen-doped ZnSe grown by MBE, phenomena related to hydrogen and ZnSe fundamental issues are studied in detail. Effects of hydrogen in the processing of ZnSe grown by MBE are clarified and the compensation mechanisms are discussed from observations of Se vacancies and substitutional nitrogen atoms in ZnSe. The experimental details are discussed in Ch. 3 through Ch. 5, and the conclusions are summarized in Ch. 6.

CHAPTER II

GROWTH AND CHARACTERIZATION

2.1 MBE System

An MBE system was designed and built in the Physics Department at West Virginia University for the growth of II-VI and III-V semiconductors. The system has two vacuum chambers: a load lock for sample introduction, and a main chamber for film growth. A transfer arm is used to handle sample loading and unloading between the load lock and main chamber. The chambers are constructed from stainless steel and isolated by gate valves. The load lock, which bridges the atmosphere and UHV environment in the growth chamber, is normally vented with dry nitrogen gas and can be pumped down to 10^{-7} Torr in less than 30 minutes using a Varian Turbo-V250 pump. The main chamber is pumped down to 10^{-6} Torr using the Turbo-V250 pump through the load lock chamber. After that, the gate valve between load lock and main chamber is closed, the main chamber pumping is then taken over by a CTI-Cryogenics CT-8 cryopump and a Varian StarCell ion pump. A vacuum at 10^{-8} - 10^{-9} Torr is obtained. The residual gases in the vacuum are monitored by an UTI-100C quadruple mass spectrometer. The residuals in the vacuum are mainly water vapor (atomic weight 18), nitrogen (28), and carbon dioxide (44) since these atmospheric gases are easily adsorbed on the stainless steel surfaces. If on any occasion the vacuum system has an air-leak, the mass spectrometer will reveal a spectrum dominated by nitrogen, water, and oxygen (32), with a N_2/O_2 peak ratio of about 7. A bakeout of the main chamber at elevated temperatures (typically 100 -150 ºC) is necessary to desorb these atmospheric gases from the chamber walls. After bakeout, a typical vacuum in the main chamber is about 10^{-10} - 10^{-11} Torr. Hydrogen (2) and carbon monoxide (16) are the typical dominant residual gases. The mass spectra of an unbaked vacuum system is shown in Fig. 2.1(a), compared with that of

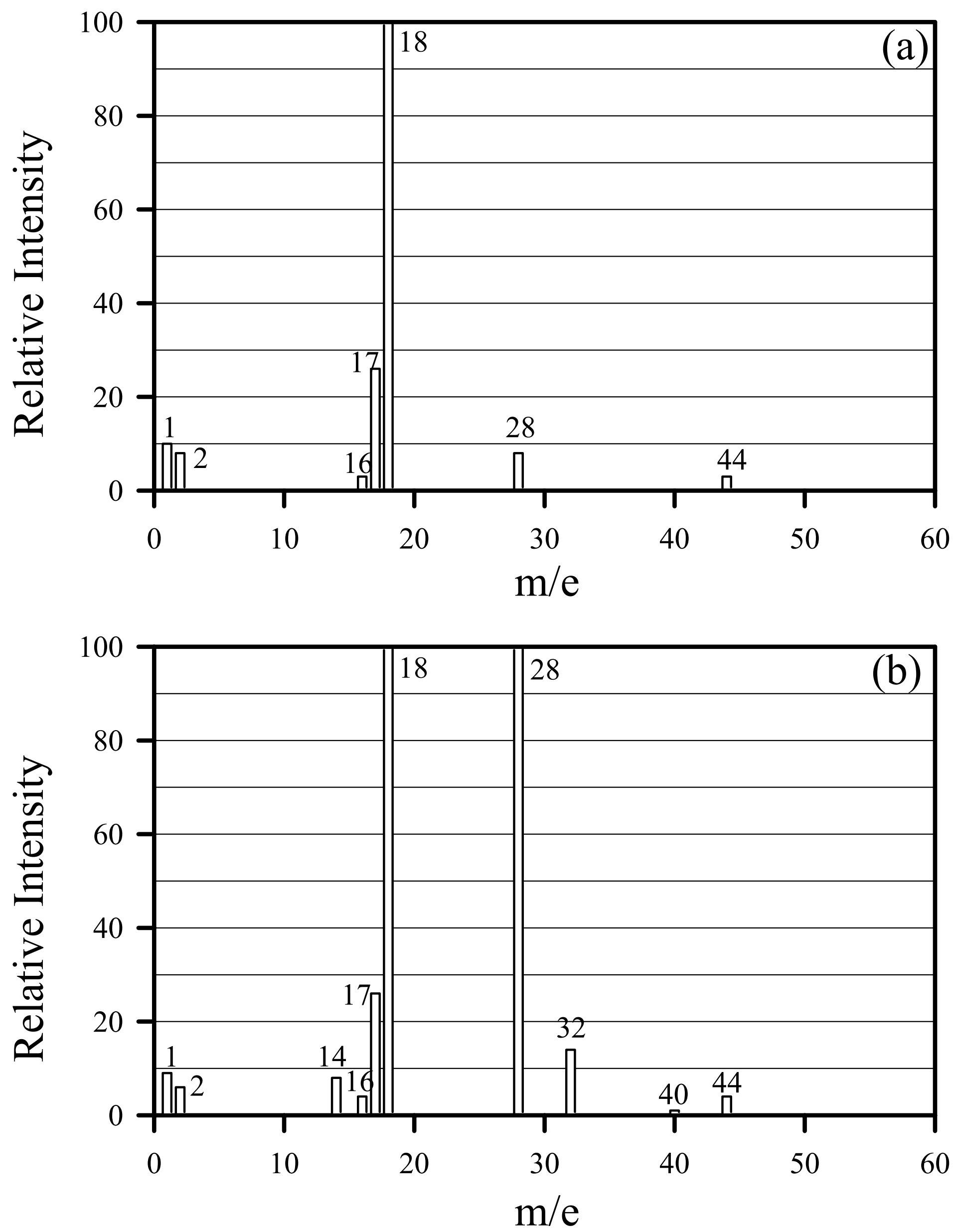

Fig. 2.1 Mass spectra of (a) an unbaked vacuum system, and (b) a vacuum system with the signature of an air-leak.

a vacuum system with an air-leak in Fig. 2.1(b). During growth, typical background pressure is 10^{-9} to 10^{-10} Torr depending on growth conditions.

2.1.1 Chamber and Source Flange Design

Fig. 2.2 shows the front view of the MBE system. A rule of thumb in designing a custom MBE system is to provide the maximum capability in growth and characterization when it is possible and/or available. A schematic diagram of the MBE system is shown in Fig. 2.3. The main chamber body is 22.50" high and 14" in diameter. It has a hemisphere on the top and a 17.25" OD wire sealed flange at the bottom for housing the source ovens. The chamber sits on the supporting frame inclined 30° with respect to the horizontal. This design provides the ability to use liquid source material, which would be precluded in the upper source ports if the chamber was not incline. A reference point, which is the center of growth surface on substrate, is along the central axis of the chamber at 9" from the top and 17.5" from the bottom. A reference plane is the plane perpendicular to the central axis of the chamber and containing the reference point. A 10" flange port on the side of the chamber (30° off chamber wall) directed to the bottom of the supporting frame is for pump connections. The cryogenic pump and ion pump are connected to this port through a 5-way cross. Another 10" flange port on the chamber side with an axis perpendicular to the chamber wall and 5" below the reference plane, is for the housing of the mass spectrometer and source shutter. A pair of ports on the opposite side along a chamber diameter on the reference plane are used for sample transfer and housing the growth shutter. A 6" flange port is connected to the load lock chamber, and an 8" flange port located on the opposite side is contains the growth shutter and liquid nitrogen inlet and outlet for the substrate cooling shroud. A second pair of ports, which also lined up on the opposite sides of a chamber diameter, are for the RHEED setup. The 4.5" flange port, which is 1° off the reference plane, is for the

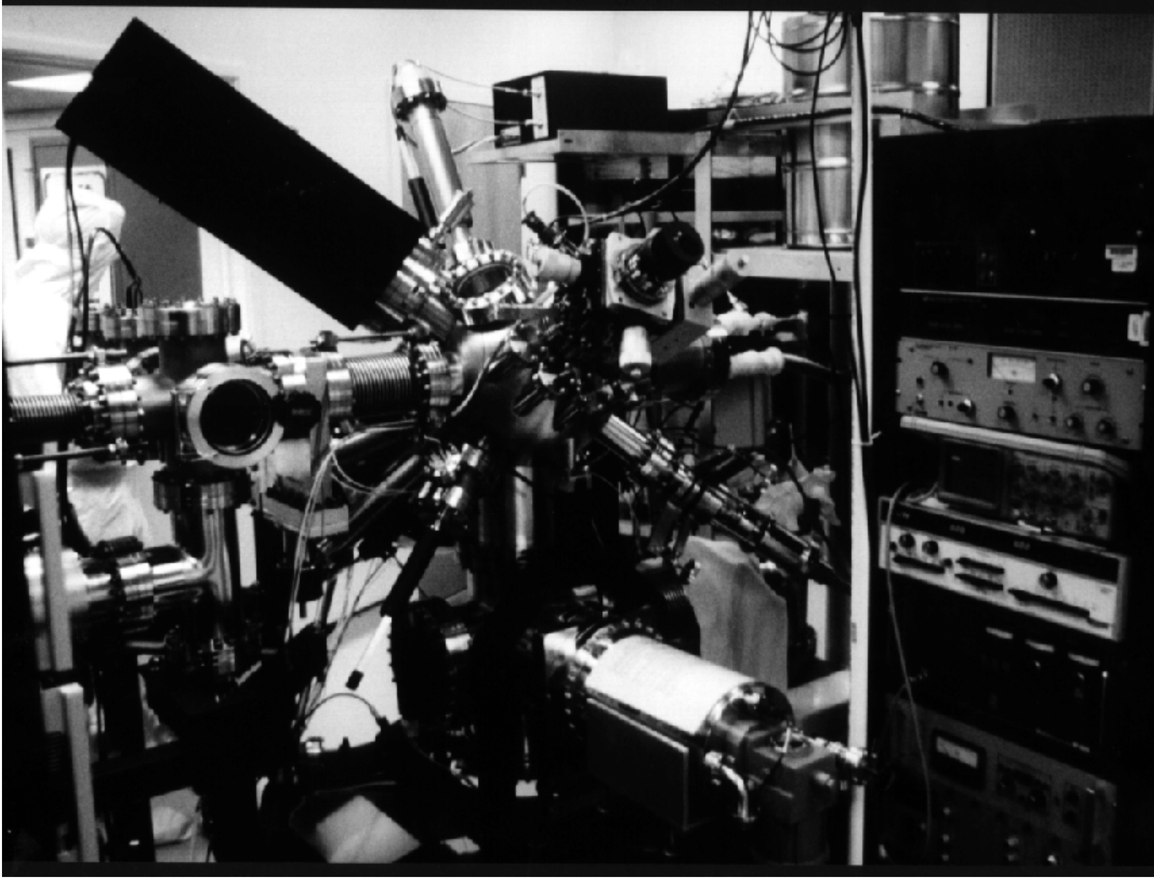

Fig. 2.2 Front view of the MBE system used in this study.

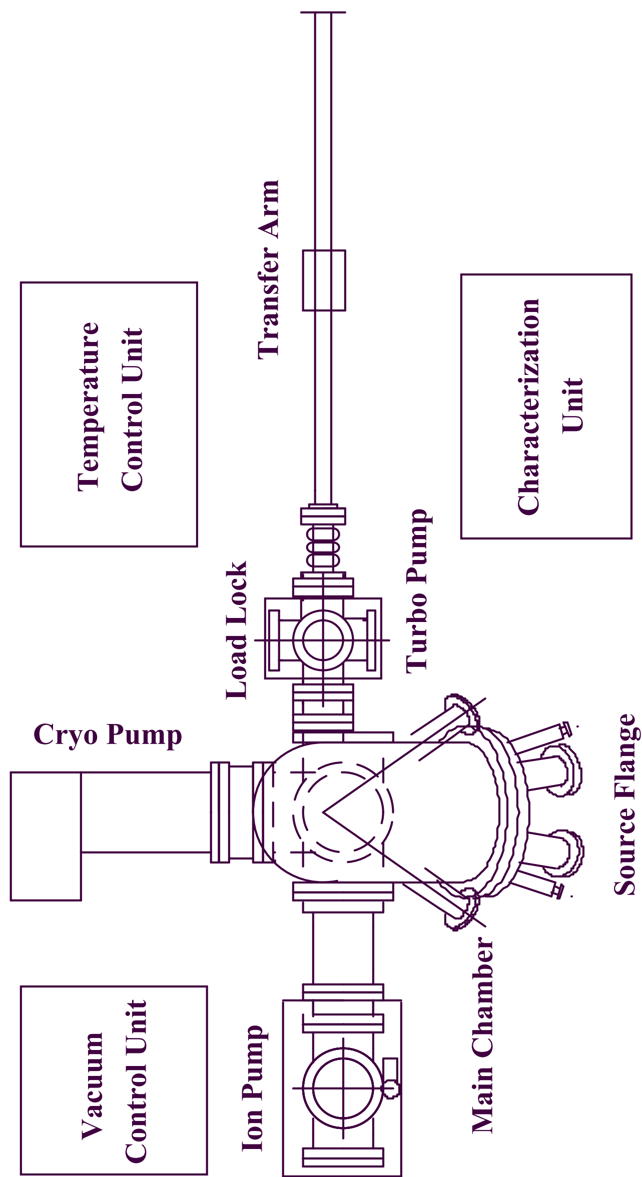

Fig. 2.3 Schematic diagram of an MBE system. In addition to the main chamber, source flange, load-lock and pumping system, other important components include the temperature control unit, the vacuum control unit and the characterization unit.

housing of RHEED electron gun. The opposite 8" flange port, which is 2" below the reference plane, is used for mounting the fluorescent screen for the RHEED diffraction pattern display. A third pair of ports on the opposite sides of the chamber diameter are for ion gauges. One of the two 4.5" flange ports, 2" below the reference plane, is mounted with the beam flux monitor (BFM) which measures source flux just before the substrate. A 6" flange port on the hemisphere, which is 45° away from the reference plane, serves as a viewport for sample loading and unloading. Three pairs of 4.5" flange ports, each of which is 35° off the chamber wall with its central axis directed to the reference point, are designed for the increasing capability of growth and characterization of the system, such as photo-assisted growth, gas source MBE and *in-situ* optical measurements. On the top hemisphere of the chamber, a 6" flange port is used to introduce the substrate manipulator, which allows translation in the x, y and z directions as well as rotational operation for the substrate block. Six 2.75" flange ports on the hemisphere on a 11" diameter circle provide electrical or mechanical feedthroughs when necessary.

The source flange is an important part of an MBE system. It provides the housing for source ovens, and also the control of growth shutters. Fig. 2.4 shows a cross-view and bottom-view of the source flange. Two 4 5/8" and five 3 3/8" flange ports are arranged on the 17.25 " wire sealed flange, each furnished with an oven for a solid source. The central axis of each off center port (two 4 5/8" and four 3 3/8") is 12° off the chamber central axis, and the two axes meet at the reference point. Due to the large heat radiation from the ovens, appropriate cooling is necessary. A two-part cooling shroud is used for this purpose. The ovens are isolated from each other in the lower shroud by stainless steel walls. The inner cavity is cooled by circulated ethylene glycol and water mixture held at 10 ºC using a NESLAB HX-200 cooling system. The top shroud is a hemispherical stainless steel double wall container with a 4" diameter opening on its top

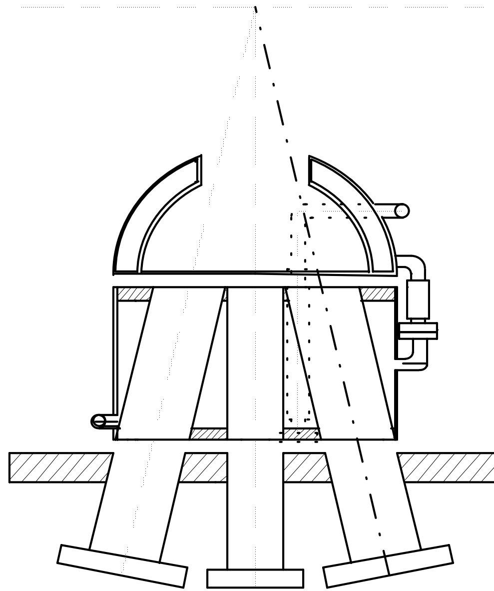

(a)

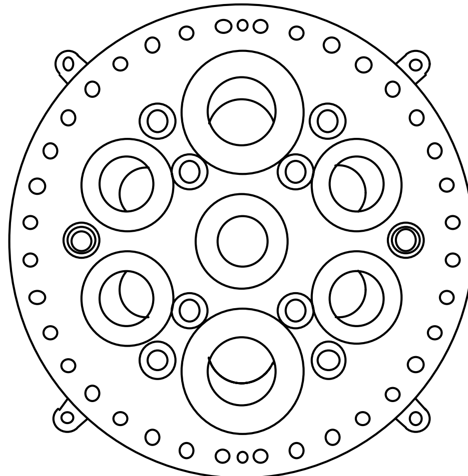

(b)

Fig. 2.4 Diagram of an MBE source flange (a) a cross sectional view with the cooling shroud for ovens also shown, and (b) a bottom view where a maximum of seven ovens can be installed.

connected to the lower shroud to further disperse heat from ovens, and can also reduce system contamination by collecting excess materials from the furnaces. There is 0.5" gap between the top and lower cooling shroud. Oven shutters are set in front of each oven just above the opening on the lower shroud. Shutters are separate from each other and operate independently by the shutter handles beside each oven. An overall source flux shutter is set in front of the top shroud opening. The distance between the front plate of the lower shroud and the reference plane is 11", which indicate that the path from the front of the source to the growth front is about 12". The solid source ovens are either low temperature or high temperature cells (EPI-40-M) depending on the source material used. For both Zn and Se, low temperature cells are used because of their high vapor pressure at low temperatures, while for Ga, high temperature cell is used because of its low vapor pressure (Although not specifically discussed in this study, GaN has also been successfully grown in this system). Typical vapor pressure and oven temperatures for required flux are listed in Table 2.1 for several source materials normally used in our growth. After loading the source material into the system, the chamber needs to undergo a bakeout, and the ovens outgassed at elevated temperatures. Prior to the first growth from a newly loaded source material, the source is run at a flux higher than the normal growth flux for at least two hours to minimize subsequent contaminant incorporation into layers. Growth is started after the source fluxes are stabilized as checked by the beam flux monitor for each growth.

2.1.2 Pumping System

To achieve an ultrahigh vacuum (UHV), it is essential to have the right pumping system. While any pressure less than 10^{-8} Torr is classified as UHV,[122] the normal background pressure in an MBE chamber is in the range 10^{-10} to 10^{-11} Torr. One cannot expect one pump to take a system from atmosphere to the high or ultrahigh vacuum

Table 2.1 Vapor Pressure, Oven Temperature and Beam Equivalent Pressure (BEP) of Typical Source Materials Used in MBE Growth

Source	Temp. (°C) for Vapor Pressure (Torr)			Typical Oven Temp. for Growth	BEP
	10^{-5}	10^{-4}	10^{-3}	(°C)	(x 10^{-7} Torr)
Zn	209	247	292	300	8
Se	133	164	199	190	7
Te	242	280	323	310	6
Ga	817	907	1007	1035	7

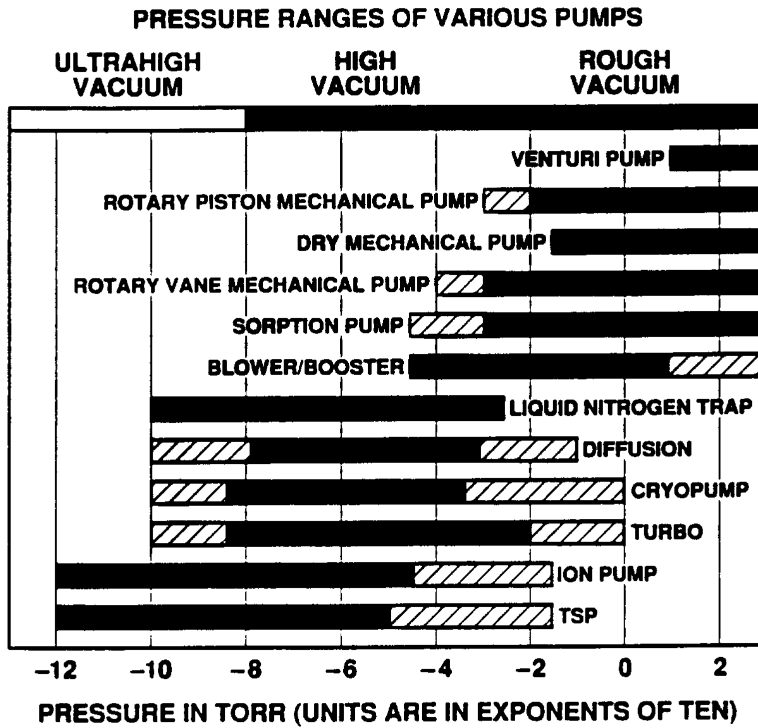

Fig. 2.5 Operating pressure range for a variety of vacuum pumps.

range. Two or more pumps must be used to reach and sustain a particular pressure. Fig. 2.5 shows typical operating range for a variety of vacuum pumps, and in Table 2.2, pumps used in our MBE system are listed. As stated earlier, the system is rough pumped to the range of 10^{-6} Torr by a turbomolecular pump which has a mechanical roughing pump as a foreline pump. Then the pumping of the main chamber is taken over by a cryogenic pump to the range 10^{-8} to 10^{-9} Torr range. If the system is opened to air (typically vented with high purity N_2 gas), a bakeout performed at temperatures between 100 to 150 °C is needed to remove adsorbed gas species. The background residual gases are monitored by mass spectrometer. A typical mass current of residual species after bakeout is listed in Table 2.3. The ion pump and titanium sublimation pump (TSP) are usually opened to the chamber when the system pressure is below 10^{-8} Torr. After the bakeout turned off, the system pressure is in the mid-10^{-10} Torr range. The residual species are mainly light gases such as H_2, H_2O, and N_2.

A liquid nitrogen cooling shroud, which is designed to surround the substrate block to take the heat load released by the substrate heater, is shown in Fig. 2.6. A 10" diameter molybdenum (Mo) plate with a 3" diameter opening at the center for substrate block operation, is bolted to a semi-cylindrical stainless steel shroud using indium foil in between for the best thermal conductivity. The liquid nitrogen inlet (fill in) and outlet (vent), and the shroud supporting rods are fitted in a 8" flange port. All connections are made with UHV joining techniques and leak-tested before adding onto the system. The shroud has a ~ 4-liter liquid nitrogen capacity and fills with liquid N_2 through the inlet which is connected to a 20-liter liquid nitrogen tank sitting beside the main chamber. The temperature at the Mo plate is monitored by a thermocouple residing on the front surface of the plate, and controlled through a solid state relay which signals a solenoid valve to vent air and let liquid in when the temperature is above the set point. The

temperature at the Mo plate is normally -190 °C when the shroud is filled with liquid nitrogen. Similar

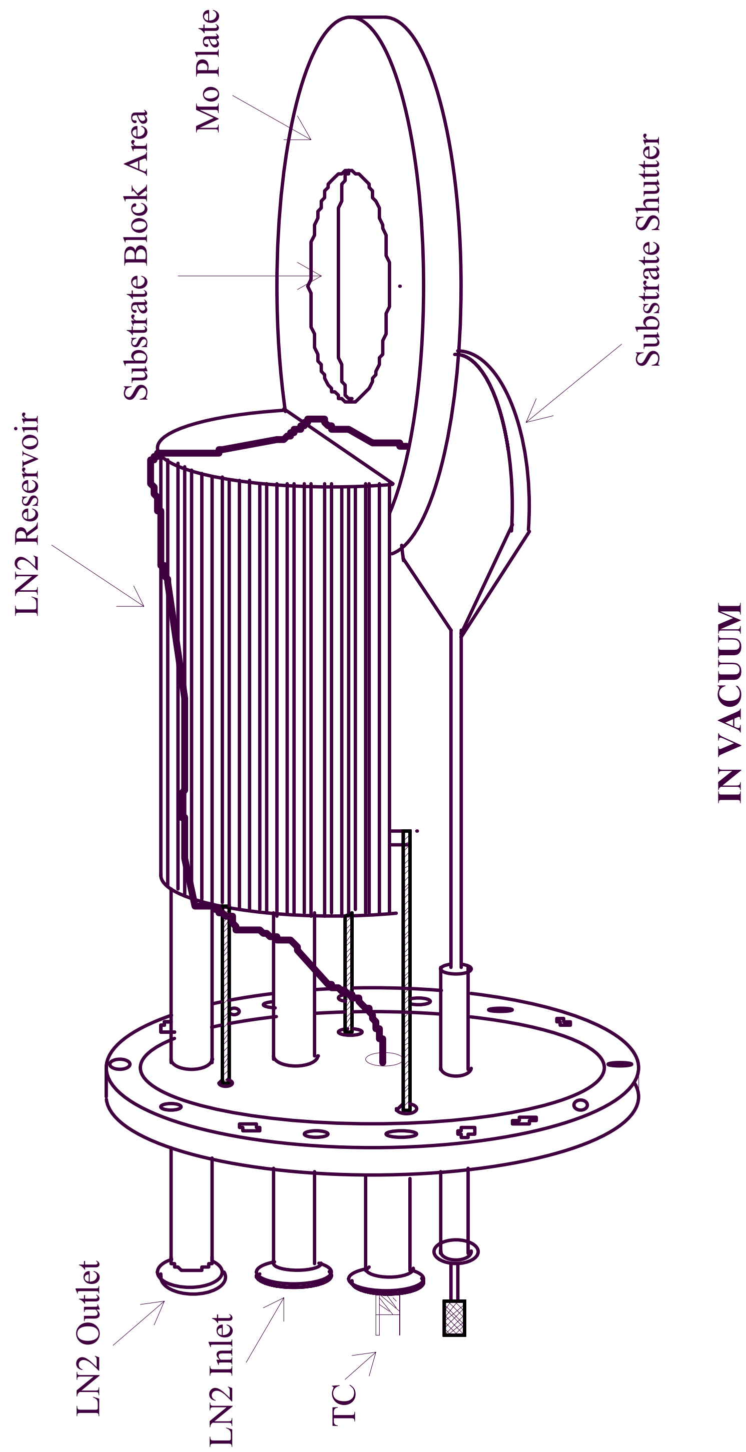

Fig 2.6 Schematic Diagram of Substrate Cooling Shroud

Table 2.2 Vacuum Pumps Used in the MBE System at WVU

Pumps	Model	Speed
Turbomolecular pump	Varian Turbo-V250	250 liter/s
Cryopump	Cryogenics Cryo-Torr 8	1000 liter/s
Ion pump	Varian StarCell VacIon	400 liter/s
Titian sublimation pump	Varian TSP	1000 liter/s

Table 2.3 Mass Current of Residual Gases in Vacuum System After Bakeout

Mass	Current (x 10^{-10} Amps)	
	(P_{sys} ~ 10^{-9} - 10^{-10} Torr)	(P_{sys} ~ 10^{-10} - 10^{-11} Torr)
2	6.0	2.8
12	2.5	0.3
14	0.2	0.2
16	1.2	0.5
18	0.6	0.3
28	2.5	1.0
32	.04	0.02
44	0.5	0.1

to a cryotrap, the substrate shroud also serves as an additional pump to the vacuum system, especially for water and carbon dioxide (CO_2). The system pressure with the substrate shroud cooled is in low 10^{-10} to 10^{-11} Torr range. The current of mass species measured by the mass spectrometer is also shown in Table 2.3 for this pressure range.

The pumps used in an UHV system, such as cryopump, ion pump and TSP, are mostly gas capture pumps.[122] They pump gases by either absorbing and condensing (cryopump) gas species or chemically reacting with gas molecules (ion pump and TSP), therefore, the gases are stored in the pump. The "clean up" of pumps periodically is necessary to keep the pumping efficiency. The ion pump is usually not used to pump heavy gas loads (the ion pump valve is closed when gas sources are used), and can be cleaned through occasional bakeout. The cryopump works in a wider pressure range and heavy gas loads. Thus the gas storage can be high in a short time depending on the growth details. To release the gas storage, a regeneration is performed. It is recommended to regenerate the cryopump every two weeks for routine growth. However, if extensive gas sources are used, such as for the growth of GaN or ZnSe:N,H, frequently checking the cold head temperature is necessary. A cold head temperature above 11 K is an indication of high gas storage in the pump and regeneration is required.

2.1.3 Substrate Manipulation

A substrate is mounted on the substrate block. A substrate manipulation system includes sample loading/unloading, heater and temperature control, and a combination of translational and rotational movement for proper adjustment. The substrate block is made from 1.25" diameter Mo rod. It consists of two fixed parts. The first part is a disk with 1.25" in diameter and 0.52" in height, which is used for mounting substrate on the front surface. The back of this part is an open space where the substrate heater resides.

On its side wall, four pins match the bayonet slot positions on the second part of the block for

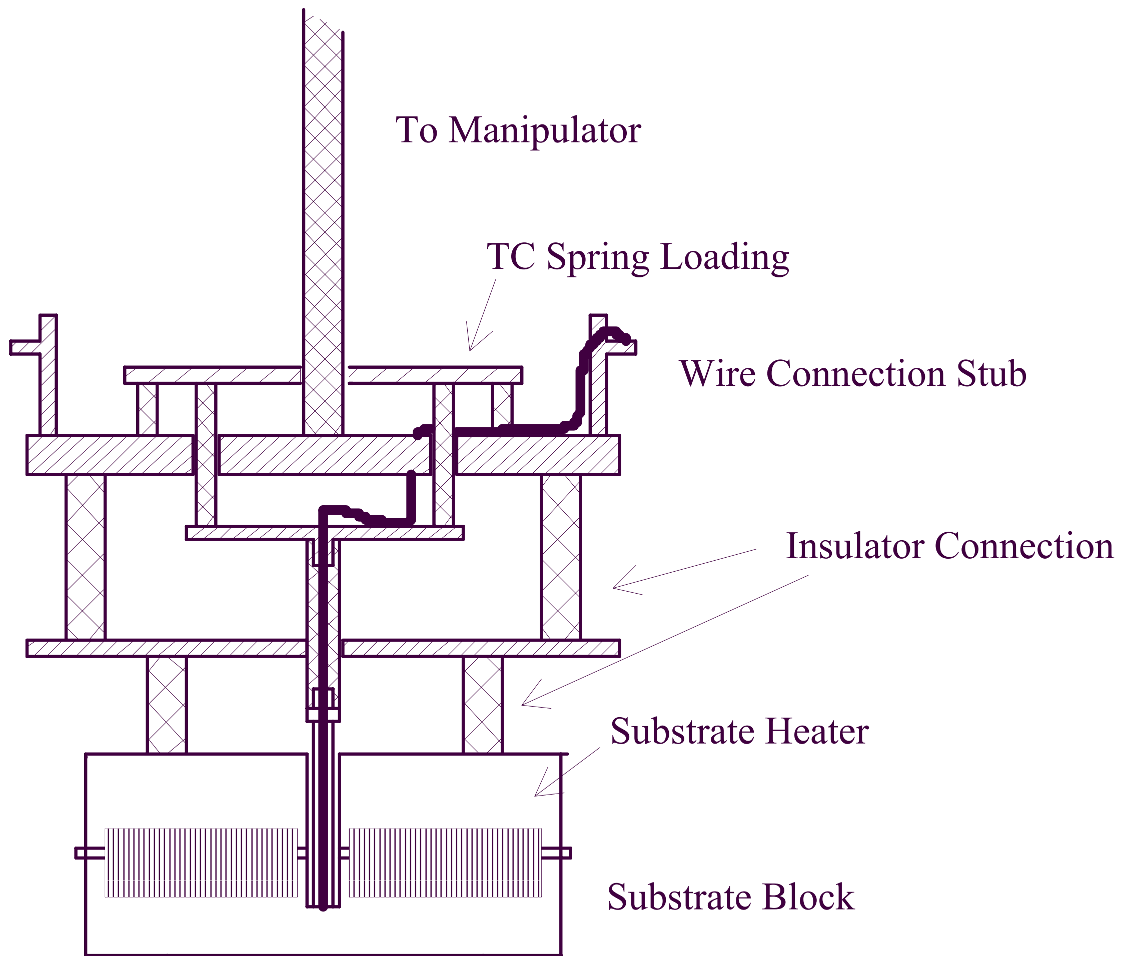

Fig. 2.7 Assembly diagram of substrate block.

locking the two parts together. At the center of its backside, a 5/16" OD, 3/16" ID, and 1/8" deep hole is added above back surface for placing a thermocouple to monitor the temperature of the substrate during growth. The front surface for mounting substrates is flat within 0.002". Additional pins and holes are added on the edges of the block for alignment or mask mounting purpose. The second part, which is a counterpart of the first part, is used for substrate heater mounting. It is 11/16" high with a 3/16" thick back plate as the heater base. The substrate heater is wired on a pyrolytic boron nitride (PBN) disk using tantalum wire which is then sandwiched between two other PBN disks which serve as insulators and heat diffusers. The heater disks are mounted on the heater base using tantalum wire. The substrate block is then bolted to a supporting Mo plate which is connected to the manipulator shaft. A spring-loading mechanism is used for the substrate thermocouple on the back of substrate block to ensure a good contact. Connections between substrate block, supporting plate, thermocouple spring load and heater power supply plate are both thermally and electrically isolated using ceramic insulators. An assembly diagram for the substrate block is shown in Fig. 2.7.

The substrate motion is provided by a Huntington PM-600-TR vacuum precision manipulator, which can move ±12.5 mm in both X and Y axis, ±25 mm in Z axis and 360 degree rotational. Substrate loading/unloading is completed by a combining operation of transform arm and manipulator. A special device is designed and added to the end of the transfer arm. Inserting the transfer arm into substrate block position, one can use the manipulator to move the substrate block into the device, and rotate to lock/unlock the substrate block.

2.1.4 Nitrogen Source and Hydrogen Source

An rf plasma nitrogen source is integrated into the MBE system. The Model CARS25 Atomic/Radical Beam Source (Oxford Applied Research Ltd.) operates by an

electrical discharge created from inductively-coupled RF excitation at 13.56 MHz.[123] The source is cooled with cryogenic (80 K) nitrogen gas. Atoms are produced by dissociation in the PBN discharge chamber and can escape into the vacuum environment along with undissociated molecules via an array of fine holes in the beam aperture plate. The electric potentials are such that negligible currents of ions or electrons (< 1μA) escape from the discharge during normal operation of the source. Dissociated atoms undergoing wall collisions in the discharge chamber exhibit a low recombination coefficient and may also ultimately contribute to the radical beam flux. The pressure in the discharge chamber is sufficiently low that atom-gas collisions are minimal over the dimensions of the discharge chamber. There is a critical pressure above which breakdown will occur. The breakdown pressure varies from gas to gas according to the ionization potential of the gas. Consequently, for a fixed source aperture conductance the flow rate necessary to achieve breakdown will vary from gas to gas. Once breakdown has occurred the flow rate can be throttled down considerably while maintaining a discharge. Thus, there is a pressure window within which a plasma discharge is sustained for a fixed aperture and operating power.

The source can be operated continuously up to 600 W. Care must be taken when operating the source at high power. An increase of reflected power due to impedance mismatch will result in overheating of the matching unit and RF circuitry and cause severe damage to the source. The discharge is monitored by an optical emission detector since the voltage output from the optical emission detector is proportional to the discharge efficiency. Therefore, a voltage output increase is observed when the plasma power is increased. However, a saturation power is found for some flow rate. After the saturation power is reached, further increase of the flow rate will result in a voltage decrease.

The source has been characterized for its optical emission spectra. A typical

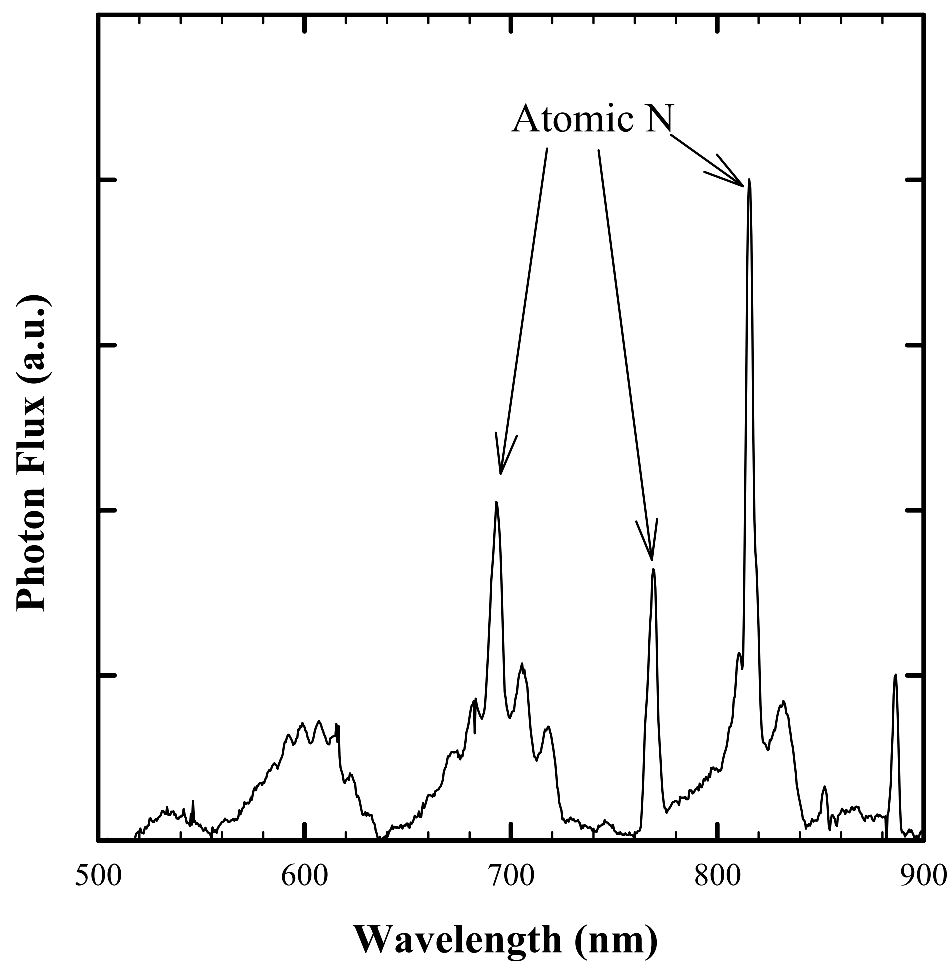

Fig. 2.8 Emission spectrum of rf plasma atomic/radical nitrogen source.

spectrum is shown in Fig. 2.8, which is similar to those observed by other researchers.[82] The strong peaks belong to atomic nitrogen emission. That indicates the high nitrogen cracking efficiency of the plasma source and explains the success of atomic nitrogen source in p-type doping of II- VI wide bandgap semiconductors.

For p-type doing of ZnSe, typical operating power of the plasma nitrogen source is ~200 W at a system pressure of ~$2x10^{-6}$ Torr using an aperture with 9 x 0.2 mm holes. The voltage output from the optical emission detector is ~2.1 V. ZnSe:N films grown under these parameters exhibit a high level of nitrogen doping concentration ranging between $1x10^{18}$ cm^{-3} to $8x10^{19}$ cm^{-3}. Further reduction of either pressure or plasma power would cause the plasma to become unstable.

An EPI-AHS-L atomic hydrogen source was added to one of the 4 1/2" flange port. The EPI atomic hydrogen source is a gas source effusion cell used to generate atomic hydrogen by thermal cracking of molecular hydrogen on a heated tungsten filament.[124] The source is water-cooled on the mounting flange and feedthrough regions due to the high operating temperatures. The filament is heated using a current-regulated power supply, which usually operates at 9.5 Amps (note the upper limit for current for the tungsten filament is 10 Amps). The current at 9.5 Amps corresponds to a power of 430 W which produces a filament temperature of about 2200 °C. Fig. 2.9 shows the cracking efficiency of the thermal cracker for hydrogen, taken from the operating manual. Thus, about 10% atomic hydrogen (corresponding to 5% H_2 cracking efficiency) is obtained at the above operating temperature. The hydrogen flow used for ZnSe growth results in a system pressure ~$1x10^{-6}$ Torr, while $2x10^{-6}$ to $6x10^{-6}$ Torr are used for substrate cleaning.

For a $2x10^{-6}$ Torr H_2 partial pressure measured by the system ion gauge, the corresponding beam equivalent pressure at the substrate is about $3x10^{-6}$ Torr. After

considering the ion gauge sensitivity for H_2 (which is about a factor of two larger than the

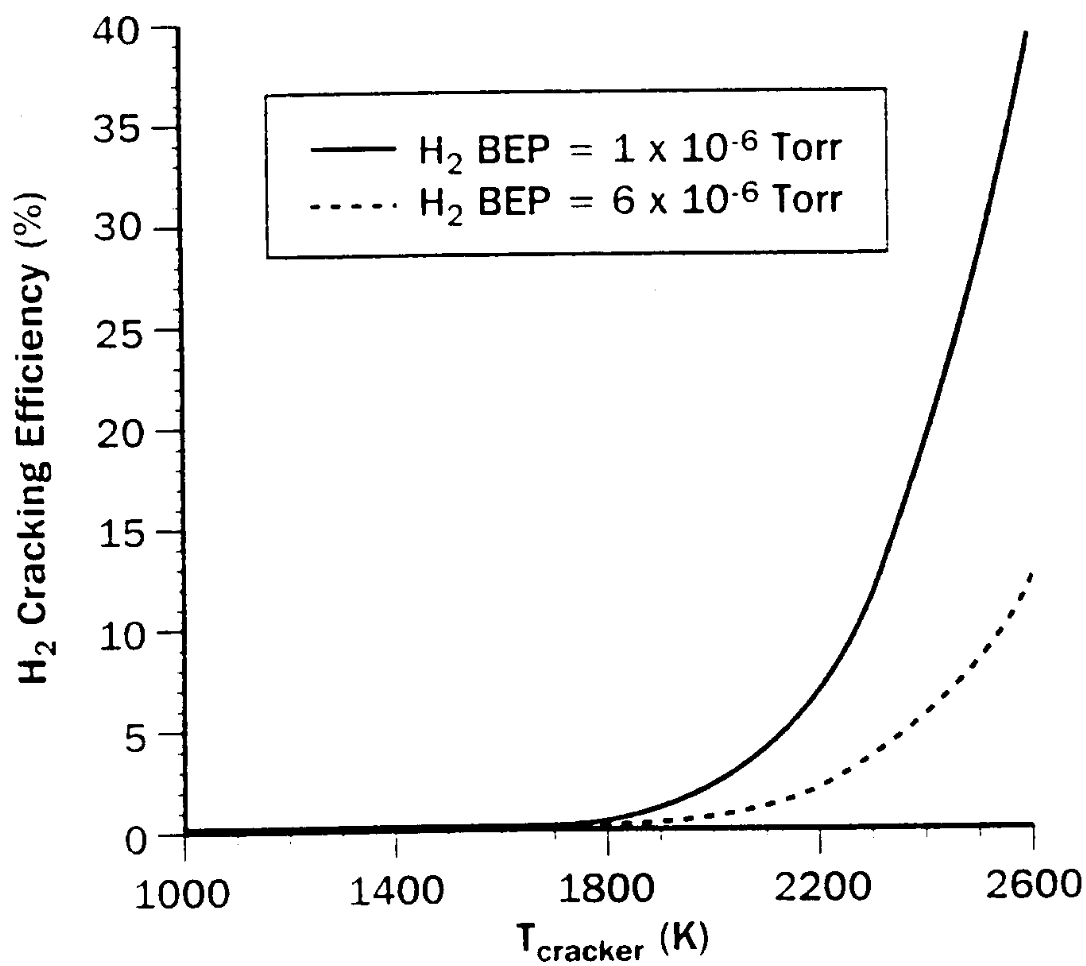

Fig. 2.9 Cracking efficiency of the atomic hydrogen source (Taken from Ref. 124).

reading pressure which is calibrated with N_2), the real pressure from the H_2 flux is about $6x10^{-6}$ Torr in the substrate area. The impingement rate of a gas species with mass M and partial pressure P at temperature T can be estimated by[168]

$$A = 3.535 x 10^{22} \frac{P}{\sqrt{MT}} \quad (2.1)$$

where P is in Torr, and T is the absolute temperature. For H_2 with the pressure of $6x10^{-6}$ Torr at room-temperature (300K), the impingement rate is $8.6x10^{15}$ sec^{-1} cm^{-2}. Thus, the impingement rate is about $8.6x10^{14}$ sec^{-1} cm^{-2} for atomic hydrogen at the above pressure. Assuming a unity accommodation coefficient and a separation d between surface molecules, the time to form a monolayer can be estimated by[169]

$$t = \frac{1}{Ad^2} \quad (2.2)$$

For d = 3 Å, the monolayer time is ~ 1.5 sec for atomic hydrogen at the system pressure of $2x10^{-6}$ Torr.

2.2 Characterization

In order to understand material qualities and the relation with its growth history, analysis of the material from various aspects and at different stages is required. Characterizations are also made after growth, which provides information of the material after completion of the growth. The characteristics of MBE growth, however, provide possibilities of evaluating material quality during the growth, i.e., *in-situ* characterization, which by bridging growth control and the after-growth properties of materials, will give

useful feedback to the quality control for growth. One of these techniques is RHEED, since the diffraction patterns directly relate to the surface reconstruction which result under certain growth condition. The mass spectrometer is always helpful in a vacuum system since it monitors species presented in the vacuum and gives reference for possible impurities contained in the material. For after-growth analysis, i.e. *ex-situ* characterization, techniques are simplified because the setup is not restricted to the growth facility. In this study, photoluminescence measurement is used first because it is able to give a quick survey of sample quality and impurity or defect signatures. Other measurements include FTIR, SIMS, microscopy (optical and AFM), Hall and X-ray diffraction.

2.2.1 *In-situ* Techniques

2.2.1.1 Reflection High Energy Electron Diffraction (RHEED)

In reflection high energy electron diffraction an electron beam with energies between 5 and 100 keV is incident onto a crystal surface at low grazing incident angles (0.1 to 5°, depending on electron energy).[125] The scattered electrons (diffracted by the lattice) impinge on a phosphor screen and the resulting image can be recorded by a camera. The high energy and small incident angle force the electron beam to penetrate only few monolayers near the surface. Therefore, RHEED is a surface-sensitive technique.

The principle of RHEED can be understood analogous to the kinematic scattering theory. For a plane wave with wavelength λ incident at an angle θ_0 on a one-dimensional grating with line spacing d, the diffraction maxima occur at angles θ_x when rays emanating from successive grating lines scatter in phase, i.e., their path difference is an integral number of wavelength. The diffraction equation,

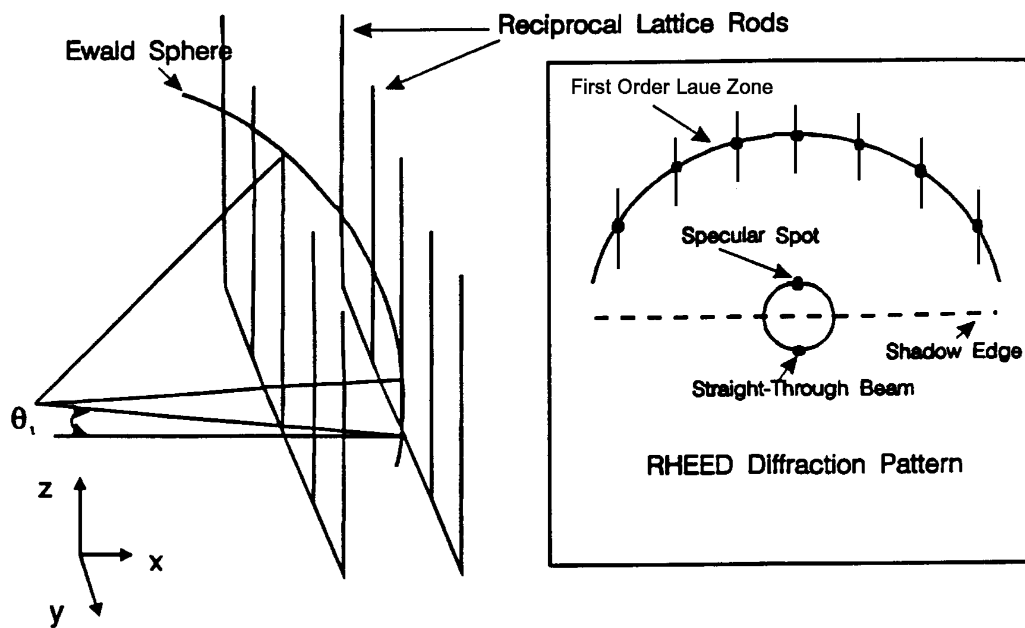

Fig. 2.10 Schematic diagram of Ewald sphere intersecting with a 2-D reciprocal lattice for a perfect two-dimensional surface (Taken from Lagally in Ref. 127) .

$$n\lambda = d(\cos\theta_x - \cos\theta_0) \qquad (2.3)$$

defines conditions where the maxima occur. For a spacing of ~1Å in a crystal surface, to observe high-order diffraction maxima (n>1), the source wavelength needs to be very short. The wavelength of an electron with energy 10 keV is ~ 0.12 Å, therefore, the high-order diffraction can be observed from a crystal surface. For a fixed incident beam energy and a fixed incident angle, each family of rows diffracts radiation at the appropriate exit angle θ_x. If a fluorescent screen is positioned to intercept these scattered beams, a diffraction pattern having the symmetry of the surface or overlayer unit mesh will be observed. If the energy of the incident beam or the incident angle is changed, the diffraction angles θ_x adjust to continue to satisfy the diffraction equation. For example, if the beam energy is increased, the entire pattern will appear to "shrink" because θ_x becomes smaller for all beams. It is easy to understand then, for each surface structure which has its unique surface row "grating", there is a corresponding diffraction pattern existing, which is the fundamental reflection for that surface structure. Other diffraction patterns from a same crystal structure with derived surface structure due to reconstruction can be identified by comparing with the fundamental reflections.

RHEED patterns can also be interpreted from the reciprocal lattice rods intersection with a Ewald sphere as it originated from the development of X-ray diffraction theory.[126] The reciprocal lattice is the representative of a crystal structure in wave-vector space (k_x, k_y, k_z). For one-dimensional (1-D) lattices, the reciprocal lattice is a series of planes perpendicular to the line of scatters and spaced $2\pi/d$ apart. For two-dimensional (2-D) lattices, the reciprocal lattice is a 2-D array of infinite rods perpendicular to the 2-D plane. The rod spacings are equal to 2π/(atomic-row spacing). For three-dimensional (3-D) lattices, the reciprocal lattice is a 3-D array of points whose separations are inversely related to the separations of crystal planes. The Ewald sphere

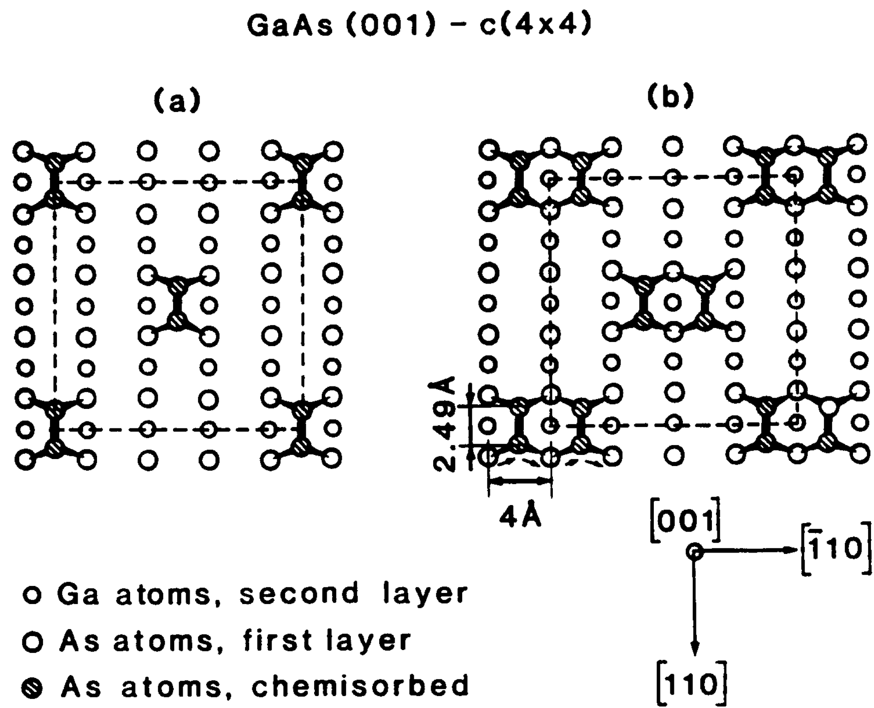

Fig. 2.11 Schematic diagram of a GaAs (100)-c(4x4) surface reconstruction (a) with additional 25% As coverage, (b) with additional 50% As coverage (Taken from Ref. 9).

provides the schematic description of the conservation of energy (diffraction is an elastic scattering, thus the incident and exiting beams have the same energy), the radius of the Ewald sphere is inversely proportional to the wavelength λ which is defined by the electron beam energy. The intersection of the Ewald sphere and the reciprocal lattice rods gives a graphical solution to the diffraction equation and therefore yields the diffraction pattern. Fig. 2.10 shows the schematic of Ewald sphere intersecting with a 2-D reciprocal lattice. As the energy of the incident beam or the angle of incidence varied, the radius of the Ewald sphere or its orientation relative to the rods changes, consequently also changing the points of intersection with the rods. The directions of the outgoing vectors define the directions of the diffracted beams.

The surface-sensitive nature of RHEED enables it to become a very useful diagnostic tool in monitoring and controlling surface structure changes with the growth parameters. It is possible to obtain information on surface structure, microstructure, and smoothness from both the symmetry of RHEED patterns and the degree of streakiness.(125,127) The growth rate can be monitored by the RHEED intensity oscillation of a particular diffraction spot (usually the specular spot).(127)

The diffraction pattern changes when a surface atomic arrangement is changed, i.e., reconstructed. Reconstruction is a consequence of the attempt of the surface to lower its energy by eliminating dangling bonds created by the formation or existence of the surface, and is prevalent in semiconductor and ionic materials and also a number of metals.(125) Reconstruction always creates a periodic surface structure (unit mesh) larger than that of the bulk termination (the fundamental structure), yielding a diffraction pattern with beams closer together than the fundamental reflections.(9,127) For example, a GaAs (100)-(m x n) surface structure is due to the (100) surface reconstruction, whose unit mesh is m x n times large than the underlying bulk structure. A schematic of the GaAs(100)-c(4x4) reconstruction is shown in Fig. 2.11. For an interesting crystal surface

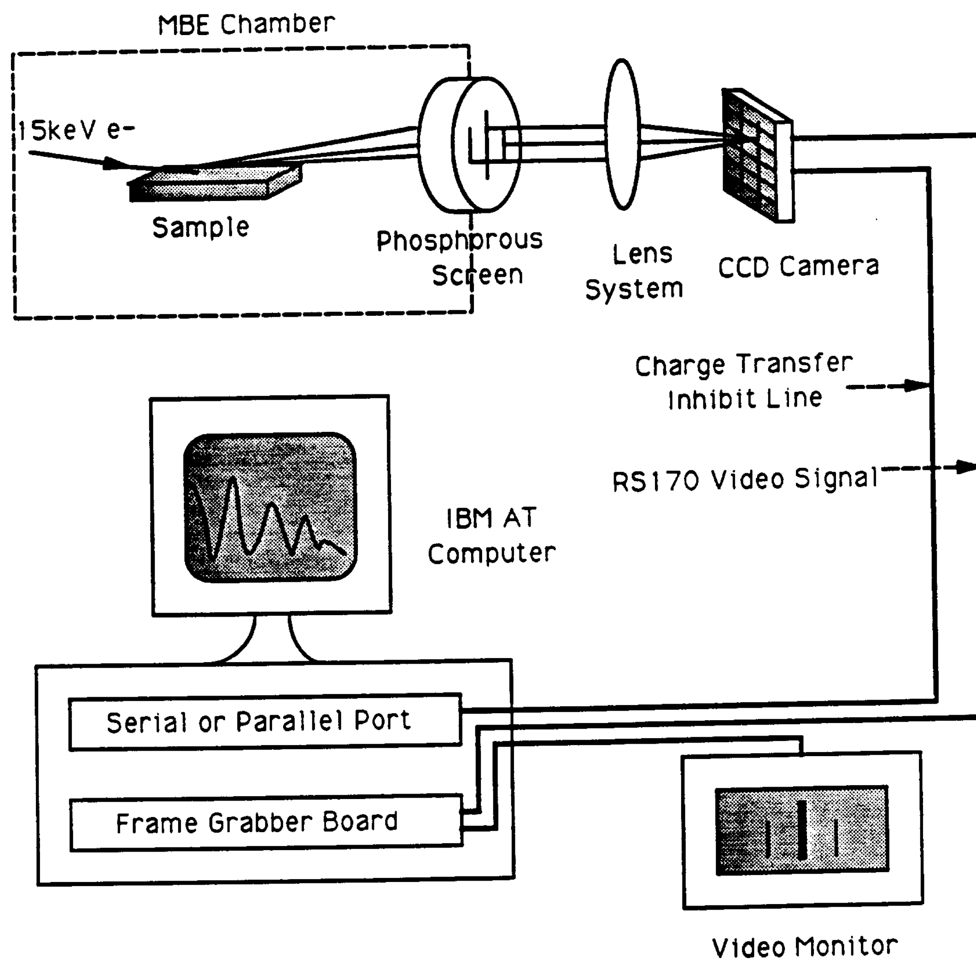

Fig. 2.12 Schematic diagram of RHEED setup in MBE system.

structure, a systematic study of RHEED patterns for its surface structure is very helpful in identifying new surface reconstructions in material growth. Such work has been mostly performed for Si and GaAs.[127]

The shape of RHEED pattern has been used for the interpretation of surface smoothness.[125,127] As stated earlier, the electron beam used in RHEED penetrates only a few monolayers into the surface. Due to the short periodicity in the perpendicular direction, the electron beam is seeing a nearly 2-D lattice, and the reciprocal lattice is an array of infinite rods perpendicular to the 2-D plane. Since the radius of the Ewald sphere is very large for a RHEED electron beam and there is a finite energy distribution in the beam, the intersection of reciprocal lattice rods by the Ewald sphere are elongated rods in the direction of perpendicular to the surface. The resulting RHEED pattern thus consists of "streaky" lines. If the surface is smooth, a streaky pattern will be observed. If the surface is not smooth, however, the electron beam penetrates more of the crystal relative to the top surface, and the electrons can "see" periodicity in the z-direction. The resulting RHEED pattern then consists of diffraction spots as the 3-D reciprocal lattice points intercept the Ewald sphere. During growth, the streaky or spotty shape of the RHEED pattern is used as a simple diagnostic of growth mode, that is, whether it is 2-D or 3-D growth.[127]

The RHEED system that was developed for *in-situ* surface characterization during MBE growth consists of an electron gun, phosphor screen, CCD camera, auxiliary video monitor, a computer equipped with a frame grabber board and software package for RHEED control and analysis. A schematic of the RHEED system is shown in Fig. 2.12. The electron beam is generated from a model VE-026 RHEED gun (Thermionics Laboratory, Inc., Hayward, CA) which can operate up to 15 keV. The RHEED gun is mounted on a bellows that allows adjustment of the electron beam incident angle through mechanical motion in addition to built-in electromagnetic deflection. The alignment of

electron beam incident on sample is first calibrated using two sets of set screws on the two deflection coils. After beam calibration and appearance of a RHEED pattern, the electron beam motion is controlled through a remote potentiometer which can move the electron beam in both x and y directions as well as focus and defocus the electron beam. An 8" OD phosphor screen is used for the display of diffraction pattern. The patterns are acquired by a low noise CCD camera that is equipped with a high quality 50 mm f/1.3 C-mount lens and an adjustable lens extension tube, which provides the image magnification/demagnification by increasing/decreasing the tube length. The image recording and analysis are performed using a 486 IBM-compatible PC and a KSA RHEED 300 system which was developed by k-Space Associates, Inc. (Ann Arbor, MI).[128] The system uses an on-chip time integration technology. Any integration time in a multiple of 1/30 second can be selected by the user for any acquisition mode. This is very useful especially in low light level applications. The (integrated) diffraction image is transferred to a standard RS-170 video signal via the CCD electronics. The image is digitized by an 8 bit A/D flash converter operating at 10 MHz. The digitizer (frame grabber) is a Data Translation DT2853 board, which digitizes the incoming signal into a 480 rows x 512 columns x 8 bit array and stores it in one of the on-board frame buffers. The DT2853 can digitize 30 images per second, i.e., at standard video rate. Concurrently, the DT2853 reconverts the digitized image to an RS-170 video signal for display on the auxiliary video monitor. The KSA RHEED 300 software extracts image from the on-board buffer on DT2853 and stores the data in extended memory, which makes the data transfer much faster than the incoming video signal being digitized. The extended memory allocated to KSA RHEED 300 is divided into 12 buffers, each of size 512 rows x 512 columns x8 bit. Thus, up to 12 images can be loaded in these buffers for display or analysis. Via the KSA RHEED 300 system, diffraction patterns can be taken

in single image mode, multiple image mode which can continuously take up to 100 images,

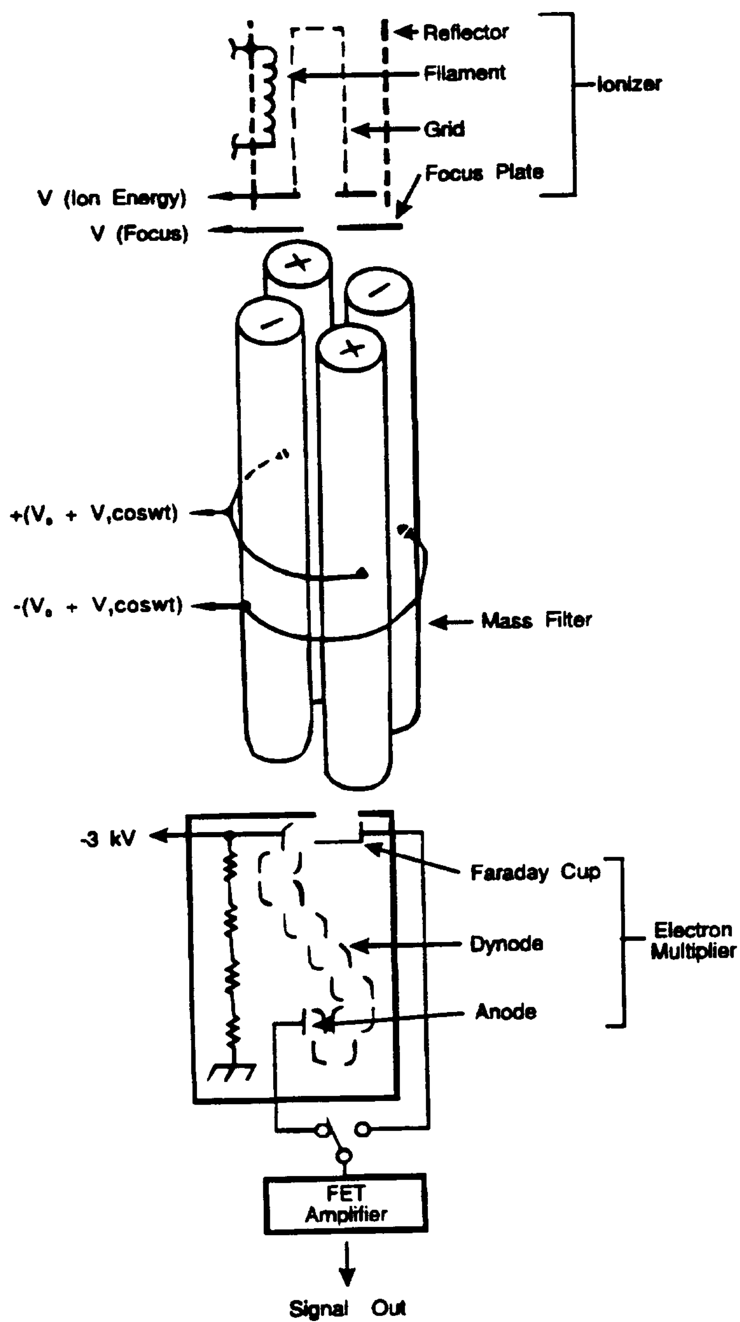

Fig. 2.13 Schematic diagram of QMS system.

linescan mode and column scan mode which record one pixel each time, dualscan mode and region mode which record the image in a specified window.

2.2.1.2 Mass Spectroscopy

A mass spectrometer is a mass analyzer which can distinguish substances by precisely measuring their charge to mass ratios in a vacuum system. The UTI 100C quadrupole mass spectrometer (QMS), which could measure mass to charge ratios from 1 to 300 amu (atomic mass units), is installed in this MBE system. With the equipped QMS in the main chamber, residual background species and those substances introduced through MBE furnaces or gas sources can be directly detected. The QMS also made leak testing of the vacuum chamber much easier.

A schematic of the QMS is shown in Fig. 2.13, and is composed of an ionizer, a quadrupole mass filter, and an ion detector unit.[129] Gas molecules within the ionizer are bombarded by electrons from dual hot tungsten filaments and become positively charged ions, which are then injected into the quadrupole mass filter section through a focus plate. The quadrupole mass filter consists of two pairs of precisely machined Mo rod electrodes where a combination of radio-frequency (RF) and electrostatic (DC) field is formed. The field between the electrodes serves as a mass filter where only substances with a certain mass to charge ratio can traverse the filter at a particular applied RF and DC voltages, other substances are filtered out. By continuously varying the applied voltages on the electrodes, a range of substances can be sequentially stabilized, and thus traverse the length of filter assembly. The mass resolution is determined by the DC/RF voltage ratio. The ions passed through the filter are detected by an "electron multiplier" which amplifies the single charge of ion into a current. The output current of the multiplier is referenced against the scan voltage and produces a spectrum of peaks. The spectrum shows ion current as a function of the mass/charge ratio in a series of peaks

corresponding to different ions. The amplitude represents the quantity of each type of ion. Discrete peaks occur because ions have discrete masses and discrete charges. The Faraday cup can also be used for collecting ions, in which ion current is not amplified and thus can be used to calibrate the multiplier gain.

2.2.2 *Ex-situ* Techniques

2.2.2.1 Photoluminescence (PL)

Photoluminescence spectroscopy is a measure of the intensity of radiation versus wavelength emitted from a semiconductor as a result of radiative recombination of electron-hole pairs that have been optically excited.[130] In order to cause this excitation, the incoming photon energy must equal or exceed the energy difference between the initial and final states of the electron. Such an excited electron usually returns to its initial state after a short time. If the excited electron returns to its initial state by radiative means, the process emits a photon whose energy is the difference between the excited and the initial state energies. The spectral distribution of the emitted photons shows an emission peak at the energy (or wavelength) corresponding to each excited level. The excited electron can radiatively recombine with a hole through various kinds of recombination processes as shown schematically in Fig. 2.14. The simplest recombination process is a band-to-band recombination where a free electron excited in the conduction band recombines radiatively with a free hole excited in the valence band. Impurities which introduce traps, donor or acceptor levels in the band gap provide alternate paths for de-excitation. When an electron or hole is captured by an impurity center and then the trapped carrier recombines radiatively with the remaining carriers in the bands, this is called band-to-impurity (free electron to acceptor (e,A^0) or donor to free hole (D^0,h)) recombination. When both the excited electron and hole are captured by different impurity centers and then the trapped electron and hole recombine radiatively,

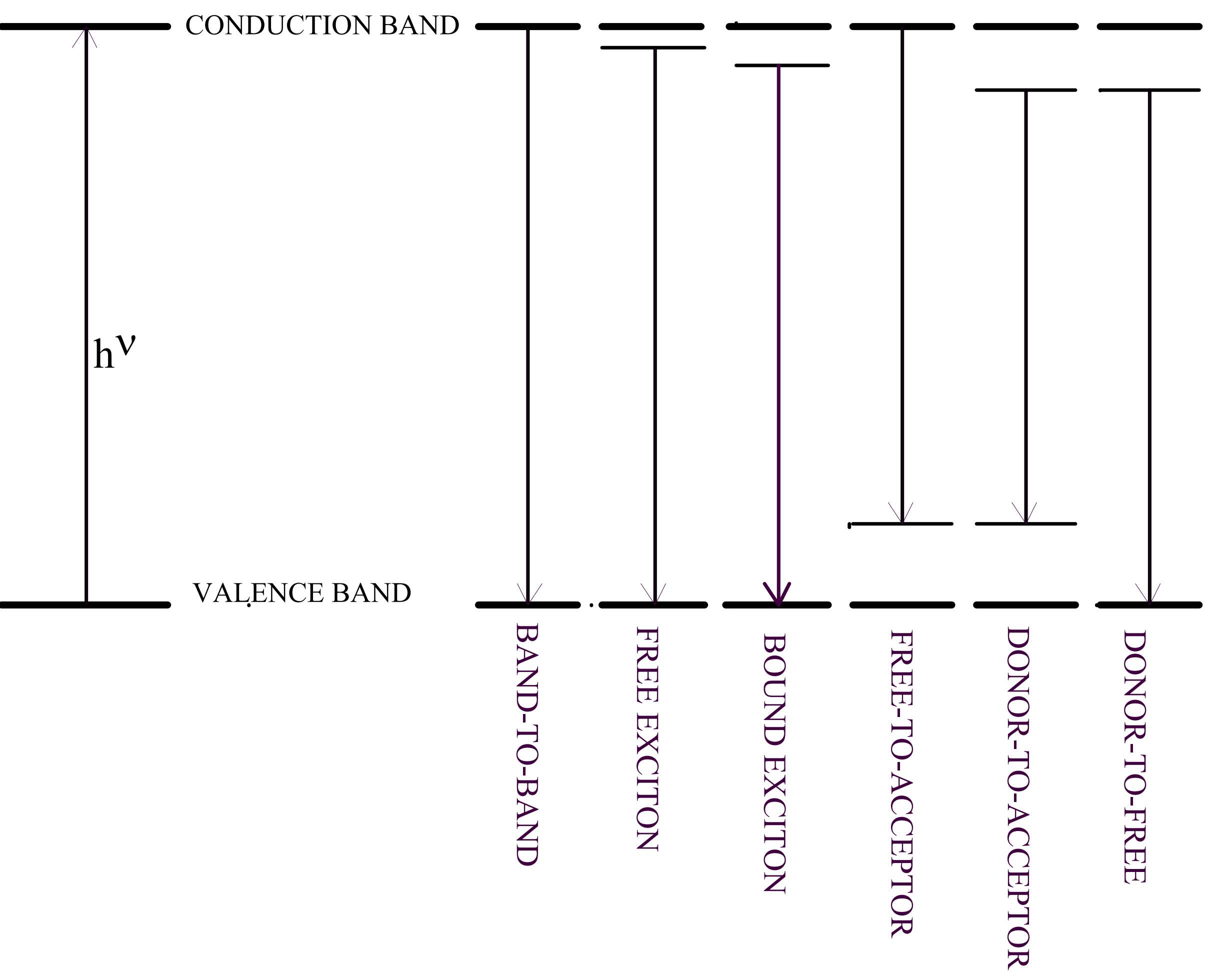

Fig. 2.14 Schematic of Possible PL Recombination Processes

Table 2.4 Typical PL Signals Observed in ZnSe

Energy	assigned transition	reference
2.815	F^1X	78
2.801-2.804 (may split)	F^0X	80, 162
2.798(may split)	D^1X	151
2.796	D^0X	151,160
2.793 (may split)	A^0X-N	162
2.791	A^0X-Li,N	80,151, 160,161
2.786	I_1	87
2.780-2.782	I_1^D (?$V_{Zn}X$, $A_{Cu}X$)	59,77
2.774	I_v	11,151
2.717	A peak((e,A^0), (D^0,h)?)	87
2.710	(e,A^0)	84,151,162
2.696±5	DAP^s	59,84,151,162
2.677±5	DAP^d	59,84,151
2.635	$D^?AP$	161
2.603	Y_0	160
2.5206	S_0	11
2.2	Cu_{Zn}-Cu_{In}	161
2.15	H-dp?	151
1.9	Cu_{Zn}	161

Table 2.5 Binding Energies for Acceptors in ZnSe Grown by MBE (Data taken from Ref. 132)

Acceptor	E_A (meV)
"S"	~ 56
O	83 ± 3
P	88.4 ± 0.5
"A_2"	95.0 ± 0.4
"A_1"	106.1 ± 0.6
N	111.3 ± 0.5
Li	114.2 ± 0.3
As	114.3 ± 0.5
Na	~ 124 - 128
Ag	~ 431
Au	~ 550

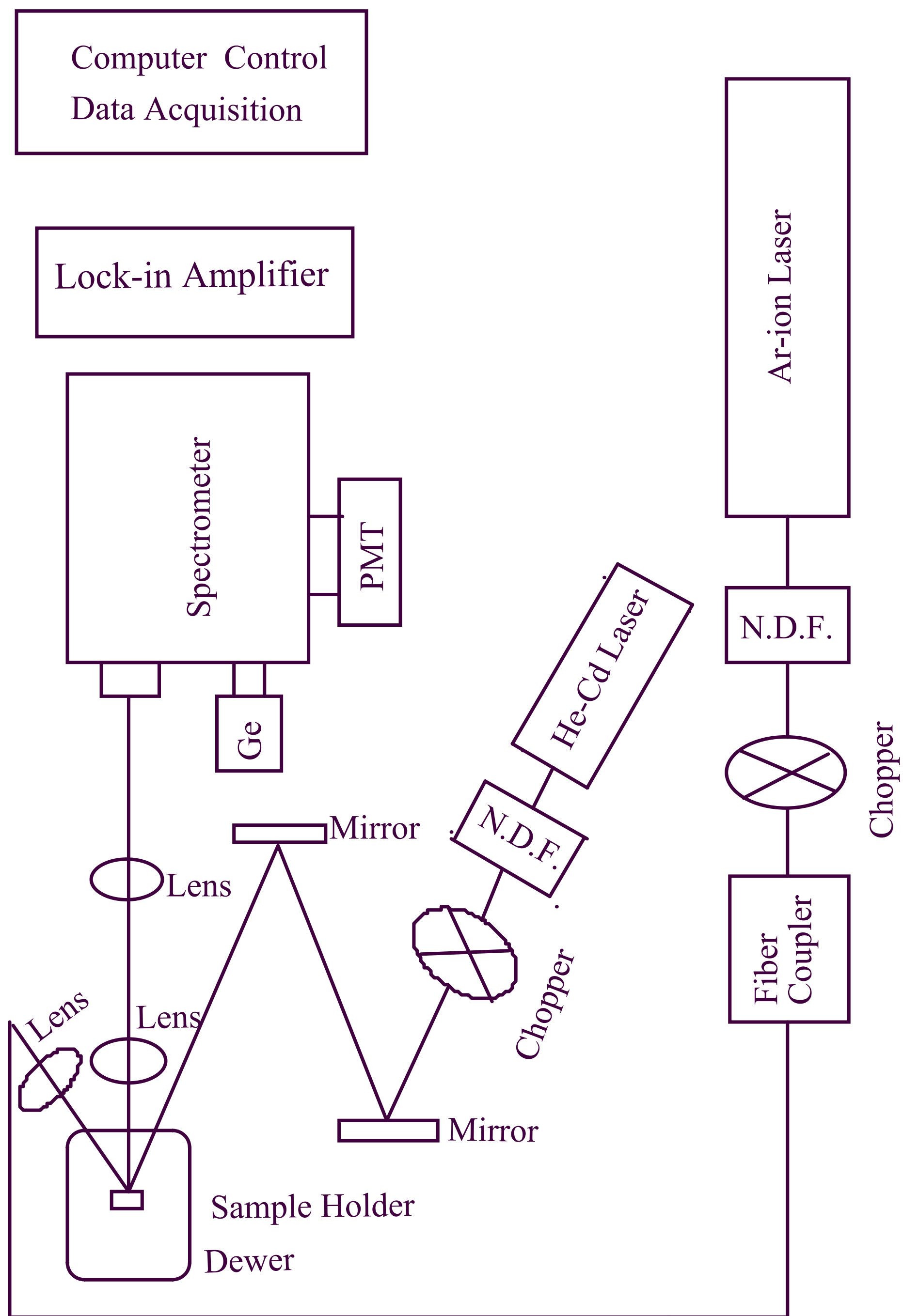

Fig. 2.15 Schematic of Photoluminescence Measurement Setup

this is known as donor-acceptor pair recombination. A generated electron-hole pair becomes an exciton. An exciton is a complex with an electron and hole bound together by a Coulomb attraction which can move freely as a quasiparticle in semiconductor. These free excitons decay in the ground state through free-exciton (F^0,X) recombination accompanied by luminescence. When free excitons are bound to impurity centers, these bound excitons (donor bound exciton (D^0,X) or acceptor bound exciton (A^0,X)) decay at just below the (F^0,X) energy.

PL is a powerful technique for mapping energy levels in band gap; therefore, it is very useful in the analysis of impurities and defects in semiconductors. The application of PL to the study of ZnSe has been substantial and shows the importance of impurities, opposed to native defects, in controlling the conductivity, and in demonstrating the desirable characteristics of the nitrogen acceptor level in relation to other available dopants.[(131)] The emission peaks in a PL spectrum are signatures of the impurity and defect states present in the material. However, care must be taken in assigning these peaks to specific transitions because some defect states may overlap in energies. To accurately identify the transitions, selective photoluminescence (SPL) and photoluminescence excitation (PLE) techniques, which use a tunable laser source to focus on the interesting emission line, are often employed to isolate a certain transition from other overlapping luminescent bands. Energy levels typically of interest in ZnSe are listed in Table 2.4. One of the important properties for dopants in semiconductor is the binding energy, which can also be determined by PL measurements. Table 2.5 lists the binding energies for acceptor dopants in ZnSe grown by MBE. Donor dopant levels in nitrogen-doped ZnSe are typically about 30 meV below the conduction band (CB) for a native shallow donor, and at about 55 meV below CB for a nitrogen related deep donor.[(87)] The PL spectrum is often featured by phonon replicas which come with the main recombination peak displaced by energies of the relevant phonon. The phonon

replica is a signature of electron-lattice interaction during the recombination process. In compound semiconductors, the electron-phonon interaction is dominated by the longitudinal optical (LO) mode phonons, and for strong phonon coupling, multiple phonon replicas can be observed. In ZnSe, the LO phonon energy is about 32 meV.[95] Room temperature PL is generally weak and broad due to non-radiative recombinations, the emission peaks are mainly from band-to-band, (F,X), (D^0,h), or (e,A^0) transitions.

The PL measurements discussed in this study were conducted in the laboratory of Professor Nancy Giles by Christina Petcu and Monica Moldovan at the Physics Department of West Virginia University. A schematic of one of the PL setups is shown in Fig. 2.15, and identifies the major components for this type of measurement. A 325-nm line from a He-Cd laser is used for above band gap excitation of ZnSe. An Ar ion laser is used to provide below bandgap excitation. The excitation power on the sample surface is about 240 mW/cm^2 for low-temperature PL measurements. The samples are contained in a Janis Research Products SuperVarietemp Optical dewar which can provide a temperature control from below 2 K up to 300 K. Low-temperature PL is typically measured at about 5 K. A standard photomultiplier tube (PMT) with GaAs cathode which has a cutoff wavelength of 880 nm is employed for the light detection. Room-temperature PL measurements were performed using a different monochrometer and a photon counting system for light collection. A microscope-based system is used for incident light focusing and collection, leading to much higher power densities. Spectra were corrected for system response if not mentioned.

2.2.2.2 Fourier Transform Infrared (FTIR) Spectroscopy

Infrared (IR) spectroscopy is used primarily to determine transition energies between vibrational energy levels in molecules and solids.[130] In an IR absorption process, a photon of infrared radiation is completely absorbed and the molecule or solid

is promoted to a higher vibrational energy state. For this absorption to occur, the energy of the photon must match the energy separation of vibrational states in the molecule or solid. The vibrational state energies of a molecule are quantizied,

$$E_v = (n + \tfrac{1}{2})\hbar\omega \qquad n = 0, 1, 2\cdots \qquad (2.4)$$

where $\omega = (k/m)^{1/2}$, k and m are the force constant and mass of a harmonic oscillator for the corresponding molecule, respectively. The energy separation of any two neighboring levels is

$$\Delta E = \hbar\omega \qquad (2.5)$$

The vibrational transition energy is normally expressed in terms of wavenumber ν. Using $\Delta E = hc\nu$, ν can be expressed as

$$\nu = \omega / 2\pi c \qquad (2.6)$$

Typical values of ν lie in the range from 200 cm^{-1} to 3500 cm^{-1} and the corresponding transitions lie in the infrared region of the electromagnetic spectrum. The transition energies are generally different for different molecules or bonds, and are determined by the structure of the molecule or the bond. Therefore, the observed ν values are signatures of particular molecules or bonds, and hence provide the evidence of their presence. Semiconductor impurities can absorb infrared energy by photoionization of their bound carriers, or may modify their immediate lattice environment to produce a so-called local vibrational mode (LVM). The measurement of local vibrational modes thus gives information about the defects in the materials investigated.

Fourier transform infrared spectrometers are widely used on account of their high sensitivity and their digital data handling capability.[130] The FTIR spectrometer used in this study is a Nicolet model 550 located in Prof. Larry Halliburton's laboratory. A mercury-cadmium-telluride detector is used for the low intensity light detection. For extended range, a DTGS detector is used. To avoid the effect of water vapor absorption on the desired spectrum, the spectrometer is purged using nitrogen gas. Samples are normally cooled to low temperatures (~15K) through a closed-cycle helium refrigerator to remove the effects of lattice vibrations or phonons in the absorption spectra. To minimize the effects from the substrate, a bare substrate scan is taken and subtracted from the sample scan.

2.2.2.3 Secondary Ion Mass Spectrometry (SIMS)

Secondary ion mass spectrometry (SIMS) is the mass analysis of secondary ions generated by ion sputtering. Bombarding the surface of a solid with an energetic ion beam generates a variety of secondary transitions, including the emission of electrons, photons and ions. Detection of any of these secondary events could serve as the basis of an analytical probe. However, SIMS is optimized for the detection of positive and negative secondary ions. SIMS is effectively used in the analysis of a broad range of materials for depth profiling and surface studies.

SIMS measurements in this study were performed at Charles Evans & Associates (Redwood City, CA) using an upgraded CAMECA IMS-4f double-focusing, magnetic sector microanalyzer(s). Typical instrument conditions for SIMS measurement of ZnSe are listed in Table 2.6.

Table 2.6 SIMS Measurement Conditions Used for ZnSe

Primary ion beam	Cs^+ (Dynamic SIMS)
Primary Beam Energy	14.5 keV
Beam Current	0.03 μA
Raster Size	125 μm^2
Detected Area	30 microns
Secondary Ion Polarity	negative
Charge Neutralization	Au-coat, e-gun

2.2.2.4 Optical Microscopy

In applications where the dimensions of interest are below the optical diffraction limit (~0.8 μm), electron microscopy is used by necessity. However, traditional optical methods remain useful for many applications such as examining topological features large than ~1.0 μm, examining defects, or counting etch pits.[130] Normaski microscopy is one of these useful optical microscopy techniques. In this technique, two microscopic images of a surface are formed so that they are slightly displaced in space and of opposite phase. Interference bands appear where the images overlap. The physical displacement and the interference bands heighten the visibility of small variations in surface levels. If using a UV light source for the illumination, the above bandgap energy light will excite electrons to the conduction band and other high energy levels in the band gap. The intensity of the resulting luminescence due to recombination of electron-hole pairs directly reflects the surface structure of the illuminated area. Thus, a fluorescent image

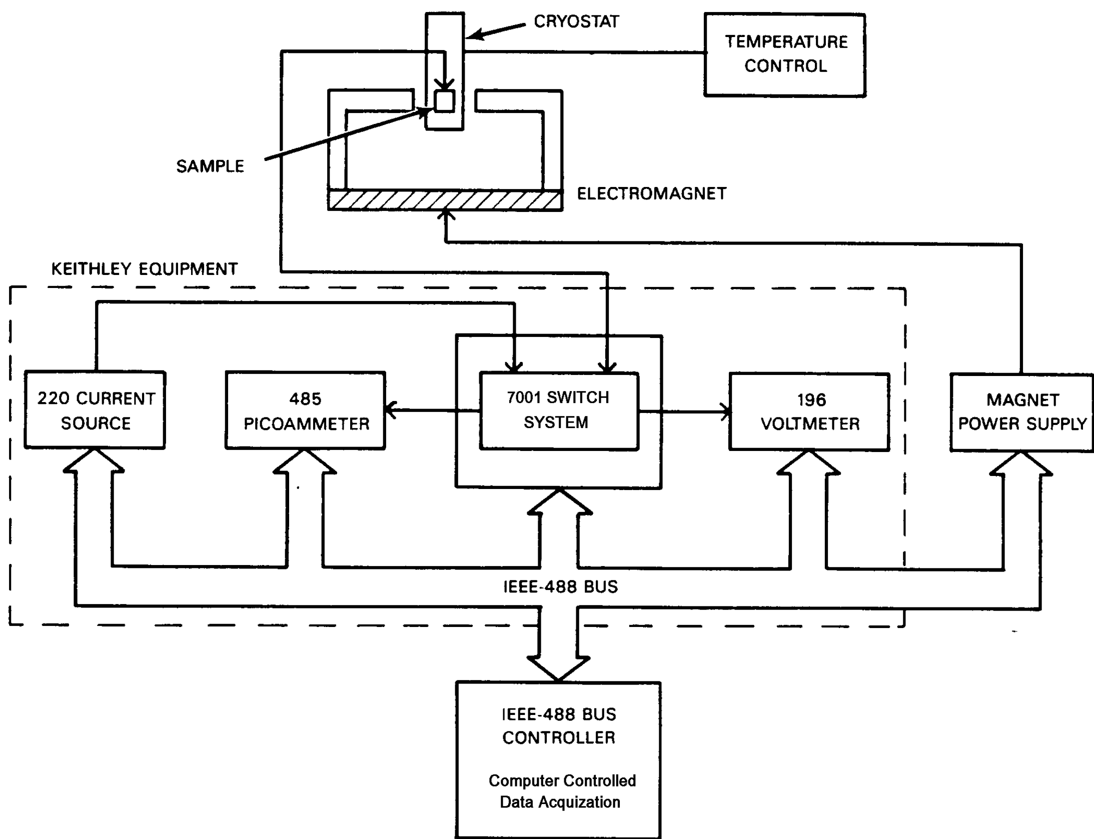

Fig. 2.16 Schematic of a Hall measurement setup.

can be obtained.

An Olympus BMP-60 optical microscope was used to perform the Normaski microscopy examination of samples for surface features. A 100 W Hg lamp was adopted as the UV light source for fluorescent microscopy.

2.2.2.5 Other Techniques

Hall effect is used for measuring carrier concentration and resistivity[133] of thin films grown by MBE. A typical van der Pauw configuration is adopted due to irregular shape of samples. The measurement is restricted to room temperature with the current setup. For undoped ZnSe samples, indium (In) is used for the contact metal. For nitrogen-doped ZnSe, due to the Schottky contact of In, a highly-doped ZnTe:N thin layer is deposited on ZnSe:N film and etched off except in the regions for making Hall measurement contacts. An ohmic contact for p-type ZnSe is obtained from this structure.

A schematic of Hall measurement setup is shown in Fig. 2.16. A Keithley 220 current source applies the current to the sample under test. The current through and voltage across the testing sample are measured by a Keithley 485 picoammeter and 197 voltmeter, respectively. A Keithley 7001 switch system provides the applied voltage and current as well as polarity control. A 6000 Gauss magnetic field is typically used. The instruments are connected through an IEEE-488 bus and controlled by the computer.

Atomic force microscopy (AFM) uses force to image a surface.[134] By slightly pushing a extremely sharp tip against atoms on the surface, the tip deflection is actually a reflection of the surface atomic arrangement. Sensing the small size displacement of the tip will give the atomic-scale topography of a sample. Because the AFM does not depend on a current, it can look at nonconductors as easily as conductors. With the AFM in a contact mode, atomic resolution as high as 1 to 2 angstroms can be achieved. In

addition to observing structure on atomically smooth surface, AFM can also image surfaces with adsorbed organic molecules, such as sorbed acid, DNA and proteins.

A Digital Instrument Nanoscope II AFM was used to examine ZnSe film surface morphology and defect states, which gives supportive information to other techniques such optical microscopy and PL.

EPR spectroscopy is widely used in characterizing complexes and point defects which have unpaired electrons.(157) In this study, EPR is used to probe the Se vacancies in ZnSe. The experiments were performed in the laboratory of Professor Larry Halliburton at Physics Department of West Virginia University by Scott Setzler. The EPR data are taken with a Bruker Model ESP 300 spectrometer operating at 9.5 GHz with 100-kHz static field modulation and at 9 K. (Data shown in this dissertation is with the magnetic field parallel to the [100] orientation of the sample.)

2.3 Typical Growth Sequence

To perform a thin film growth by MBE, a specific sequence of substrate preparation, growth preparation, film growth, and growth termination is followed. In the case of ZnSe grown in this study, the procedures are described below:

Substrate preparation

Semi-insulating (100) GaAs is used as substrate for ZnSe growth. Specifications of GaAs substrate are listed in Table 2.7. The as-shipped GaAs consists of 2" wafers which were cut into pieces 1 cm x 1 cm to fit the substrate block used in this MBE system. One 1 cm x 1 cm substrate is used for each growth run. Before it is loaded into a vacuum system, the substrate is degreased and chemically etched to remove the surface contaminants under a chemical hood. This procedure is listed in Table 2.8. The

chemically etched substrate is then mounted on the substrate block using Aquadag (Ladd Research Industries, Inc.), which has very low vapor pressure, good thermal conductivity, and is suitable for low temperature growth. The substrate block is loaded into the load lock chamber and transferred into main chamber after the load lock pressure is below $5x10^{-7}$ Torr.

Growth preparation

The etched substrate is covered by oxides. To remove the oxides prior to epitaxial layer deposition, the substrate is normally heated up to about 600 °C. In this study, two oxide desorption procedures are used: (1) heating the substrate to 580 °C and maintaining for 20 min, as the so-called conventional thermal cleaning; and (2) heating the substrate to 400 °C and maintaining for 20 min under an atomic hydrogen flux, as the so-called atomic hydrogen cleaning. The substrate surface reconstruction is monitored by RHEED, which normally has a weak and spotty pattern before oxide desorption, and a bright and streaky pattern after the oxide desorption. After finishing the oxide desorption procedure, the substrate is cooled to the temperature for ZnSe growth, which was either 250 °C or 300 °C.

To start the growth, a stabilized source flux must be obtained. A typical procedure for this process is: (1) determining the beam equivalent pressure (BEP) and the corresponding oven temperature for each source flux used for the growth; (2) heating the oven to a temperature within 100 °C of the temperature for the required growth flux after the substrate block is transferred into the main chamber; (3) heating the oven to the temperature for growth flux at least one half hour before starting the growth; (4) checking BEP for each source at least 20 min after the oven reaches the temperature for growth flux; (5) adjusting oven temperature for the required BEP as necessary and allowing at least 10 min for the oven to stabilize.

Film growth

As soon as the substrate reaches the growth temperature and the source flux stabilizes at the required BEP, film growth commences. After making sure that all oven shutters (Zn, Se ovens and overall) are open and the BFM is retracted, ZnSe growth can be started by opening the substrate shutter. For nitrogen-doped growth, the growth is interrupted by inserting the substrate shutter to prepare for the nitrogen plasma source. If the hydrogen source is to be used, it will be turned on to the required operating condition at this time. After the plasma is stabilized at the required power and nitrogen flow, growth is resumed by opening the substrate shutter.

The growth can be monitored through RHEED. The RHEED pattern and its change can give information on surface reconstruction and flatness, growth mode, and crystallinity of the growing film.

Growth termination

Growth is terminated by closing the substrate shutter. The substrate is then cooled down to room temperature. The nitrogen and hydrogen sources are turned off if they were used. Source fluxes are checked before the source ovens are turned down to the maintaining temperatures.

Table 2.7 Specifications of GaAs Substrate Used for ZnSe Growth

Conduction Type	Semi-insulating
Dopant	None
Resistivity	(5 - 7) x 10^7 ohm cm
Mobility	6900 - 7100 cm^2 V^{-1} s
Etch Pit Density	≤ 5000 cm^{-2}
Orientation	(100) 2° ± 0.1° toward (110)
Thickness	400 ± 25 μm
Surface Finish	Side 1 Polished, Side 2 Etched

Table 2.8 GaAs Substrate Etching Procedure for ZnSe Growth

(1) degrease as follows:

boil in Trichloroethane (TCA) for 5 min, twice, with fresh solvent each time;

boil in acetone for 2min, once;

boil in methanol for 5min, twice, with fresh solvent each time;

(2) rinse under running de-ionized water (18 MΩ) for 5 min and then blow dry with nitrogen gas;

(3) prepare a solution of H_2SO_4 : H_2O_2 : H_2O = 8 : 1 : 1;

(4) etch substrate in solution prepared in (3) for 5 min at room temperature;

(5) rinse under running de-ionized water for 5 min, and again blow dry with nitrogen gas.

CHAPTER III

REDUCTION OF TWIN-RELATED DEFECTS

3.1 Substrate Cleaning Using Atomic Hydrogen

The development of ZnSe light emitting devices is hindered by their very short device lifetime which limits the application of ZnSe-based devices only to research laboratories. This issue may result in other material systems such as GaN dominating the photonics and optoelectronics market.(8) One of the major contributors to the short device lifetime is the high defect densities in the active regions of ZnSe device structures.(105,107) The primary defect is a twin-related stacking fault which most likely occurs at the III-V/II-VI substrate/epilayer interface. This defect acts as a generation site of threading dislocations.(113,114) The threading dislocations penetrate into the active region and become nucleation sites for dislocation networks in the active layer as the device degrades during operation.(107) The dislocation patches can be observed by CL and TEM.(105,109) To reduce the formation of those dislocation networks, one first needs to reduce their nucleation sites which originate from stacking faults at the interface between ZnSe and GaAs.

It is believed that the stacking faults are formed at the interface during the initial layer growth.(56) The stacking faults are due either to incomplete oxide removal or poor surface preparation that introduces the formation of stoichiometry related defects. For MBE growth of ZnSe on GaAs substrates, the final step prior to growth is often a thermal cleaning at temperatures ranging from 580 to 650 °C to remove the native oxides.(52) However, the resulting GaAs surface after this treatment exhibits a Ga-rich surface reconstruction. This gallium-rich surface can lead to the formation of Ga_2Se_3 at the interface(63) which can then serve as nucleation sites for stacking faults. Substantial efforts have been made in reducing the density of stacking faults over the past few

years.[56,57,61-63,140] Either heating the substrate under an As-flux or the growth of a GaAs epilayer prior to ZnSe growth has shown to improve the interface quality.[141] Recent studies show that stacking fault densities less than 10^4 cm^{-2} can be obtained through a combination of As-rich surface GaAs epilayer growth followed by Zn treatment of the surface prior to ZnSe growth.[56,141] A disadvantage of this approach is that a separate growth chamber is required for the GaAs epilayer deposition to minimize the potential for cross-contamination.

Atomic hydrogen has been demonstrated to be effective in removing surface contaminants for many types of substrates prior to epitaxial growth.[27-32,135-138] Both thermally cracked[27-32] and remote plasma sources[135-137] are used to generate atomic hydrogen. Surfaces after atomic hydrogen cleaning contain very low levels of oxygen and carbon contaminants as indicated by Auger electron spectroscopy (AES) for Si,[30,139] GaAs,[27,136] CdTe[138] and InP[32] substrates. GaAs epilayers grown on Si substrates cleaned with atomic hydrogen show significant reduction of dislocation density, to about 10^4 cm^{-2}.[30,31] Thus the use of atomic hydrogen to clean GaAs for the subsequent growth of ZnSe was under taken.

In additional to a clean surface, the surface reconstruction of GaAs is found to be As-rich after atomic hydrogen cleaning as indicated by RHEED.[27,136] This implies that atomic hydrogen treatment can result in a similar GaAs surface to the GaAs buffer layer approach. Both undoped and nitrogen-doped ZnSe thin films were grown on GaAs substrates which were cleaned with either the conventional thermal treatment or atomic hydrogen treatment prior to ZnSe growth. The defect structure in the films was examined by various microscopy techniques and by PL measurements. In this chapter, experimental procedures are described first, followed by the results of the characterization of the ZnSe samples. Finally, a discussion of micro-defect related issues is presented.

3.2 Experimental Procedures

ZnSe thin films were grown on GaAs substrates by MBE. The GaAs wafers used were (100) oriented with 2° toward (110) with other properties listed in Table 2.7. The substrate was solvent degreased and chemical etched as more completely described in Table 2.8 before being loaded into the vacuum chamber. Oxide removal for etched GaAs substrate was carried out in the growth chamber by one of the two procedures described next: conventional thermal cleaning by heating the substrate to 580 °C and maintaining for 20 min after the temperature has stabilized or atomic hydrogen cleaning by heating the substrate to 400 °C and maintaining for 20 min under an atomic hydrogen flux after the temperature has stabilized. The atomic hydrogen flux was generated using the commercial tungsten filament thermal cracker described in Ch. II running at 9.5 A in a current regulation power mode. High purity (5N) hydrogen gas flows through the hot filament to maintain a system pressure in the range 2 to 6×10^{-6} Torr. These operating conditions correspond to an operating power about 420 W and a molecular cracking efficiency of about 5%.

During the cleaning process, the substrate surface is monitored by RHEED for surface reconstruction and smoothness. Undoped and nitrogen-doped ZnSe have been grown on GaAs substrates using both cleaning procedures for comparison. Growth temperature was either 250 °C or 300 °C, while the II/VI ratio ranged from 2 to 0.5. Nitrogen doping was achieved using an atomic/radical rf plasma source. After the growth, samples were examined by Nomarski microscopy for surface roughness, and by fluorescent microscopy to image the micro-defects. Selected samples were also looked at using AFM for microstructure. Photoluminescence measurements at low-temperature (~5 K) were performed on all samples using the 325 nm line from a He-Cd laser (focused to a power density of 240 mW/cm^2) in conjunction with a grating spectrometer and standard detection electronics. The spectra are corrected for system response.

3.3 Results

3.3.1 RHEED

The substrate surface is monitored by RHEED during the cleaning process. Surface reconstruction and flatness are reflected by RHEED pattern. Fig. 3.1(a) is a typical RHEED pattern of (100) GaAs substrate without any treatment, i.e., the as etched surface. The oxide-covered surface is easily seen from the ring and weak spotty pattern. After conventional thermal cleaning, the surface oxides are removed as indicated by the bright RHEED pattern in both [100] and [110] azimuth as shown in Fig. 3.1(b). The elongated pattern indicates a smoother surface after the thermal cleaning. However, the diffraction pattern is not very strong and remains spotty. This could be a sign of an incomplete oxide removal of the surface. In contrast, Fig. 3.1(c) shows the pattern from a GaAs surface cleaned with atomic hydrogen. The strong and streaky shaped pattern indicates that a smooth 2-D surface is obtained with the atomic hydrogen cleaning procedure.

3.3.2 UV Fluorescent Microscopy of ZnSe

Two types of stacking fault defects are observed in ZnSe films grown on GaAs substrates and are typically studied using transmission electron microscope (TEM).(56,135) Frank-type stacking faults, which are bound by Frank partial dislocations, appear as triangular-shaped twin faults, while Shockley-type stacking faults, which are bound by Shockley partial dislocations, appear more line-shaped. The radiative efficiency is lower in the region of the stacking fault, allowing the use of techniques such as cathodoluminescence to image the defects.(56) When looking at ZnSe samples under an optical microscope using a Hg lamp, the UV illumination excites electrons from the valence band into the conduction band, resulting in blue light luminescence from the ZnSe film. Fig. 3.2 shows the micrographs under a fluorescent microscope from ZnSe

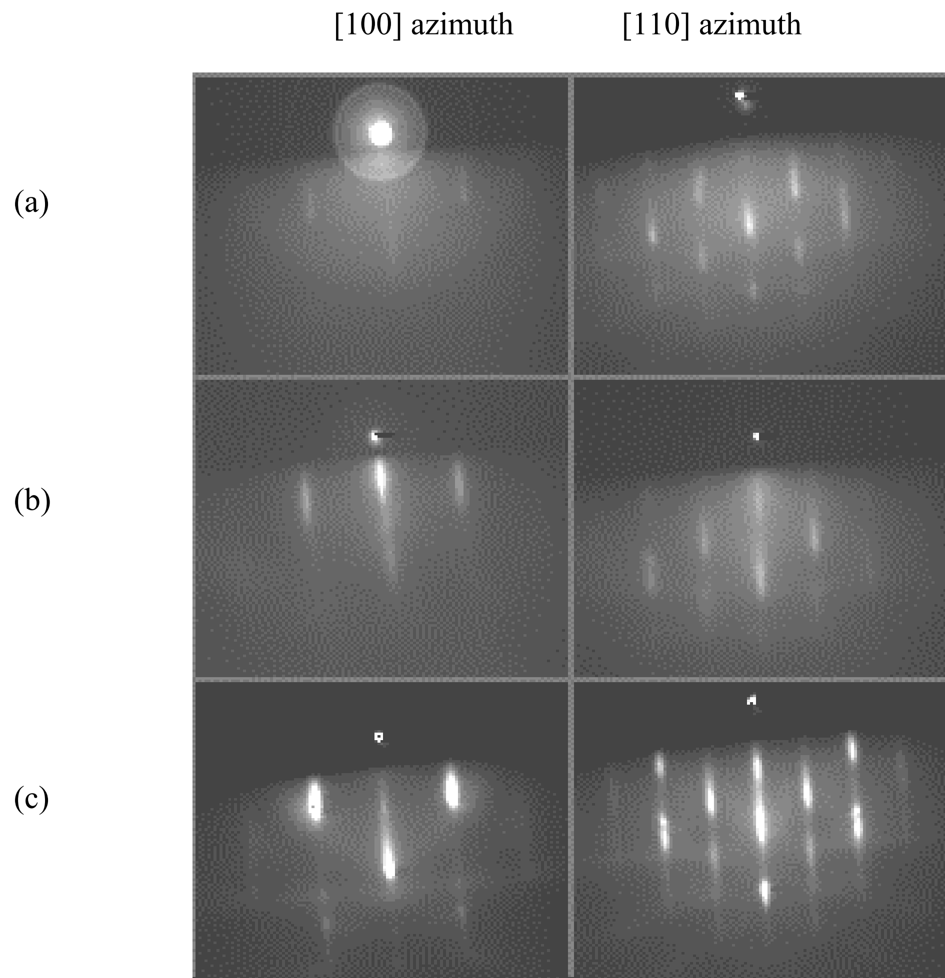

Fig. 3.1 RHEED pattern of (100) GaAs substrate in both [100] and [110] azimuth: (a) as-etched surface; (b) after conventional thermal cleaning; (c) after atomic hydrogen cleaning.

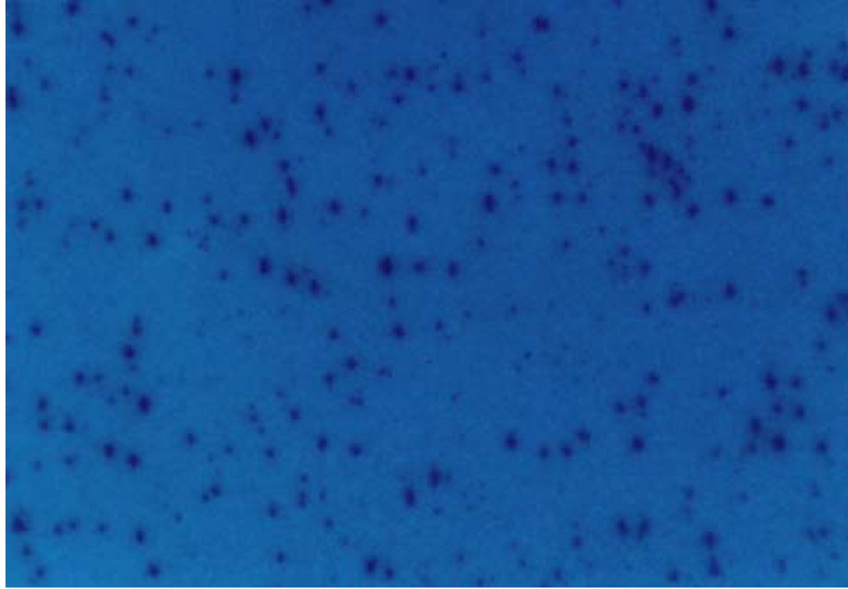

(a)

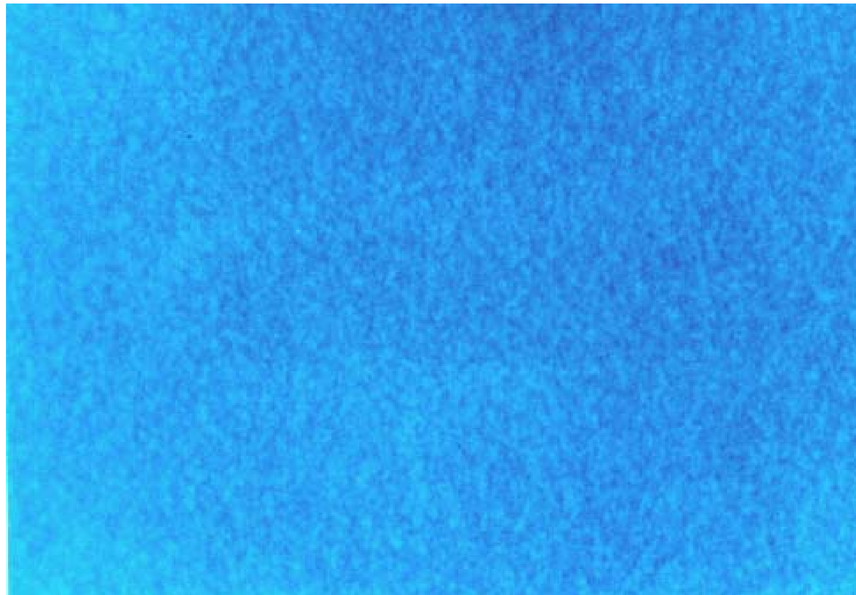

(b)

Fig. 3.2 Optical fluorescence micrograph of undoped ZnSe/GaAs grown (a) with conventional thermal cleaning, (b) with atomic hydrogen cleaning. The micrographs represent an area of 125 μm by 88 μm.

films grown on GaAs substrates. Fig. 3.2(a) is the fluorescence micrograph of an undoped ZnSe film grown on GaAs substrate with conventional thermal cleaning. The dark features are non-radiative regions due to stacking faults, with the short line-shaped features ascribed to Shockley-type stacking faults and the larger triangular-shaped features to Frank-type stacking faults. These images are very similar to those observed under TEM.[56] The density of both types of defects was determined to be greater than 10^7 cm^{-2} by simply counting the number of stacking faults in the field of view. Fig. 3.2(b) shows a typical fluorescence micrograph of an undoped ZnSe grown on GaAs substrate cleaned with atomic hydrogen. A significant reduction in defect density is observed. The dark features associated with the stacking faults were isolated and difficult to find on these layers. The density of both types of stacking faults was conservatively estimated to be less than 10^4 cm^{-2} by direct observation. We did not observe a significant difference for the two different substrate temperatures (250 °C and 300 °C) or any of the growth flux ratios investigated.

Heavy nitrogen doping ($>10^{18}$ cm^{-3}) has been reported to enhance the formation of stacking faults.[114] In this study, ZnSe with nitrogen-incorporation levels greater than 10^{19} cm^{-3} (as determined by SIMS) were grown on substrates cleaned by both techniques. Fig. 3.3(a) is a fluorescence micrograph of such a sample grown with the conventional thermal cleaning. Both Frank- and Shockley-type stacking faults were again observed at densities of about 10^8 cm^{-2}. In contrast, the micrograph displayed in Fig. 3.3(b) indicates much cleaner material with a defect density of about 10^4 cm^{-2} for a heavily nitrogen-doped sample cleaned with atomic hydrogen prior to growth.

AFM images of the ZnSe surfaces indicate that films grown with atomic hydrogen cleaning also have a smoother surface than those grown with conventional thermal cleaning. The features on both types of samples were too small to be observed by Nomarski microscopy. Hence the samples appeared mirror-like and were

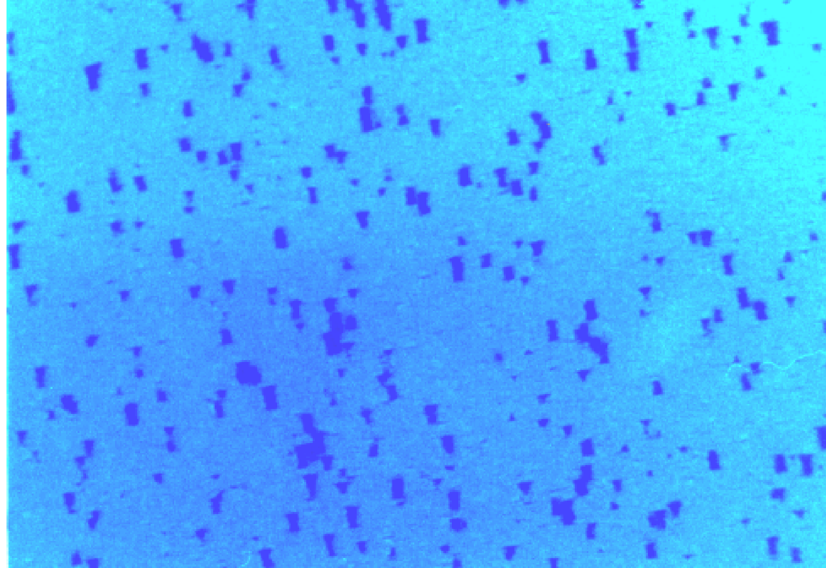

(a)

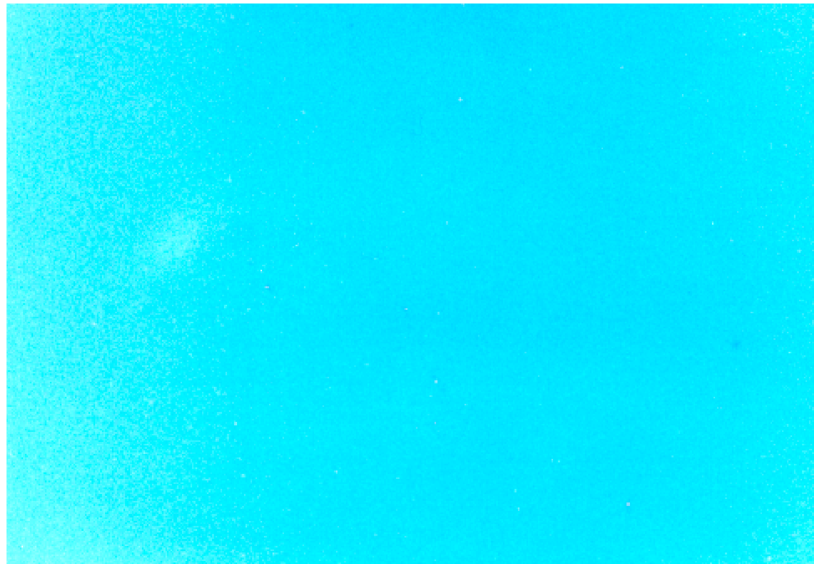

(b)

Fig. 3.3 Optical fluorescence micrograph of nitrogen doped ZnSe/GaAs grown (a) with conventional thermal cleaning, (b) with atomic hydrogen cleaning. The micrographs represent an area of 125 μm by 88 μm.

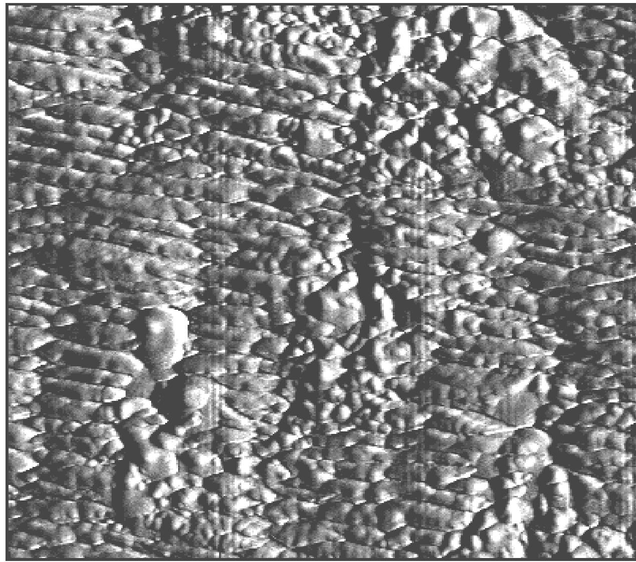

(a)

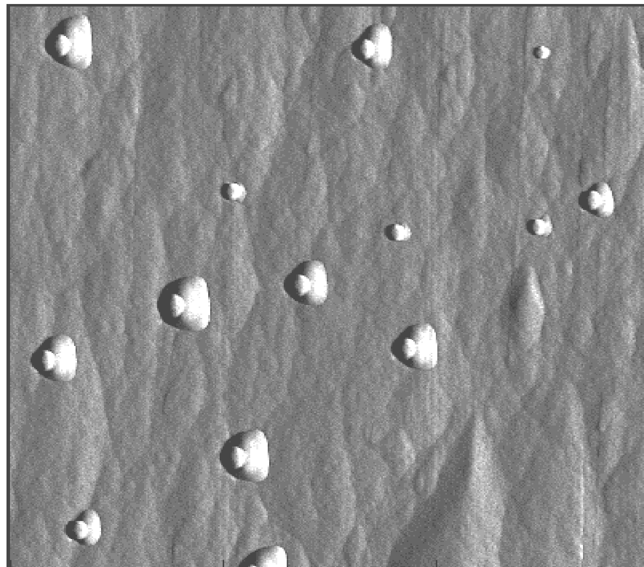

(b)

Fig. 3.4 Atomic force images of ZnSe/GaAs grown (a) with conventional thermal cleaning, (b) with atomic hydrogen cleaning. The micrographs represent an area of 3 μm by 3 μm.

indistinguishable for light microscopy. However, they showed very different microstructures under atomic force microscopy. Fig. 3.4(a) is an AFM image of a nitrogen-doped ZnSe grown with conventional thermal cleaning. The surface was rough and appears to have step-like features. The roughness was about 4 nm between features. In contrast, Fig. 3.4(b) is an AFM image of a nitrogen-doped ZnSe grown with atomic hydrogen cleaning. The surface was very smooth, with no observation of the large hillock features. However, small features were observed, whose origin is unknown. The roughness is about 2nm between features. These results indicate that ZnSe films grown on GaAs substrates using atomic hydrogen cleaning have much smoother surface morphology than that using conventional thermal cleaning.

The microstructural features observed under AFM and surface structures from RHEED pattern are consistent for GaAs substrates cleaned with the conventional thermal treatment and atomic hydrogen treatment. Most importantly, ZnSe films grown on GaAs substrates cleaned with atomic hydrogen show a dramatic reduction of stacking faults. The cleaner surface left by atomic hydrogen treatment significantly reduces the formation of micro-defects.

3.3.3 Photoluminescence

Low-temperature PL spectra also show a dramatic difference between samples cleaned with atomic hydrogen and those grown after the conventional thermal treatment. The quality of ZnSe films can be evaluated by their PL spectra. PL of high-quality undoped layers will be dominated by excitonic features while defect-related features will dominate the PL spectra in layers with high defect densities.(142) The Y_0 line at 2.60 eV line has been related to dislocation loops in the film and may quench the excitonic transitions.(110,143) The I_V line at 2.774 eV has been associated to stacking faults by CL and TEM,(111,144) and is found to depend on the density of extended structural defects in

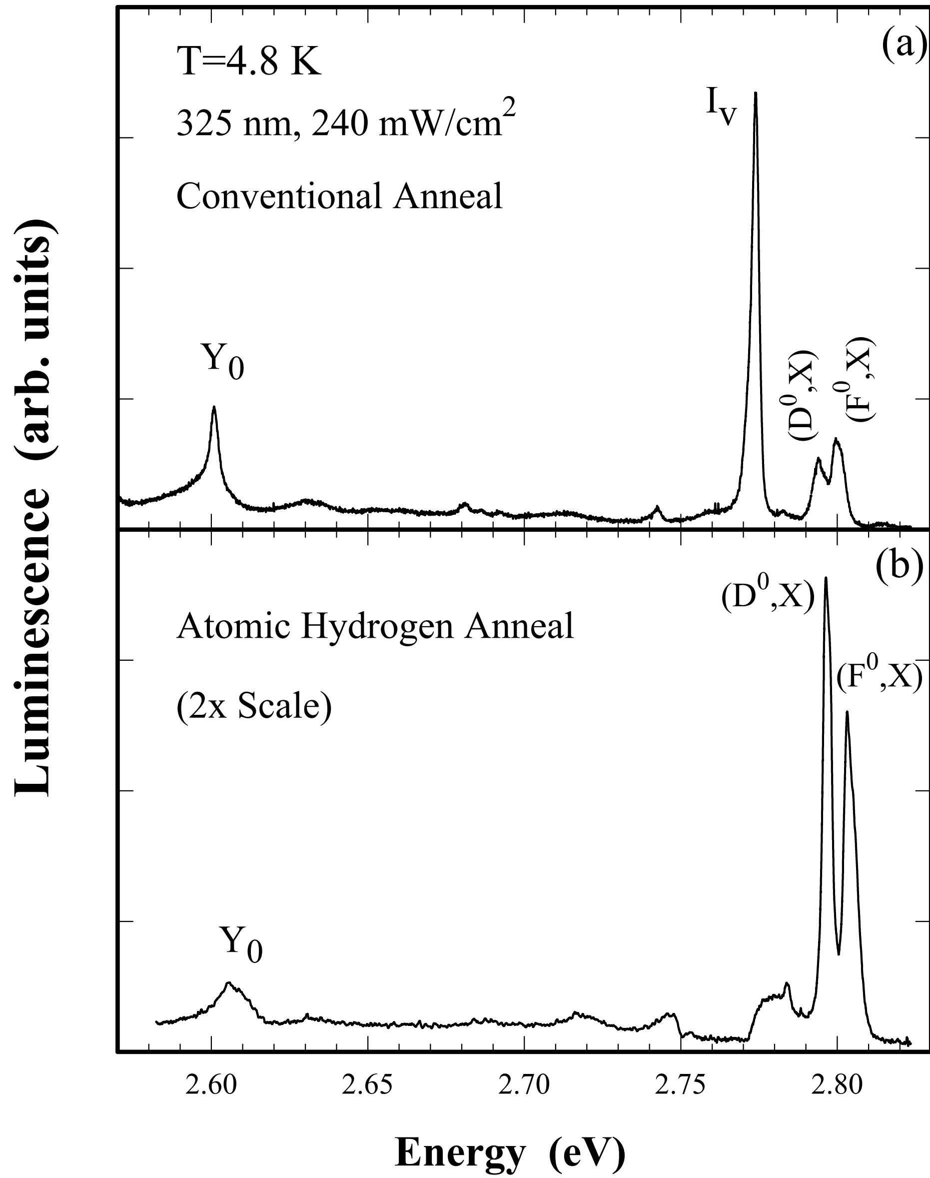

Fig. 3.5 Low-temperature photoluminescence spectra of undoped ZnSe/GaAs grown (a) with conventional thermal cleaning, (b) with atomic hydrogen cleaning (intensities shown are enhanced by factor of two).

the films.[110,142] Fig. 3.6 shows the PL spectra corresponding to the samples in Fig. 3. Fig. 3.5(a) exhibits very prominent I_v and Y_0 lines which can be attributed to the high defect density in the film. Exciton-related emissions were quite weak. In contrast, as shown in Fig. 3.5(b), features due to donor-bound excitons (D^0,X) and free excitons (F^0,X) were dominant in the undoped samples grown on substrates cleaned with atomic hydrogen. The very weak Y_0 line observed in Fig. 3.5(b) indicates that the film still has a low density of defects, possibly related to a residual background of threading dislocations. While it is possible to obtain PL spectra similar to Fig. 3.5(b) using a conventional thermal anneal and different growth conditions,[111] it is worth noting that the only difference between layers whose PL are shown in Fig. 3.5 was the substrate cleaning procedure. This underscores the importance of substrate preparation in determining overall layer quality.

Low-temperature PL spectra of all the atomic nitrogen-doped ZnSe films were dominated by a broad feature with peaks in the range of 2.50 to 2.65 eV, typical of heavily nitrogen-doped ZnSe layers.[85,97,114,145] Other transitions were either quenched or too weak to be detected. Although the PL lineshapes did not show a significant difference between samples grown with conventional thermal cleaning and those with atomic hydrogen cleaning, the peak intensity of the latter case was about twice that of the former case. This is a direct reflection of the decrease in the density of non-radiative defects.

3.4 Discussion

3.4.1 Defect Reduction by Atomic Hydrogen Cleaning of Substrate

It has been shown in this study that stacking fault density as low as 10^4 cm^{-2} of ZnSe thin films grown on GaAs substrate by MBE can be achieved by using atomic

hydrogen cleaning of substrate prior to epitaxial layer growth. Optical fluorescent microscopy and PL give consistent results on the presence of micro-defects in ZnSe epilayers. Those micro-defects, imaged by CL,[110,111] PL,[108] EL[105,106] and TEM,[56,135] proved to be stacking faults which normally appear in pairs. Such defects are also referred to as micro-twins.[113] In growth using conventional thermal cleaning, a Ga_2Se_3 interfacial layer can be formed on the Ga-rich surface during the initial stage of ZnSe growth.[63] This thin Ga_2Se_3 layer is believed to be the nucleation site for micro-defect formation since high concentration of vacancies existed in the structure.[63] A recent study by Wu *et al.*[140] indicates that a 2D growth mode at the initial growth stage is also critical to obtain a low defect density II-VI epitaxial layer on GaAs, in addition to the need for an As-rich GaAs surface. With a Zn exposure of the As-rich GaAs surface, a layer by layer 2-D growth mode is always obtained. The exposure of Zn could have one of the two results. Zn may modify the As-rich GaAs surface by eliminating excess As. Excessive As will cause a surface charge imbalance and lead to interface roughing and 3-D nucleation.[60] Instead, a slightly As-rich surface will result in a 2-D nucleation. Alternatively, the Zn may form a thin (2 to 3 atomic layer), atomically smooth Zn and As compound interfacial layer which will effectively suppress the formation of stacking faults.

As a result of atomic hydrogen cleaning, the GaAs substrate is cleaner and smoother as indicated by the flat feature AFM images and streaky RHEED patterns for the corresponding samples shown in Fig. 3.4 (b) and Fig. 3.1(c), respectively. The (2x4)As feature in Fig 3.1 (c) may indicate a slightly As-rich surface. Interestingly, the growth mode of samples with atomic hydrogen cleaning is 2-D as illustrated in Fig. 3.6. The initial layer by layer growth is indicated by the streaky RHEED pattern after the first 10 s growth as shown in Fig. 3.6(b). The resemblance between the two different

approaches strongly suggests a similar mechanism for lowering the defect density, possibly related to the surface status of GaAs prior to the ZnSe growth.

Although atomic hydrogen is proven to be very effective in cleaning GaAs substrates, the mechanism of this process is not fully understood. It seems that the atomic hydrogen not only cleans the surface better by effectively removing oxides, carbon, chlorine, sulfur and other common contaminants, but also produces a slightly As-rich GaAs surface, which was normally obtained by a much more complicated process.[56,140] Detailed studies by Yamada *et al.*[28] suggest a process which could create such a surface during atomic hydrogen cleaning. There are two types of Ga oxides on the GaAs surface, Ga_2O_3-like and Ga_2O-like. Ga_2O-like is volatile and easy to remove. At a relatively low temperature (above 300 °C)[28] anneal, Ga_2O-like and As oxides are easily desorbed, while the Ga_2O_3-like oxides are the last to be removed from the surface, and usually require a very high temperature (~ 600 °C) for desorption. However, the high temperature desorption of Ga_2O_3-like oxide is also accompanied by GaAs decomposition and As_2/As_4 desorption. The resultant surface after a high temperature anneal is largely Ga-rich. Since atomic hydrogen cleaning is usually performed at a moderate temperature (350 ~ 400 °C), the Ga_2O_3-like oxide can instead be removed through the formation of volatile Ga_2O and H_2O vapor,

$$Ga_2O_3 + 4H \rightarrow Ga_2O\uparrow + 2H_2O\uparrow$$

Therefore, this process removes Ga_2O_3 and removes excess Ga very effectively unaccompanied by As_2/As_4 desorption. An As-stabilized surface thus can be obtained as observed by RHEED.[27,137] Therefore, it seems that the rough surface with incomplete oxide removal left by conventional thermal cleaning is composed of mainly Ga oxides. Atomic hydrogen cleaning removes the Ga oxides so well that a very smooth and clean

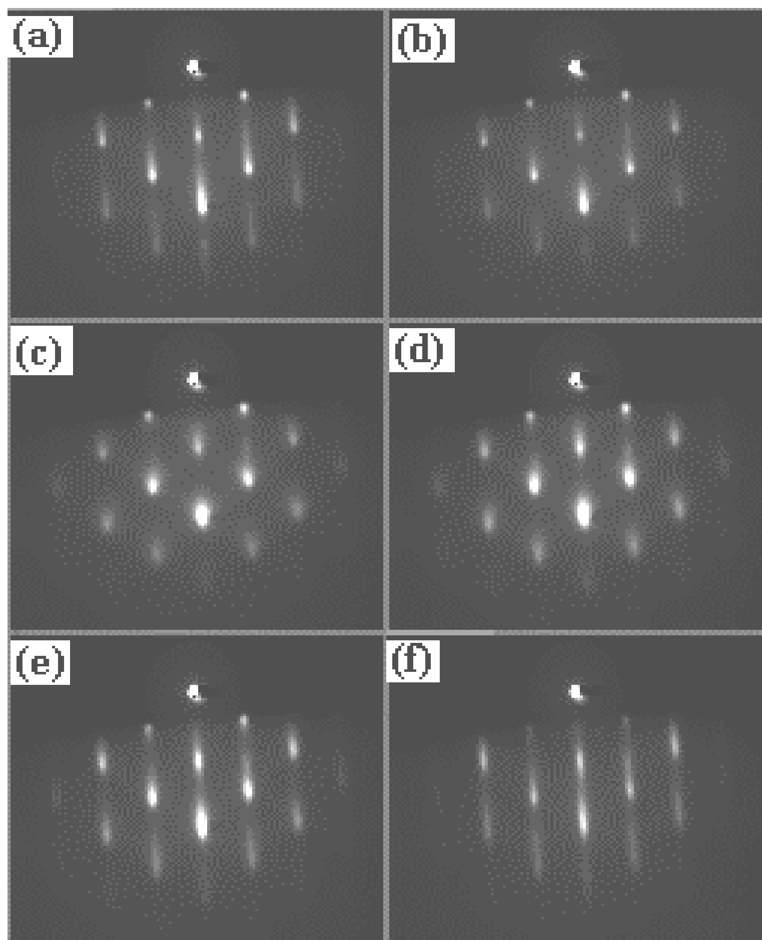

Fig. 3.6 RHEED of ZnSe grown on GaAs after the growth of (a) 0 s, (b) 10 s, (c) 30 s, (d) 1 min., (e) 2 min., and (f) 5 min. The electron beam is in the [110] azimuth.

GaAs surface is obtained.

As indicated in Ch. 2, the impingement rate of atomic hydrogen is about 8×10^{14} sec^{-1} cm^{-2} at a system partial pressure of 2×10^{-6} Torr during a typical atomic hydrogen cleaning. This corresponds to about one-half of an equivalent atomic hydrogen monolayer arriving per second. If the above reaction takes place as atomic hydrogen arrived on the surface, then two hydrogen atoms are needed to remove one Ga atom. Therefore, to remove one monolayer of Ga oxide, a total number of about 3×10^{15} hydrogen atoms are needed assuming a monolayer separation of 2.8 Å for Ga oxide. The RHEED pattern starts to change after the first 5 min of cleaning and becomes bright and streaky after 10 min. The total number of hydrogen atoms arrived in the substrate surface will be about 2 to 5×10^{17} over that time span. If the resultant RHEED pattern corresponds to the surface after one monolayer of Ga oxide removal, it implies that only about one percent of the total hydrogen atoms actually contribute to the surface reaction.

There are advantages in using atomic hydrogen cleaning over other types of substrate preparation. The first is the low substrate temperature needed to perform the cleaning. For GaAs surfaces, the atomic hydrogen cleaning can be accomplished at temperature less than 400 °C, while thermal cleaning must be carried out around 600 °C. The lower temperature can result in less cross-contamination from heated surfaces. The atomic hydrogen cleaning also results in an appropriate As-stabilized GaAs surface for subsequent ZnSe growth, eliminating the need for an As-flux. Particularly, it is very difficult to control the surface stoichiometry to obtain a lean As-surface using RHEED, because different As coverage surface will have same RHEED reconstruction pattern.[(140)] Additionally, atomic hydrogen has been shown to be effective at removing carbon and other surface impurities as well as oxides, resulting in a cleaner surface.[(29,138)] The primary advantage, however, is that this approach may eliminate the need for the growth

of a GaAs epilayer, resulting in a less complicated growth process for subsequent manufacture of layers for light-emitter fabrication.

3.4.2 Effect of Twin-related Defects on Nitrogen Doping

Achieving high p-type conductivity of ZnSe has been proven very difficult although it is easy to incorporate nitrogen to as high as 10^{20} cm^{-3} using an atomic nitrogen source as demonstrated in this study. The discrepancy between the acceptor dopants and net holes in the film indicates that compensation of acceptor dopants occurs. Studies on the compensation mechanism have been substantial.(13-19,96) Since a high defect density has been found in almost all ZnSe films, it would be interesting to see if there is any relation between the defect density and dopant compensation. As nitrogen concentration increases, the ZnSe lattice constant decreases.(96) However, the reduction in lattice constant is greater than can be explained by the shorter Zn-N bond distance of model predictions. It is likely that the generation of point defects accompanying nitrogen doping leads to further contraction of the lattice constant.(96) In addition, some studies indicate that the density of stacking faults increases with increasing nitrogen doping concentration.(116) The misfit dislocation structure at ZnSe/GaAs interface becomes a regular array of rectangular grids when nitrogen is incorporated in ZnSe,(96,116) instead of the 60° misfit dislocations occurred in undoped ZnSe. Thus, the question arises, "Are the twin-related defects and nitrogen compensation intimately related?".

In contrast to the above report(96) that the density of stacking faults increases as the nitrogen doping concentration increases, no observable increase of stacking faults in nitrogen-doped ZnSe samples over the undoped ZnSe samples was observed in this study, according to optical fluorescence microscopy. It is worth noting that all the atomic nitrogen-doped ZnSe samples studied are heavily doped and hence highly compensated. Thus the lack of a high density of stacking faults in these doped films implies that the

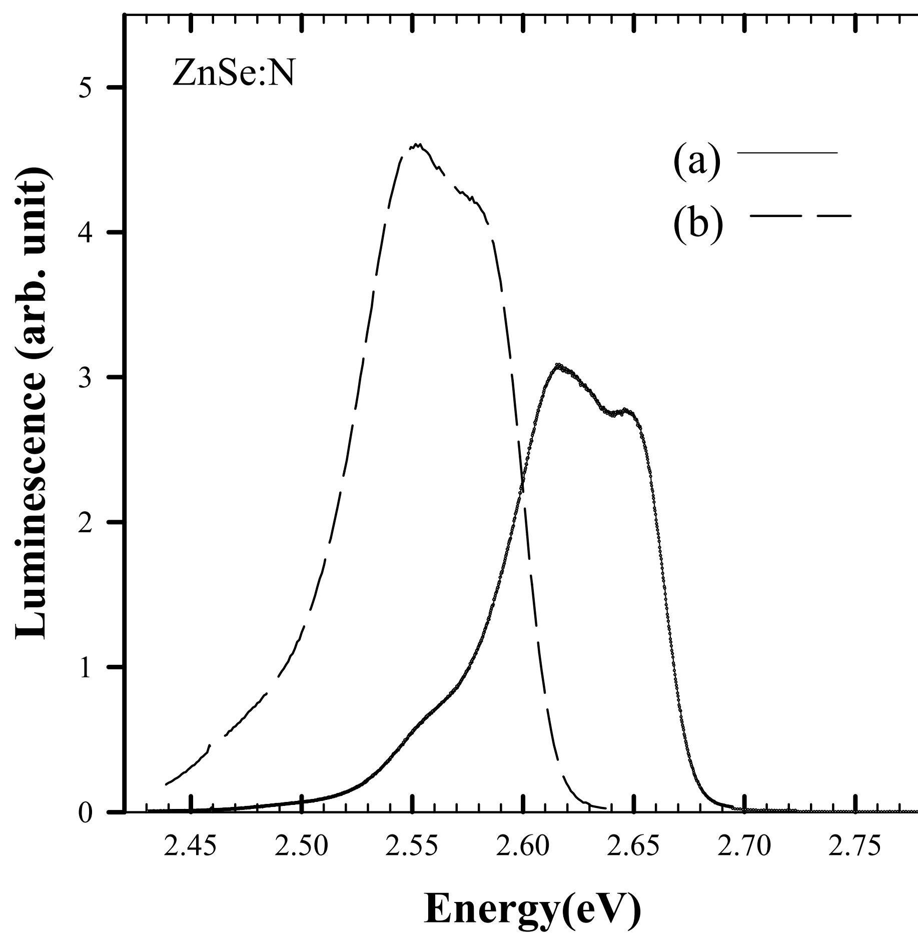

Fig. 3.7 Low-temperature photoluminescence spectra of nitrogen-doped ZnSe/GaAs grown (a) with conventional thermal cleaning, (b) with atomic hydrogen cleaning. The observed shift is due to different nitrogen concentration in the samples.

nitrogen doping is not the source of stacking faults, and conversely, the twin-related stacking faults are not the source of compensation. A speculation is that the increase in stacking fault densities could simply be a mis-interpretation of the variation from sample to sample because of the relatively high defect density (> 10^6 cm^{-2}) in all of their films.[116] On the other side, PL spectra of nitrogen-doped ZnSe using conventional thermal cleaning and atomic hydrogen cleaning show similar lineshapes, typical of heavily doped and highly compensated ZnSe films as illustrated in Fig. 3.7. Although the intensity of PL peaks for samples grown with atomic hydrogen cleaning is stronger, peak positions and lineshapes do not display significant differences for samples grown with either cleaning procedure. SIMS results also indicate comparable nitrogen concentrations in those samples for similar growth conditions. Therefore, the reduction of micro-defects in samples grown with atomic hydrogen cleaning does not seem to affect nitrogen incorporation in ZnSe. Micro-defects appear to primarily contribute to non-radiative luminescence and to act as nucleation sites for other structural defects such as dislocations which cause device degradation and failure. It can be concluded that the doping compensation mechanism in ZnSe is not driven by twin-related micro-defects.

CHAPTER IV

HYDROGEN-RELATED PHENOMENON

4.1 Role of Hydrogen in Semiconductors

Hydrogen is pervasive in semiconductors. It is a component of most chemicals used in the fabrication of electronic and photonic devices, is easily incorporated into semiconductors and it is a model impurity for studying defect reactions in solids.(22,23) Hydrogen passivation of deep level impurities and defects have been broadly investigated in Si and III-V compound semiconductors.(22,23) Recently, compensation by hydrogen has drawn attentions by researchers for II-VI compound semiconductors, particularly p-type doped ZnSe.(33,34,104) Once nitrogen proved to be an effective p-type dopant, hydrogen incorporation was examined for the potential bonding between nitrogen and hydrogen atoms in ZnSe(33,104) and other II-VI materials.(146) Experimentally, evidence for nitrogen and hydrogen bonding is found in MOCVD(33) and MOVPE(104) grown nitrogen-doped ZnSe by FTIR absorption measurements, with the absorption bands occurring at 3193 cm^{-1} and 783 cm^{-1}. These absorption bands have been associated with local vibrational modes of N-H bond in ZnSe. One can compare these bands to that observed in ammonia, and due to nitrogen-hydrogen bonding in GaAs and GaP.(104) SIMS measurements show that the hydrogen concentration is comparable to the nitrogen level in layers of nitrogen-doped ZnSe grown by GSMBE.(34) In MOCVD and MOVPE growth of ZnSe:N, it is typical to use ammonia as the doping source and hydrogen as the carrier gas, while in GSMBE H_2Se is used as the Se source. Therefore, the presence of hydrogen during growth is due to the nature of the growth technique or the choice of source material. Observations of hydrogen incorporation in ZnSe:N films grown by MOCVD, MOVPE and GSMBE indicate that hydrogen effectively passivates nitrogen in these nitrogen-doped ZnSe layers. Since the hydrogen source is not unique in those

growth methods, the mechanism of hydrogen passivation can not be uniquely determined. In addition, the hydrogen partial pressure during those growths is very high. Thus, it is difficult to further understand at what level hydrogen passivation will start to effectively compensate nitrogen doping. Therefore, it is necessary and useful to examine conditions for hydrogen incorporation in ZnSe by using a single, controllable hydrogen source.

It is important to understand the effect of hydrogen on the MBE growth of ZnSe. To date the best ZnSe-based films and devices are grown by MBE,[(5,21)] and most efforts in improving material and device processing have also been focused on the MBE technique. However, p-type doping compensation in ZnSe has been one of the major problems hampering device fabrications of the material system. Hydrogen is the main residual gas in a UHV background. It is not clear whether this residual hydrogen plays a role in the doping process in ZnSe grown by MBE as it does in MOCVD, MOVPE, or GSMBE. By intentionally introducing hydrogen into ZnSe growth, the effect of hydrogen on nitrogen doping can be solely determined. In a further step, with different combinations of atomic hydrogen, molecular hydrogen, atomic nitrogen and molecular nitrogen present during the growth, one can obtain information on the hydrogen-nitrogen interaction in MBE growth of ZnSe for various growth conditions. In this study, MBE growth has been arranged to carry out the above objective. The resulting samples are characterized by SIMS to determine the doping profile in the samples, by FTIR to detect N-H bonding through observation of vibrational absorption bands, by PL to measure luminescent transitions in the energy gap for determining defect and impurity levels, and by Hall measurements. This chapter will first describe the experimental procedures, and then give results on the characterization of samples. Finally, discussions of the effects related to hydrogen in ZnSe grown by MBE will be presented.

4.2 Experimental Procedures

ZnSe films were grown on semi-insulating (100) GaAs substrates (Table 2.7). Substrates were solvent cleaned and chemical etched before being loaded into the vacuum chamber. Surface oxide removal was performed using atomic hydrogen cleaning at 400 °C for 20 min. with the hydrogen source operating at 9.5 amps on current regulation mode and hydrogen partial pressure at $2x10^{-6}$ Torr. High purity (7N) elemental Zn and Se were used for the II and VI source materials, respectively. Both Se-rich and Zn-rich growth condition samples were grown with a Zn/Se flux ratio ranging between 0.5 and 2. Growth temperatures were 250 and 300 °C, respectively. Nitrogen doping was achieved by the rf plasma atomic/radical nitrogen source (Oxford CARS25). The nitrogen source was typically operating with a plasma power between 150 to 300 W and a nitrogen flow between 1 to $6x10^{-6}$ Torr system pressure, depending on the aperture used. For doping with molecular nitrogen, the plasma power of the nitrogen source was turned off while nitrogen gas was flowing through the plasma chamber. The atomic hydrogen source was the same one used for substrate cleaning. To introduce atomic hydrogen, the growth was interrupted by inserting the substrate shutter to prepare for the hydrogen source. Hydrogen flow was varied to obtain a system pressure which ranged from $1x10^{-9}$ to $1x10^{-5}$ Torr ($1x10^{-6}$ Torr typical) by controlling a precision UHV leak valve between the hydrogen source and the high purity hydrogen gas tank. Growth was resumed by opening the substrate shutter, thus exposing the growing surface to an atomic hydrogen flux. For exposure to molecular hydrogen, the hydrogen source power was simply turned off while hydrogen gas is flowing.

Deuterium was used to replace hydrogen in some growths. The reasons for using deuterium are that deuterium is easier to detect than hydrogen in a SIMS measurement because deuterium is less abundant than hydrogen in the air, yielding at least two orders magnitude improvement in the SIMS detection limit, and deuterium allows a clean

investigation of N-H bonding in ZnSe through isotope related effects. Since the isotopic shift in vibrational frequency of hydrogen bond is unique for a particular H-X bond (X is the other atom attached to H), the observation of an isotope shift is a signature of the corresponding H-X bond. This approach is widely used for confirming bond formation with hydrogen in other material systems.(22) Deuterium was introduced to growth through the hydrogen source, which has a valve system to allow switching between hydrogen and deuterium sources.

The sample thickness was nominally about 2 μm, which was measured by a ZnSe witness layer deposited simultaneously on a sapphire disk sitting beside the GaAs substrate. The thickness was determined by the interference fringes in the transmittance of the ZnSe witness layer on the sapphire. The transmittance spectra were taken using a Cary-14 spectrometer. The growth rate was about 0.4 μm/h for Se-rich condition, and 0.3 μm/h for Zn-rich condition. All doped samples are grown with a one hour undoped ZnSe buffer layer prior to the doping growth. Samples grown with different configurations of hydrogen and nitrogen atomic form are listed in Table 4.1. A complete description of the growth conditions for each sample can be found in Appendix A.

ZnSe growth was monitored by *in-situ* RHEED, especially during the initial stage of the growth. Doping and impurity concentrations were examined by SIMS measurement on a selected set of samples. Low-temperature and room-temperature PL were performed for all ZnSe samples. Absorption bands of vibrational modes were measured by FTIR. Hall measurements were used to obtain carrier concentrations and mobilities of ZnSe films. For undoped ZnSe, indium was used for the ohmic contact metal. For nitrogen-doped ZnSe, a thin layer of heavily doped ZnTe:N was deposited on ZnSe:N, the ZnTe:N layer was then etched away except for the contact regions at four corners which were covered by photoresist. Au from $AuCl_3$ was used for the ohmic contact metal on ZnTe:N.

Table 4.1: Samples Grown with Various Hydrogen/Nitrogen Configurations

	ZnSe	ZnSe:N
undoped	ZnSe (9627, 9602)	ZnSe:N (9536, 9603)
under atomic H	ZnSe:H (9610)	ZnSe:N,H (9612, 9616)
under atomic D	ZnSe:D (9613)	ZnSe:N,D (9614, 9620)
under molecular H		ZnSe:N,H_2 (9541)
under molecular D		ZnSe:N,D_2 (9621)

4.3 Results

4.3.1 Reflection High Energy Electron Diffraction

The initial growth of ZnSe was monitored by RHEED and illustrated in Fig. 3.6. At the beginning of the ZnSe growth, a smooth (2x4)As surface was indicated by the streaky RHEED pattern in Fig. 3.6(a). After first 10 s of the growth, about 10 Å (corresponding to 3 to 4 monolayer) of ZnSe was deposited. The observed RHEED pattern (Fig. 3.6(b)) showed streaky features, indicating a layer by layer growth and smooth growing surface. Fig. 3.6(c) corresponds to a surface after 30 s of growth which corresponds to about 10 monolayers. The spotty features may be due to surface roughening due to interfacial misfit dislocation generation. After 1 min. of growth, the surface was becoming smoother, as indicated by the RHEED pattern (Fig. 3.6 (d)) which again became quite streaky. Figs. 3.6(e) and (f) were RHEED patterns after 2 min. and 5 min. of growth, the presence of streaks indicated that a 2-D growth was established. The

RHEED pattern at the end of the ZnSe growth was also streaky. For nitrogen-doped growth of ZnSe, the initial growth on ZnSe was always found to proceed as 2-D growth. However, a 3-D RHEED pattern was observed for some of the nitrogen-doped samples at the end of growth. This transition from 2-D to 3-D growth modes was not fully understood since a clear trend of RHEED pattern related to growth parameters was not observed.

4.3.2 Secondary Ion Mass Spectrometry

Secondary ion mass spectrometry measurements are made to determine the doping concentration profiles in ZnSe samples using Cs+ ions as the probing beam. SIMS measurement on an undoped ZnSe sample indicates a background in the SIMS instrument itself of nitrogen at $1x10^{17}$ cm^{-3} and hydrogen at $2x10^{18}$ cm^{-3}. Deuterium was at zero counts, representing a minimum detectability of $5x10^{16}$ cm^{-3}. These levels served as a guideline for the background of those species in subsequent SIMS measurement of ZnSe. Fig. 4.1 shows the SIMS depth profile of a nitrogen-doped ZnSe sample. The nitrogen concentration is about $1.5x10^{19}$ cm^{-3} and hydrogen is in the SIMS background level. The drop in nitrogen concentration near the ZnSe/GaAs interface at ~ 1.8 μm corresponds to the undoped ZnSe buffer layer. The nitrogen and hydrogen concentration depth profile for a nitrogen-doped ZnSe sample grown under a hydrogen flux is shown in Fig. 4.2(a). The nitrogen concentration is $3x10^{19}$ cm^{-3} in the doped layer. Surprisingly, the hydrogen level is $5x10^{20}$ cm^{-3} in this doped layer, representing a concentration of almost one atomic percent. The variation in hydrogen concentration throughout the sample's depth closely tracked that of nitrogen. During the growth of the layer, the plasma was inadvertently turned off while maintaining the nitrogen flow with atomic hydrogen was always present. The hydrogen incorporation is clearly modulated

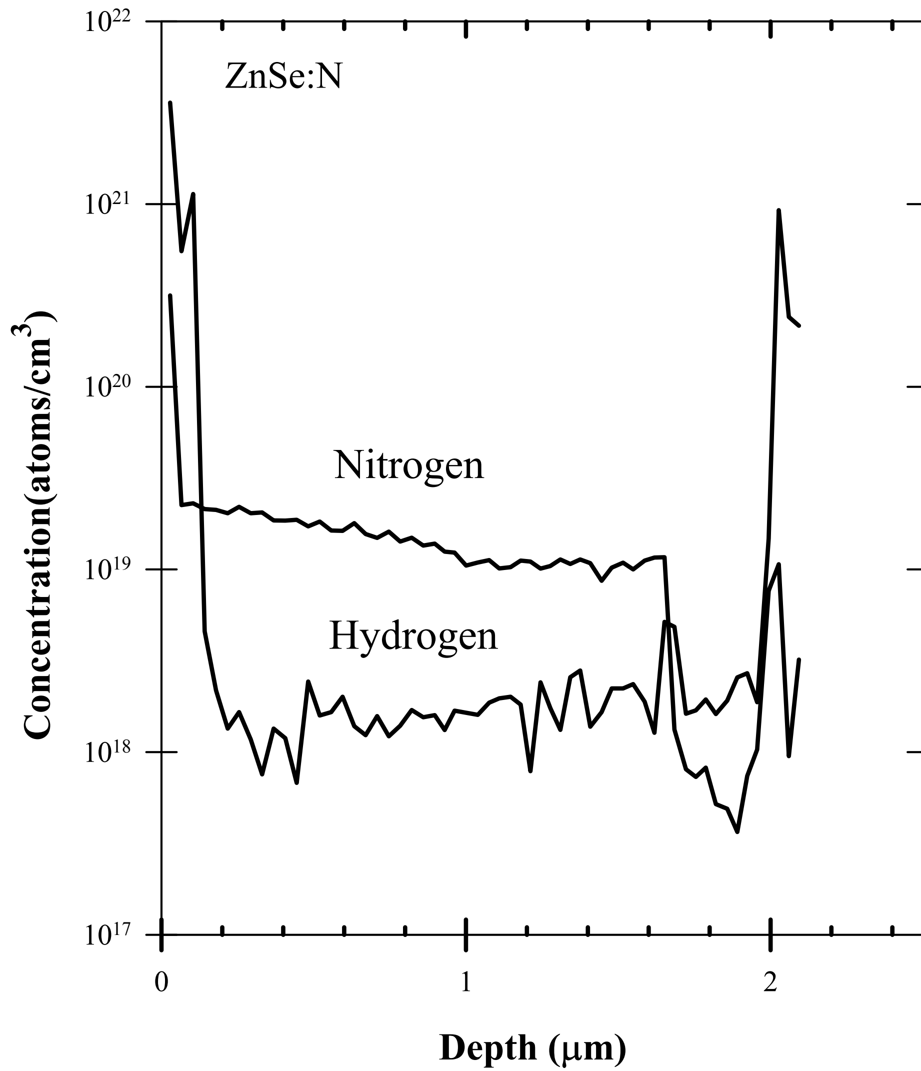

Fig. 4.1 Secondary ion mass spectrometry depth profile of nitrogen-doped ZnSe. The drop in nitrogen concentration near the ZnSe/GaAs interface corresponds to the undoped ZnSe buffer layer.

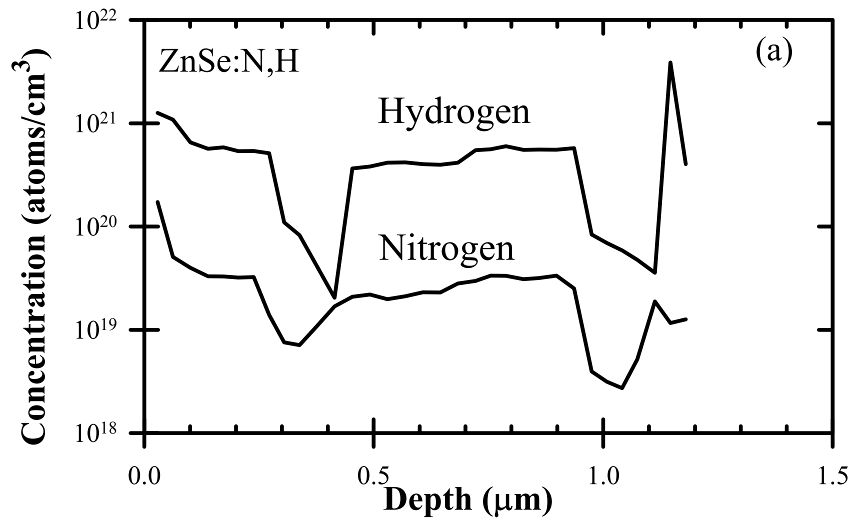

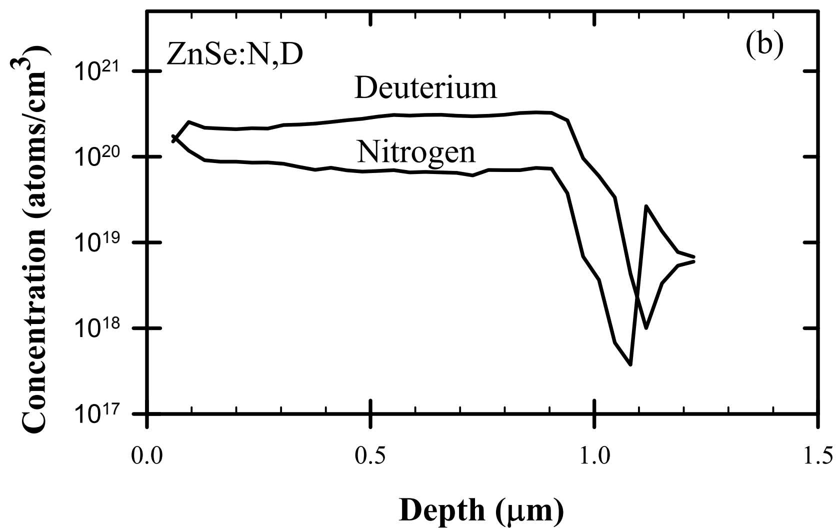

Fig. 4.2 Secondary ion mass spectrometry depth profile of (a) ZnSe:N,H, (b) ZnSe:N,D.
The drop in concentrations near the ZnSe/GaAs surface corresponds to the undoped ZnSe buffer layer while the drop near the sample surface in

(a) corresponds to switching from atomic to molecular nitrogen during the growth.

by nitrogen incorporation in the ZnSe similar to the phenomenon observed in nitrogen-doped ZnSe grown by GSMBE.[34] For several layers, deuterium was used during nitrogen-doped ZnSe growth to investigate both the nature of the N-H bond through isotopic substitution and low-level incorporation of hydrogen. Fig. 4.2(b) shows the SIMS depth profile of a nitrogen-doped ZnSe sample grown under a deuterium flux. The nitrogen concentration is $8x10^{19}$ cm^{-3} and the deuterium concentration is $3x10^{20}$ cm^{-3}, again at a surprisingly high level in the doped layer.

Table 4.2 contains a summary of hydrogen, deuterium and nitrogen concentrations for various growth conditions. Hydrogen incorporation in ZnSe was significant only when both atomic hydrogen and atomic nitrogen were present during the growth (ZnSe:N,H). In nitrogen-doped ZnSe exposed to molecular deuterium during growth (ZnSe:N,D_2), a deuterium level at 10^{18} cm^{-3} and nitrogen level at $8x10^{19}$ cm^{-3} were observed, indicating a low hydrogen incorporation efficiency for molecular *vs*. atomic deuterium. In addition, a measurable deuterium incorporation was not observed for undoped layers grown under an atomic deuterium flux. This low "cracking" efficiency indicates that the background levels of molecular hydrogen typically found in an MBE system are not an issue for compensation of nitrogen-doped ZnSe. Hydrogen incorporation in ZnSe also depends on the growth conditions. The highest nitrogen and hydrogen concentrations are obtained for Zn-rich conditions and at the lower growth temperatures. The highest hydrogen level is $5x10^{20}$ cm^{-3}, more than one order higher than the nitrogen level in the same layer. As expected, Zn-rich conditions are more favorable to nitrogen incorporation in ZnSe since nitrogen occupies a Se site for p-type doping in ZnSe.[84]

Table 4.2: Hydrogen, Deuterium and Nitrogen Concentrations In ZnSe for Various Growth Conditions*

Sample	T_{growth} (°C)	Zn/Se ratio	N flux ($x10^{-6}$ torr BEP)	[N] ($x10^{19}$ cm^{-3})	[H] or [D] ($x10^{19}$ cm^{-3})
ZnSe:N,H	250	1.8	3.0	3.0	50
ZnSe:N,D	250	2.0	4.7	8.0	30
ZnSe:N,D	250	0.6	4.7	1.5	1.8
ZnSe:N,D	300	0.5	15	0.4	1.0
ZnSe:N	300	0.5	3.2	1.5	background
ZnSe:D	300	0.5	0	background	background
ZnSe:N,D_2	300	1.2	5.1	8.0	0.1

* The nitrogen source rf power was 200 W and the hydrogen/deuterium pressures were maintained at $1x10^{-6}$ Torr whenever present.

4.3.3 Fourier Transform Infrared Spectroscopy

Fourier transform infrared spectroscopy is performed at room-temperature and 15K on the ZnSe samples using a Nicolet model 550 FTIR spectrometer. Absorption bands are observed at 783 cm^{-1} and 3193 cm^{-1} in nitrogen-doped ZnSe samples grown under an atomic hydrogen flux as shown in Fig. 4.3, which corresponds to the sample whose concentration depth profile is shown in Fig. 4.2(a). These peaks are absent from ZnSe samples grown only with atomic nitrogen or atomic hydrogen flux, as well as from undoped ZnSe samples. Similar features were observed at 783 cm^{-1} and 3194 cm^{-1} in nitrogen-doped ZnSe grown by MOVPE(104) and at 3194 cm^{-1} in nitrogen-doped ZnSe grown by MOCVD.(33) The 3194 cm^{-1} band has been tentatively assigned to the stretching mode, and 783 cm^{-1} band to the wagging mode of the N-H bond in ZnSe(104) based on absorption bands observed in ammonia(22) and N-H bonding in GaAs and GaP.(147)

The effect of isotopic substitution on the observed vibrational frequency is very useful for the identification of the species that comprise a defect complex.(22,148) For example, the large frequency shift that results upon the substitution of deuterium for hydrogen can lead to an unambiguous assignment of the hydrogen bonding. In the harmonic oscillator approximation, the vibrational frequency of an X-H oscillator is assumed to be inversely proportional to the square root of the reduced mass of the oscillator,

$$\omega(H) \propto \frac{m_X m_H}{m_X + m_H} \tag{4.1}$$

where m_H and m_X are the masses of hydrogen and the other atom, respectively. The r-factor, defined as:

$$r = \frac{\omega(H)}{\omega(D)} \qquad (4.2)$$

is the ratio of the vibrational frequencies observed for the isotopic substitution, D for H. Hence, for an ideal harmonic oscillator,

$$r = \sqrt{\frac{2(m_X + 1)}{(m_X + 2)}} \qquad (4.3)$$

for X, H and D atoms of masses m_X, 1 and 2, respectively. For a particular atom attached to hydrogen, the frequency shift can be predicted by the r-factor. The calculated r-factor is 1.369 for a N-H bond which can be compared to the experimental value of 1.342 for the N-H bond stretching mode in ammonia. The decrease is due to the fact that nitrogen is also bonded to other atoms. In the nitrogen-doped ZnSe sample grown under a deuterium flux by MBE, an absorption band is observed at 2368 cm^{-1} as shown in Fig. 4.4, which corresponds to the sample with the concentration depth profile in Fig. 4.2(b). Taking this 2368 cm^{-1} band and the 3194 cm^{-1} band in the ZnSe:N,H sample as the set of vibrational frequencies corresponding to N-D and N-H bonds respectively, the ratio is calculated to be 1.348. The excellent agreement between this value, that of ammonia, and with the predicted value of r-factor leads us to conclude that the 2368 cm^{-1} absorption band belongs to the N-D stretching mode in ZnSe. This result unambiguously identifies that N-H bonding is occurring in the ZnSe:N,H samples.

Another interesting aspect of this study is the large concentration of hydrogen observed for samples grown under Zn-rich conditions. Theoretical studies, such as the recent one by Neugebauer and Van de Walle[149] concerning GaN, indicate that hydrogen is more stable (and thus highly incorporated) in p-type than n-type material in agreement

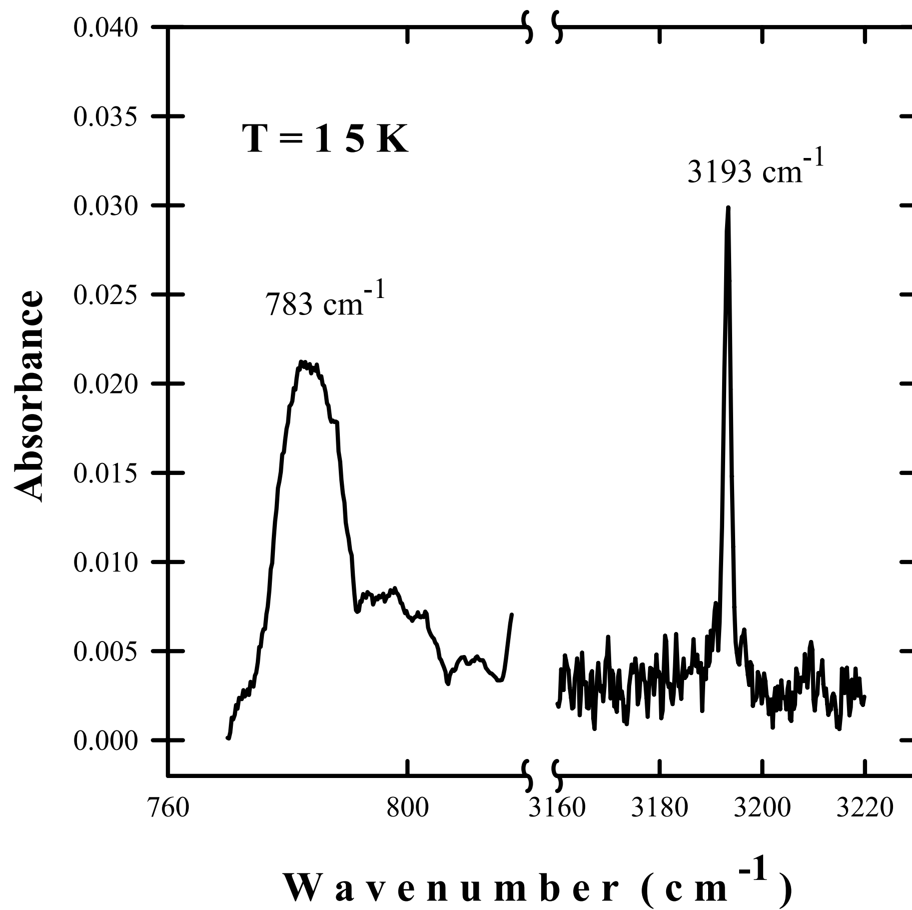

Fig. 4.3 Fourier transform infrared spectroscopy spectrum of ZnSe:N,H. The absorption bands at 783 cm^{-1} and 3193 cm^{-1} correspond to the N-H bond wagging mode and stretching mode, respectively.

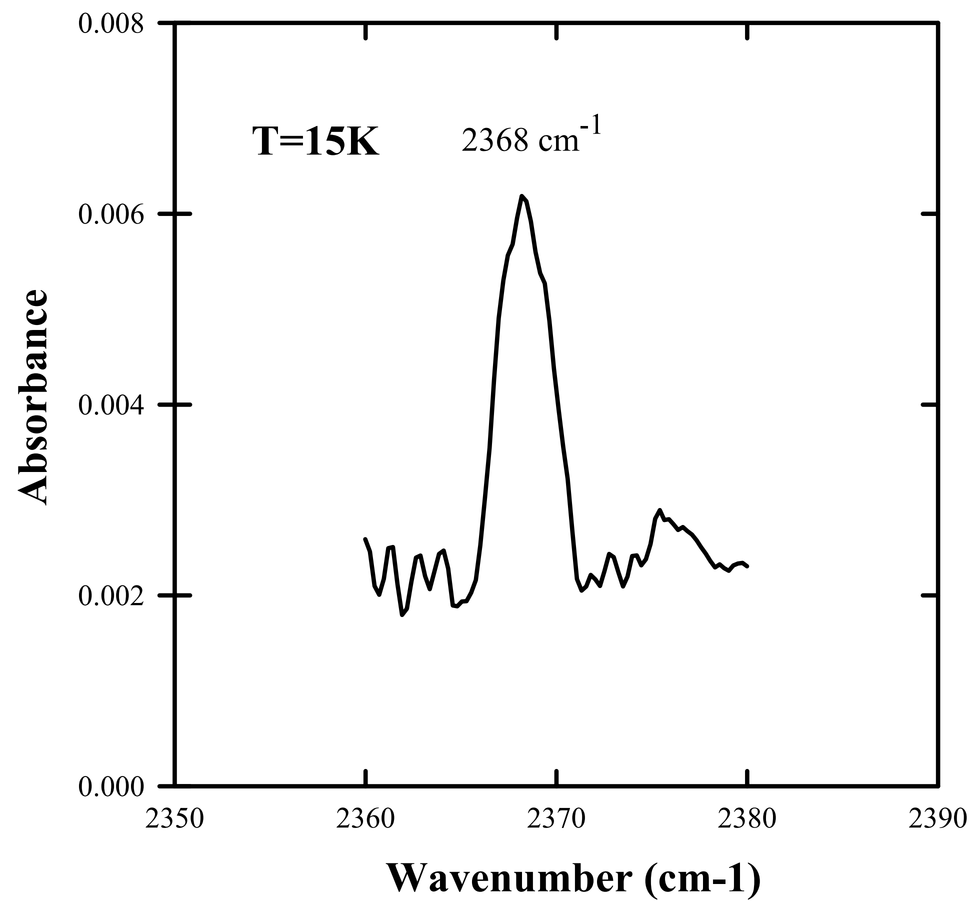

Fig. 4.4 Fourier transform infrared spectroscopy spectrum of ZnSe:N,D. The absorption band at 2368 cm^{-1} corresponds to the stretching mode of N-D bond.

with the present study. Neugebauer's calculation implies a one-to-one incorporation of hydrogen-to-acceptor, which is what we essentially observed for Se-rich ZnSe:N,H growth and for hydrogen incorporation in nitrogen-doped CdTe in a previous study.[146] It is not clear how the "excess" hydrogen is being incorporated in the samples grown for this study based on the measurements made to date. One possibility is that hydrogen is incorporating on vacancy sites (either Zn or Se) similar to observations for Si and Ge.[25]

Other LVMs for Zn-H, Zn-D, Se-H and Se-D bonds have been reported in ZnSe samples prepared by ion implantation techniques.[150] Tatarkiewicz *et al.*[150] observed the LVMs of Zn-H and Se-H at 1315 cm^{-1} and 2150 cm^{-1} respectively in H implanted ZnSe with a H concentration about 1.35×10^{21} cm^{-3}. The isotopic shifts of the corresponding LVMs were also observed when D replaces H for the implantation, with the absorption bands occurred at 950 cm^{-1} and 1560 cm^{-1} for Zn-D and Se-D bonds, respectively.[150] However, these features are not observed in our samples. Since the doped layer thickness is different from sample to sample, for a better evaluation of contribution from a particular vibrational center to the absorption band in the sample, we could use the total number of dopant atoms per cm^{-2} which represents a cross-section for absorption, assuming that all these atoms will form oscillators, to estimate the possibly observable absorption. In Tatarkiewicz's study,[150] 6×10^{17} atoms cm^{-2} of hydrogen gave a peak intensity of 0.05 (0.017) in absorbance for Se-H (Zn-H) bonding at 2150 cm^{-1} (1315 cm^{-1}). The highest hydrogen concentration is 5×10^{20} cm^{-3} in our nitrogen-doped ZnSe layers which corresponds to 5×10^{16} atoms cm^{-2} of hydrogen. Assuming the absorbance linearly increases with the increase of oscillating centers, one would expect an absorption peak intensity of less than 0.005 around 2150 cm^{-1} for the Se-H bond in the above sample. Practically, this signal level is very close to the noise background of the instrument and hard to detect even without any interference from other interactions such as N-H bonding.

4.3.4 Photoluminescence

As shown in Fig 3.5(b), low-temperature PL spectra of undoped ZnSe samples were dominated by strong excitonic features with free exciton (F^0,X) and donor-bound exciton (D^0,X) transitions at 2.802 and 2.798 eV, respectively. Fig. 4.5 shows the PL spectra of ZnSe:N and ZnSe:N,H samples at low-temperature. The PL spectrum of the ZnSe:N sample is represented by the dashed line in Fig. 4.5. It is a typical lineshape of heavily doped and highly compensated nitrogen-doped ZnSe, with a broad peak ranged between 2.5 and 2.65 eV.[85,97,114,145] This feature, typically identified as donor-acceptor pair recombination,[85,97,145] is completely quenched in the ZnSe:N,H sample as indicated by the solid line in Fig. 4.5. However, a new, deep level feature centered at 2.10 eV appears in the films grown with atomic hydrogen. This feature appeared in all samples grown with atomic hydrogen or atomic deuterium, indicating that it is hydrogen related.

For undoped ZnSe grown under an atomic hydrogen flux, the PL spectrum is different from that of undoped ZnSe samples grown without atomic hydrogen. Fig. 4.6 shows the low-temperature PL spectrum of an ZnSe layer grown with atomic hydrogen. The 2.794 eV line can be attributed to an acceptor-bound exciton (see Table 2.4). The peak at 2.782 eV is significantly stronger than that observed for undoped ZnSe (Fig. 3.5(b)) in the near band edge emission region, while the (D^0,X) and (F^0,X) peaks are relatively weaker than for typical undoped layers. This 2.782 eV peak is normally observed in low doped p-type ZnSe and attributed to a deep acceptor-bound exciton.[59,77] A strong and broad emission around 2.72 eV, which has been reported in As and nitrogen-doped ZnSe[78,87] and whose origin is unidentified, also appears in the free electron-to-acceptor (e,A^0), donor-to-free hole (D^0,h) or DAP transition range in these samples. This peak is accompanied by phonon replicas, indicative of DAP. Assuming a normal shallow donor energy of 30 meV, the acceptor energy is estimated to be about 90 meV assuming a 20 meV pair term. This energy is very close to that for a P acceptor in

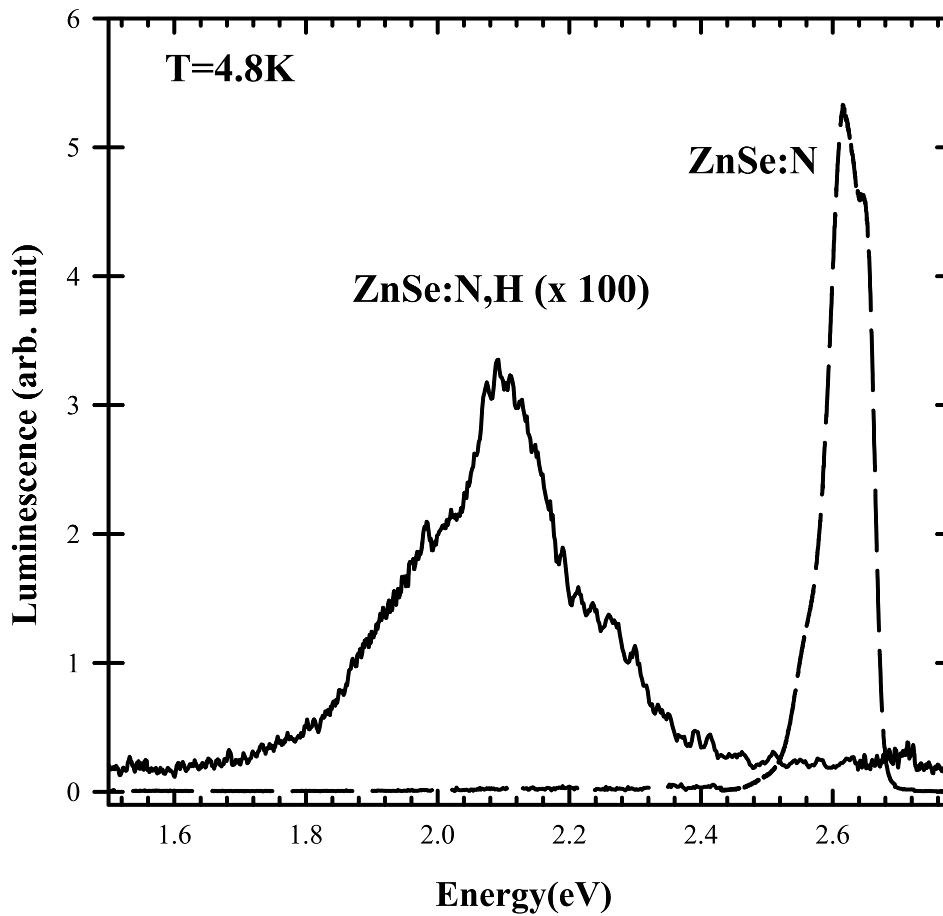

Fig. 4.5 Photoluminescence spectra of ZnSe:N (dashed line) and ZnSe:N,H (solid line). The PL feature in ZnSe:N is a typical lineshape of heavily nitrogen-doped ZnSe, and the new feature (representing a deeper level) in ZnSe:N,H is hydrogen related.

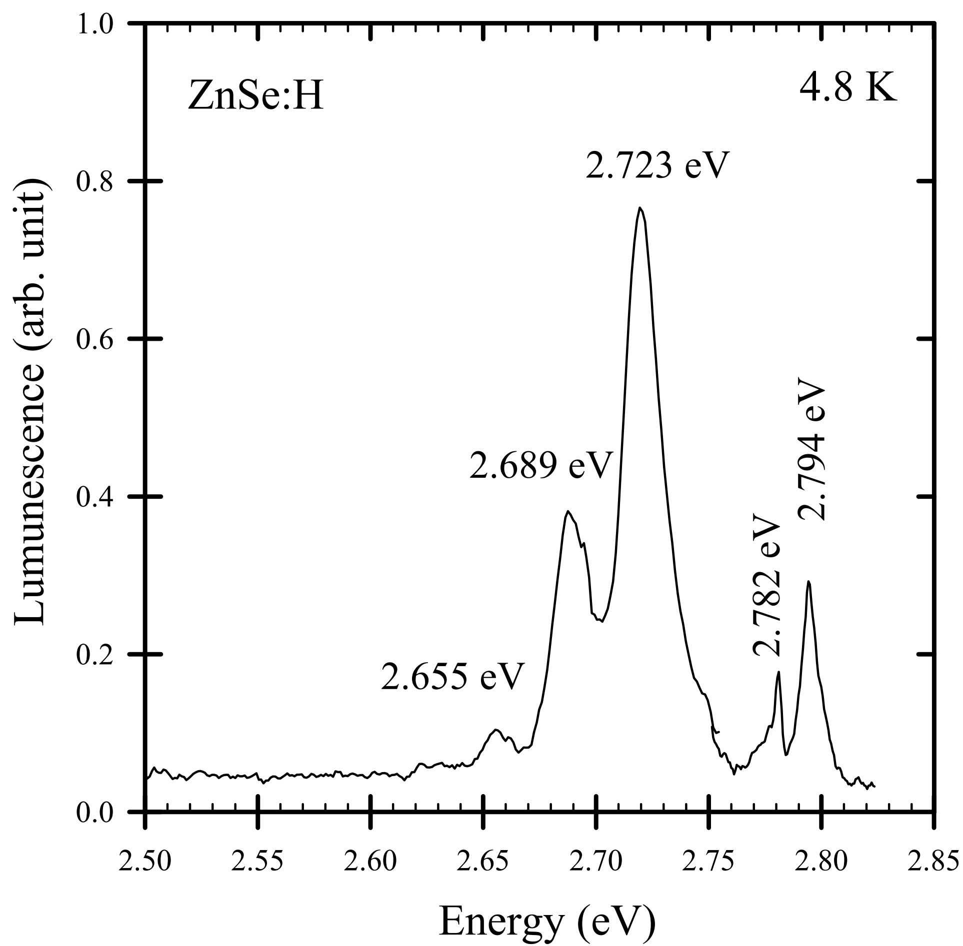

Fig. 4.6 Low-temperature PL spectrum of ZnSe grown under an atomic hydrogen flux.

ZnSe.[132] However, this has been reported in As-doped ZnSe.[78] In addition, the structural defect related transitions I_V and Y_0 lines are further suppressed in those undoped ZnSe grown with atomic hydrogen samples, which may imply that these defects are further reduced in these layers. The origin of the peak at 2.782 is not clear at the moment. This line was quite weak in the undoped ZnSe samples grown without atomic hydrogen, and previous reports in low level nitrogen-doped ZnSe[59] indicate this PL could be from residual species (such as As, O, and S) auto-doping, which is possibly enhanced by the presence of atomic hydrogen. Room-temperature PL of a ZnSe sample grown with atomic hydrogen and an undoped sample are shown in Fig. 4.7. The data was taken using a 441.6 nm line from a He-Cd laser and a power density of 24 W/cm^2. The spectra were not corrected for system response. The PL lineshape for the ZnSe:H sample is the same as for the undoped ZnSe. Others have reported this.[87] However, the undoped ZnSe and the ZnSe:H are completely different at low temperatures. Thus, the identical PL from both types of samples at room-temperature strongly suggests that the room-temperature PL comes from intrinsic processes such as band-to-band or excitonic recombinations. Similar to room-temperature PL based on such intrinsic recombination as has been reported for CdTe.[166,167]

The PL spectrum of a nitrogen-doped ZnSe layer grown with molecular nitrogen (nitrogen source plasma was turned off) is shown in Fig. 4.8. The BEP of molecular nitrogen flux was 4.1x10^{-5} Torr. The PL lineshape is a typical of low concentration nitrogen-doped ZnSe,[11] and is similar to those of p-type ZnSe doped *via* nitrogen gas as reported by earlier workers.[80,81] The spectrum is dominated by the strong nitrogen-acceptor-bonded exciton ($A^0_N X$) at 2.790 eV and by DAP at 2.695 eV. Both the $A_N X$ and the DAP exhibited a strong series of LO-phonon replicas. (F^0,X) and (D^0,X) transitions were also observed. The presence of the Y_0 line indicates that some residual structural defects exist in the epilayer. The room-temperature PL spectrum was similar to

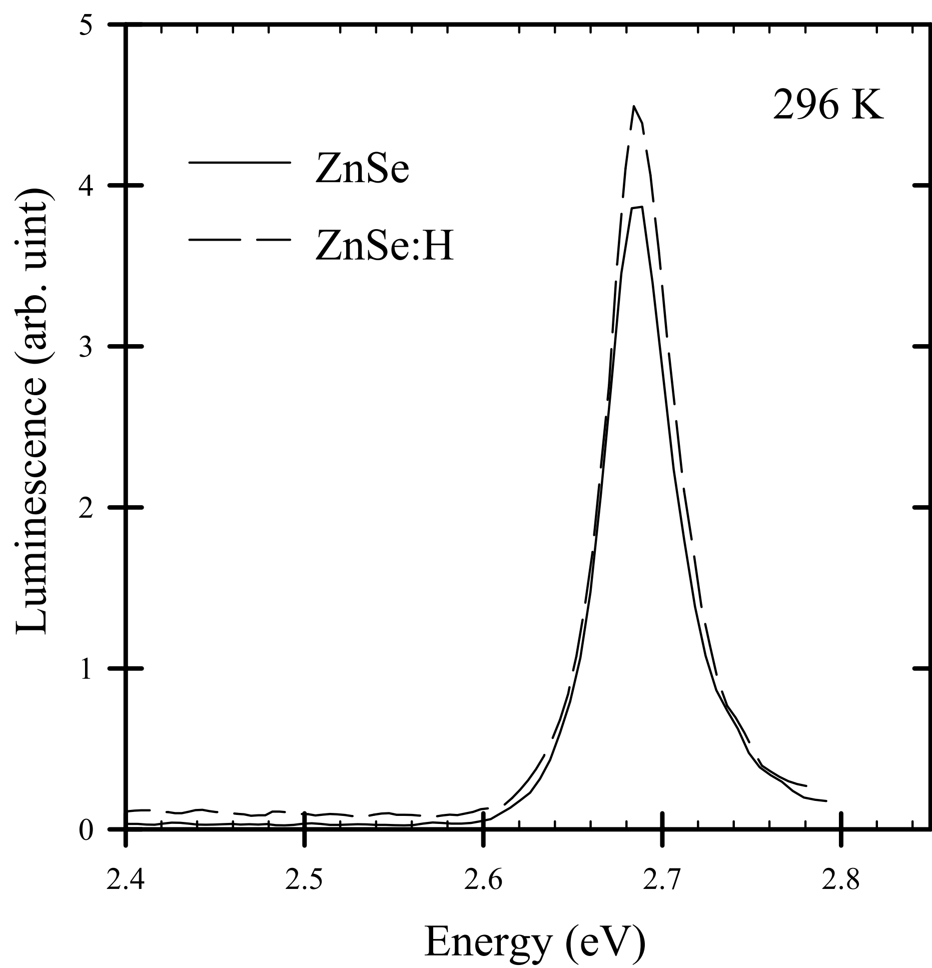

Fig. 4.7 Photoluminescence spectrum of ZnSe and ZnSe:H at room-temperature.

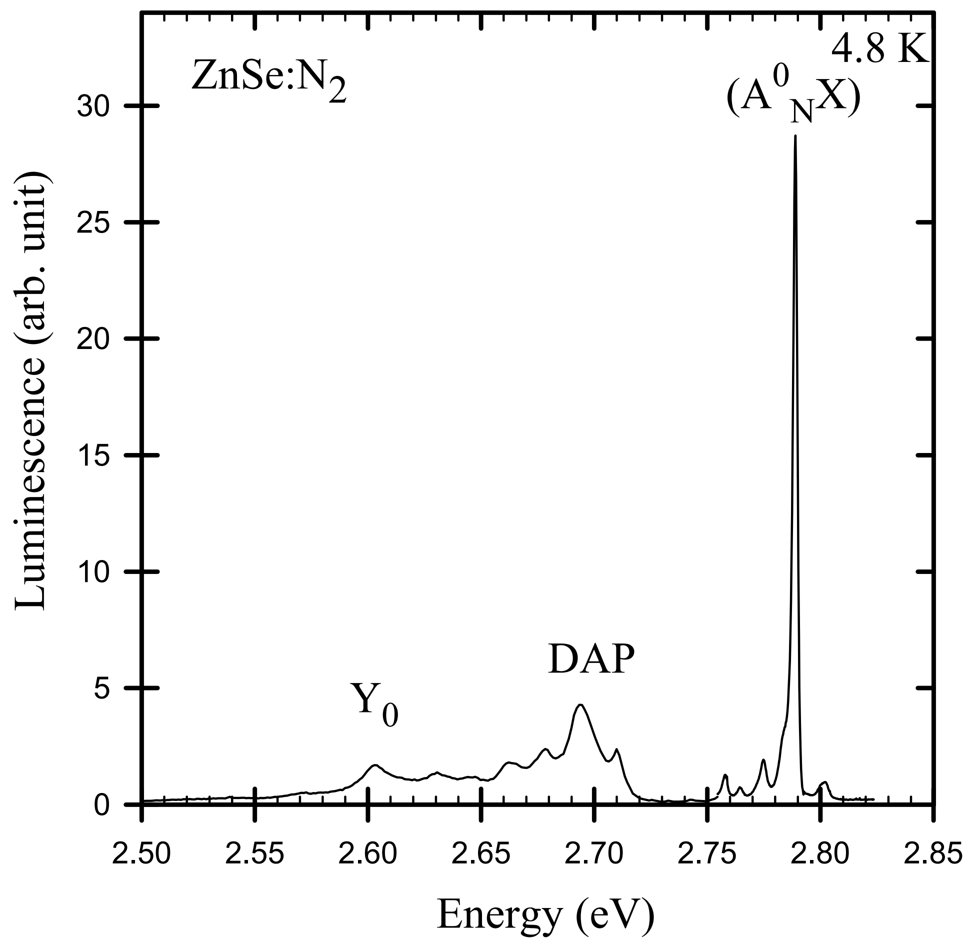

Fig. 4.8 Photoluminescence spectrum of ZnSe:N_2 at low-temperature. The strong nitrogen acceptor bound exciton and DAP feature indicate the nitrogen incorporation in the sample.

those of undoped ZnSe samples as shown in Fig. 4.7, again supporting that the room-temperature PL occurs due to intrinsic processes. Interestingly, all of our nitrogen-doped ZnSe samples grown using atomic nitrogen contain a high concentration of nitrogen even with the lowest plasma power and nitrogen flow. The only lightly-doped sample is the one grown using molecular nitrogen. Although p-type doping of ZnSe using molecular nitrogen was demonstrated, the doping concentration is low due to the poor "cracking efficiency" of molecular nitrogen.

For nitrogen-doped ZnSe grown under molecular hydrogen, the low-temperature PL spectrum is similar to those for nitrogen-doped ZnSe grown without hydrogen, consisting of a broad peak in the range of 2.5 to 2.65 eV (Fig. 4.6). Notice the SIMS results of the ZnSe:N,D_2 sample in Table 4.2, which has a nitrogen concentration of $8x10^{19}$ cm^{-3} and a deuterium concentration of $1x10^{18}$ cm^{-3}. The nitrogen incorporation rate appeared unaffected by the presence of molecular hydrogen, while the hydrogen incorporation was low in the molecular form. Therefore, it is not a surprise that the PL lineshape is similar to that of the ZnSe:N samples.

4.3.5 Hall Measurements

Room-temperature Hall measurements have been made on selected samples. Undoped ZnSe was found n-type with carrier concentrations ranging from $4x10^{10}$ cm^{-3} to $2x10^{12}$ cm^{-3} and mobilities ranging from 1600 cm^2 $V^{-1}s^{-1}$ to 70 cm^2 $V^{-1}s^{-1}$. The low carrier concentration and high mobility indicate a low impurity background in the undoped ZnSe grown by MBE. While normally In is used for the ohmic contact metal on undoped and n-type ZnSe, both In and Au (from $AuCl_3$) were tried for the ohmic contacts on undoped ZnSe samples. The measured carrier concentrations were about the same for both types of contacts, but the mobility measured using In contacts was about a factor of 20 larger than that using the Au contacts. All undoped ZnSe samples were very highly

resistive. For nitrogen-doped ZnSe samples, Au was tried first for the ohmic contacts, however, an ohmic contact can not be obtained, indicating that the contact metal normally used for narrow bandgap semiconductors is not suitable for wide bandgap semiconductors such as ZnSe. An alternative approach is to grow a thin layer of p-type ZnTe on top of the nitrogen-doped ZnSe, and use Au as the contact metal on the p-type ZnTe. About a 1/4 μm of nitrogen-doped ZnTe was deposited on the nitrogen-doped ZnSe, the ZnTe:N layer was then etched off in a 0.5% Br:Ethylene Glycol solution except in contact regions at sample corners. The ZnTe:N contact layer had a hole concentration of about $5x10^{19}$ cm^{-3} as measured by the Hall measurement in a 2μm thick nitrogen-doped ZnTe grown on GaAs substrate with the same growth conditions. Four nitrogen-doped ZnSe samples were chosen to grow a subsequent ZnTe:N layer and make the Au-ZnTe:N-ZnSe:N contact structure for Hall measurements. Three of those samples are ZnSe:N, and the other one is ZnSe:N,H. One of the ZnSe:N sample with a nitrogen concentration of $1.5x10^{19}$ cm^{-3} (from SIMS measurement) showed a p-type conductivity with free-hole concentration about $2x10^{16}$ cm^{-3}, mobility about 35 cm^2 V^{-1} s^{-1} and resistivity about 10 Ω-cm. The ZnSe:N,H sample using Au-ZnTe:N-ZnSe:N contact structure showed a non-ohmic contact and had a very noisy signal, while an n-type conductivity was found with carrier concentration about $1x10^{14}$ cm^{-3} and mobility about 75 cm^2 V^{-1} s^{-1} for one of the ZnSe:N,H sample using In contacts, indicating the hydrogen passivation of nitrogen in this type of samples.

4.4 Discussion

4.4.1 Hydrogen Incorporation in ZnSe

Hydrogen incorporation in nitrogen-doped ZnSe has been investigated by intentionally introducing hydrogen into MBE growth. Although hydrogen is not known to be a problem in nitrogen-doped ZnSe grown by conventional MBE as that occurred in

MOCVD,[33] MOVPE[104] and GSMBE,[34] the understanding of how hydrogen is incorporated in ZnSe is important to the processing of ZnSe-based material and devices by both MBE and other growth techniques. A summary of the measured results is given in the following paragraphs.

SIMS data shows that hydrogen concentration as high as $5x10^{20}$ cm^{-3} was present in nitrogen-doped ZnSe grown with atomic hydrogen samples (ZnSe:N,H). In contrast, the hydrogen concentration could not be measured in ZnSe:N grown without atomic hydrogen. In ZnSe:N,H samples, the hydrogen concentration was higher than the nitrogen concentration in the same layer, while in nitrogen-doped ZnSe grown with molecular hydrogen samples (ZnSe:N,H_2), the hydrogen level was significantly lower than the nitrogen level. The hydrogen incorporation clearly tracks nitrogen incorporation in ZnSe by SIMS depth profile. When deuterium was used, results similar to hydrogen were observed.

The PL spectra were different for ZnSe samples grown with and without atomic hydrogen. For nitrogen-doped ZnSe layers, those grown with atomic hydrogen featured a broad and deep level peak around 2.1 eV in the PL, while those grown without atomic hydrogen had the more typical PL consisting of a broad peak between 2.5 and 2.65 eV for heavily nitrogen-doped ZnSe. The feature at 2.1 eV in ZnSe:N,H has been speculated to be associated with hydrogen.[151] For undoped ZnSe layers, those grown with atomic hydrogen showed a strong line at 2.782 eV and a proposed DAP feature at 2.72 eV (Fig. 4.6), while those grown without atomic hydrogen were dominated by excitonic features. Though the features in ZnSe:H are not clearly identified yet, and the level of hydrogen could not be determined due to the detection limit in both SIMS and FTIR, the changes in the PL imply that hydrogen may indeed incorporate in the ZnSe:H samples.

FTIR spectroscopy is able to observe vibrational absorption bands related to hydrogen bonds. Features at 783 cm^{-1} and 3193 cm^{-1} were observed in ZnSe:N,H

samples and are associated to the local vibrational modes of N-H bond. These features are absent in other samples (ZnSe, ZnSe:N, ZnSe:H, ZnSe:N,H_2). Using isotopic deuterium to replace hydrogen, the isotopic shift in the vibrational frequency of N-H bond is predicted by the harmonic oscillator approximation. The observed absorption band at 2368 cm^{-1} agreed very well with the predicted band position for N-D bond, which led to the unambiguous confirmation of N-H bond formation in ZnSe.

Therefore, hydrogen incorporation in ZnSe occurs under certain conditions. The following properties are worth stressing:

(1) Hydrogen incorporation strongly relates to the nitrogen incorporation in ZnSe. In GSMBE[34] and MOCVD[33] grown nitrogen-doped ZnSe, hydrogen concentration tracks nitrogen concentration but both at the same level. In the MBE ZnSe grown with atomic hydrogen in this study, the hydrogen level is generally higher than the nitrogen level. This may imply that the hydrogen source we used in MBE is more effective in producing atomic hydrogen atoms. Note that hydrogen incorporation also increased with increasingly Zn-rich growth conditions while the GSMBE and MOCVD growth conditions may have actually occurred under highly Se-rich conditions.

(2) Hydrogen incorporation is significant only when both atomic hydrogen and atomic nitrogen are present during the growth of ZnSe. Both SIMS and FTIR measurements clearly indicate this property, which may not be easily seen from the MOCVD and GSMBE growth because of the hydrogen source is not unique and the contribution can not be solely determined. A recent study by Bourret-Courchesne[152] in organometallic vapor phase epitaxy (OMVPE) using non-hydrogen carrier gas indicates a significant reduction in hydrogen concentration compared to the use of hydrogen as a carrier gas.

(3) Nitrogen incorporation is not affected by hydrogen incorporation. This is supported by the fact that a high nitrogen concentration is observed in all ZnSe:N,H and

$ZnSe:N,H_2$ samples, which means that hydrogen will not compete with nitrogen for incorporation in ZnSe. While nitrogen is incorporated in a substitutional site, the smaller hydrogen will be in an interstitial site in the lattice. The observation of a substitutional nitrogen FTIR signal in both ZnSe:N and ZnSe:N,H samples supports the above proposition.

For hydrogen incorporation in nitrogen-doped ZnSe, it has been proposed that hydrogen could bond to nitrogen in either a center-bonding (CB) or anti-bonding (AB) site (Fig. 4.9), though the CB site might be more favorable.[(25,104)] This study cannot address this question. However, the close correspondence of the r-factor obtained from deuterium substitution with that of ammonia suggests that the hydrogen is fairly free to move and not strongly influenced by nearby atoms. This suggests the anti-bonding site.

If we notice that the hydrogen level was much higher than the nitrogen level in ZnSe:N,H samples, N-H bonding can not account for all hydrogen atoms in the layers. The excess hydrogen atoms in the films could be in other forms than N-H bond, such as:

(a) at interstitial site and bonding to a host atom;[(25,150)]

(b) at interstitial site and bonding to another impurity such as As or a vacancy;[(25)]

(c) an interstitial H_2 complex;[(25)]

(d) a complex with other impurity such as H_n-O and H_n-V.[(25)]

Those speculations are analogous to similar observations from other materials and not confirmed yet. Further investigation is needed to verify the origins of the excess hydrogen atoms in ZnSe. This could lead to a very interesting study if a combination of PL and magnetic resonance are used to investigate this phenomenon.

4.4.2 Nitrogen Compensation in ZnSe by Hydrogen

All doped ZnSe samples using atomic nitrogen as the doping source were heavily doped for a wide range of growth conditions. Generally, the nitrogen source was

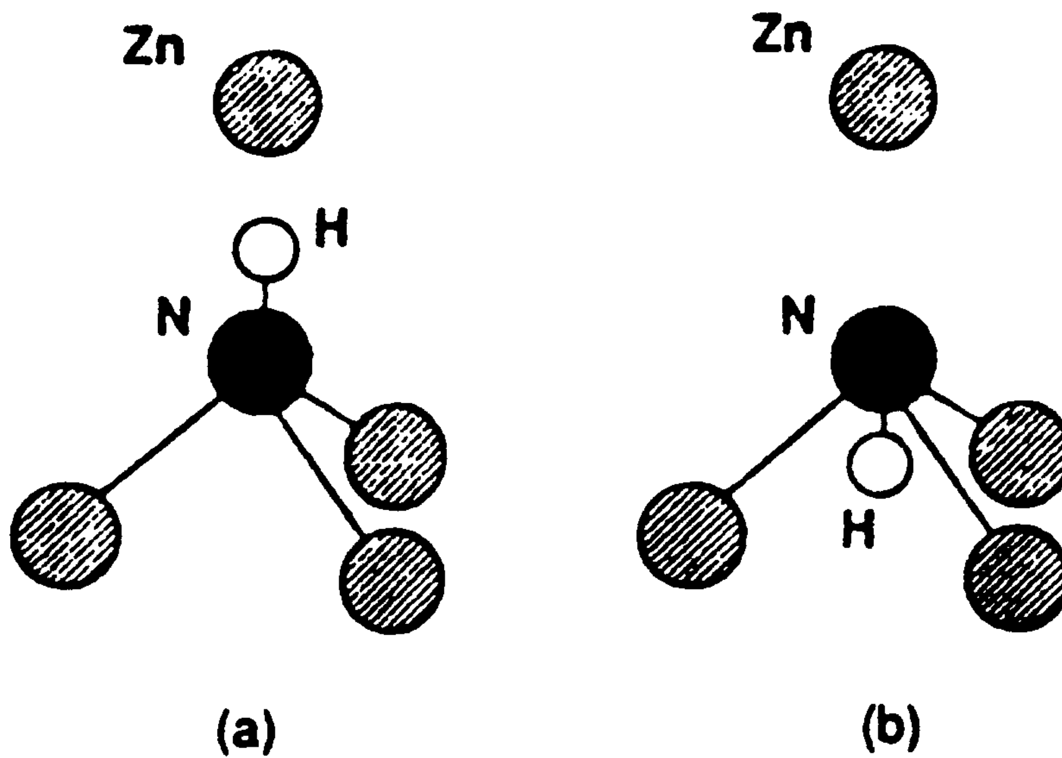

Fig. 4.9 Model of hydrogen bonding in ZnSe:N,H (a) center-bonding site, (b) anti-bonding site (Taken from Wolk *et al*.[(104)]).

operated at a plasma power range from 150 W to 300 W and a nitrogen flux BEP ranging from 1.5×10^{-6} to 5×10^{-6} Torr. Even with the lowest plasma power and nitrogen flux for which a plasma could be sustained, the resulting layer showed a very high nitrogen concentration as indicated by a PL spectrum indicative of heavily nitrogen-doped ZnSe. SIMS data shows the nitrogen concentration ranged from 4×10^{18} cm^{-3} to 8×10^{20} cm^{-3} in the doped samples (Table 4.2). Thus the rf plasma atomic/radical nitrogen source is very efficient for nitrogen incorporation into ZnSe. The nitrogen concentration is higher in samples grown with Zn-rich condition than that with Se-rich condition, while the growth rate changes in the reverse direction. This is similar to the results by planar-doping MBE of nitrogen-doped ZnSe.(153) With increasing either plasma power or nitrogen flow, nitrogen incorporation increases.

The heavily nitrogen-doped ZnSe films are highly compensated as confirmed by both PL and Hall measurements. In the quest of actual compensation mechanisms, optimization of existing growth procedures has not made significant progress in reducing compensation and increasing the hole concentration in ZnSe-based materials.(5,21) In this study, an independent hydrogen source was used to investigate the effect of hydrogen on the doping of nitrogen in ZnSe. Since a problem originated from the hydrogen passivation of nitrogen observed in MOCVD,(33) MOVPE,(104,152,154) and GSMBE(34) grown ZnSe, it is easy to come to the question of whether hydrogen plays any role in the nitrogen doping of ZnSe by MBE. Even though the hydrogen is in a background level of about 1×10^{-9} to 1×10^{-10} Torr partial pressure, it has been present as a problem in other material systems that hydrogen can compensate acceptors.(159) If the cracking efficiency is high, this level of hydrogen is sufficient to incorporate at levels of nitrogen in the 10^{17} - 10^{18} cm^{-3} range. This study indicates, however, that hydrogen incorporation is significant only when both atomic hydrogen and atomic nitrogen are present during growth. To examine the extent of hydrogen incorporation in a condition of conventional

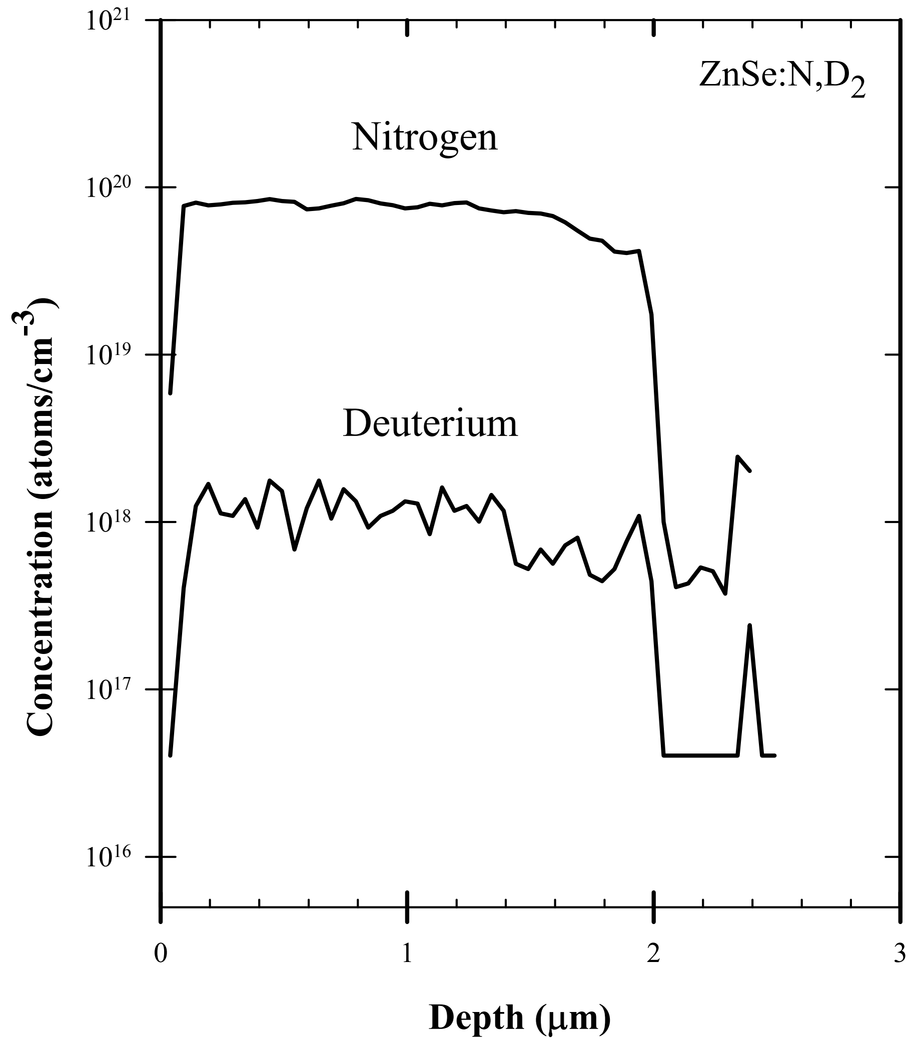

Fig. 4.10 Secondary ion mass spectrometry depth profile of ZnSe:N,D_2. The level of deuterium indicates that the hydrogen incorporation in molecular form is significantly lower than in atomic form.

MBE growth of ZnSe, a deuterium gas flow without thermal cracking was exposed to the ZnSe during nitrogen-doped growth. Because of high abundance of hydrogen, SIMS measurement sensitivity for hydrogen is poor. The use of the isotope deuterium to replace hydrogen increases the SIMS detection limit for hydrogen incorporation in ZnSe. A low "cracking efficiency" of molecular hydrogen was found with the actual hydrogen incorporation significantly lower than the nitrogen concentration.

Fig. 4.10 shows the SIMS depth profile of nitrogen and deuterium concentration for a nitrogen-doped ZnSe grown under a 10^{-6} Torr deuterium gas background ($ZnSe:N,D_2$). The nitrogen concentration was $8x10^{19}$ cm^{-3}, while the deuterium incorporation was about $1x10^{18}$ cm^{-3}. Compared to samples grown with atomic hydrogen (deuterium), where the hydrogen (deuterium) level was much higher than the nitrogen level in the same layer, the deuterium level was nearly 2 order lower than the nitrogen level in the $ZnSe:N,D_2$ sample, indicating that hydrogen incorporation is very low when it is in molecular form in the nitrogen-doped ZnSe growth. In a typical nitrogen doping growth of ZnSe by MBE, the hydrogen partial pressure in the background is about 10^{-10} Torr. If the incorporation is proportional to the amount of hydrogen molecules, the corresponding hydrogen concentration would be in a level of $1x10^{14}$ cm^{-3} by analog to the deuterium incorporation in $ZnSe:N,D_2$ sample. This level of hydrogen concentration would not be possible to contribute to the nitrogen compensation in a noticeable level. In conjunction with the PL spectrum of the $ZnSe:N,H_2$ ($ZnSe:N,D_2$) sample, which shows a feature of heavily nitrogen-doped ZnSe as shown in Fig. 4.5, and undetectable N-H (N-D) bond absorption by FTIR, it can be seen that the hydrogen passivation of nitrogen is insignificant in these layers. Thus, hydrogen is not a likely source of compensation in nitrogen-doped ZnSe grown by conventional MBE.

CHAPTER V

ADDITIONAL FTIR, PL AND EPR STUDIES: IMPLICATIONS FOR COMPENSATION PROCESSES

5.1 Evidence of Compensation Sources

5.1 Evidence of Compensation Sources

The previous sections have discussed evidence that compensation in nitrogen-doped ZnSe grown by MBE is not hydrogen-related, and occurs independent of twin-related defects. This chapter discusses additional studies made on the MBE grown ZnSe thin films. This evidence will help to clarify the mechanisms of this complicated process which has limited the p-type conductivity of ZnSe. FTIR measurement is consistent with nitrogen incorporation on a substitutional site, but further study indicates that not all nitrogen atoms are incorporated in equivalent sites at very high doping concentrations. PL measurements indicate the presence of a deep donor about 0.30 eV below the conduction band and the presence of a new local mode vibration tightly coupled to the deep-level related PL. EPR measurements are used to observe Se vacancy signals in both undoped and nitrogen-doped ZnSe samples, indicating that the Se vacancy occurs at a high enough density to be a compensating source, at least in a certain range of doping concentration.

5.1.1 FTIR Measurements

Analysis of ion channeling experiments is consistent with primarily substitutional nitrogen in heavily doped ZnSe, with no evidence of interstitials or significant lattice distortion.[88,97,98] Additionally, the observation of an FTIR absorption band with the characteristics appropriate for substitutional nitrogen has been reported for nitrogen that was ion implanted into ZnSe.[155] In this study, we have for the first time observed this

FTIR vibrational absorption band for substitutional nitrogen in nitrogen-doped ZnSe grown by MBE. Fig. 5.1 shows such spectra for samples of ZnSe:N, ZnSe:N and ZnSe:N,D, respectively. The absorption peak at 553 cm^{-1} corresponds to the vibrational mode for Zn-N bonding in the lattice based on the earlier observations in ion implanted ZnSe:N by Stein.[155]

Stein observed this absorption band in implanted ZnSe with a nitrogen concentration of about $5x10^{19}$ cm^{-3}, and attributed it to substitutional nitrogen in ZnSe through analysis of peak shifts with isotopic substitution between ^{14}N and ^{15}N.[155] The total cross-section of nitrogen atoms for absorption can be compared between Stein's samples and those of this study. The total cross-section of nitrogen atoms in the nitrogen implanted ZnSe layer was about $2x10^{15}$ cm^{-2} for the observed absorption peak intensity of 0.01 at 553 cm^{-1}.[155] The nitrogen cross-section in our MBE grown nitrogen-doped ZnSe layers is generally greater than $2x10^{15}$ cm^{-2}, indicating we should be able to observe this phenomenon. The observation of this band at a similar level is a direct evidence of substitutional nitrogen in nitrogen-doped ZnSe. While similar to the previously reported spectra, several significant differences exist. First, the full width at half maximum (FWHM) is a factor of two smaller for comparable nitrogen concentration. For example, Stein[155] quotes a FWHM of 15 cm^{-1} for a nitrogen concentration of ~ $5x10^{19}$ cm^{-3} while we observe a FWHM of 7 cm^{-1} for a concentration of $8x10^{19}$ cm^{-3} (Fig. 5.1(a)). This indicates that some residual damage may have remained in the ion-implanted samples. Additionally, Stein[155] observed additional N-related features at about 620 cm^{-1} which were absent from all ZnSe:N samples examined in the present study. However, a weak absorption band appears at about 620 cm^{-1} in ZnSe:N,H and ZnSe:N,D samples along with a concomitant decrease in the intensity of the 553 cm^{-1} band, as shown in Fig. 5.1(c). The decrease is consistent with N-H bond formation which would alter either the charge state or the local force constant for vibration at the nitrogen

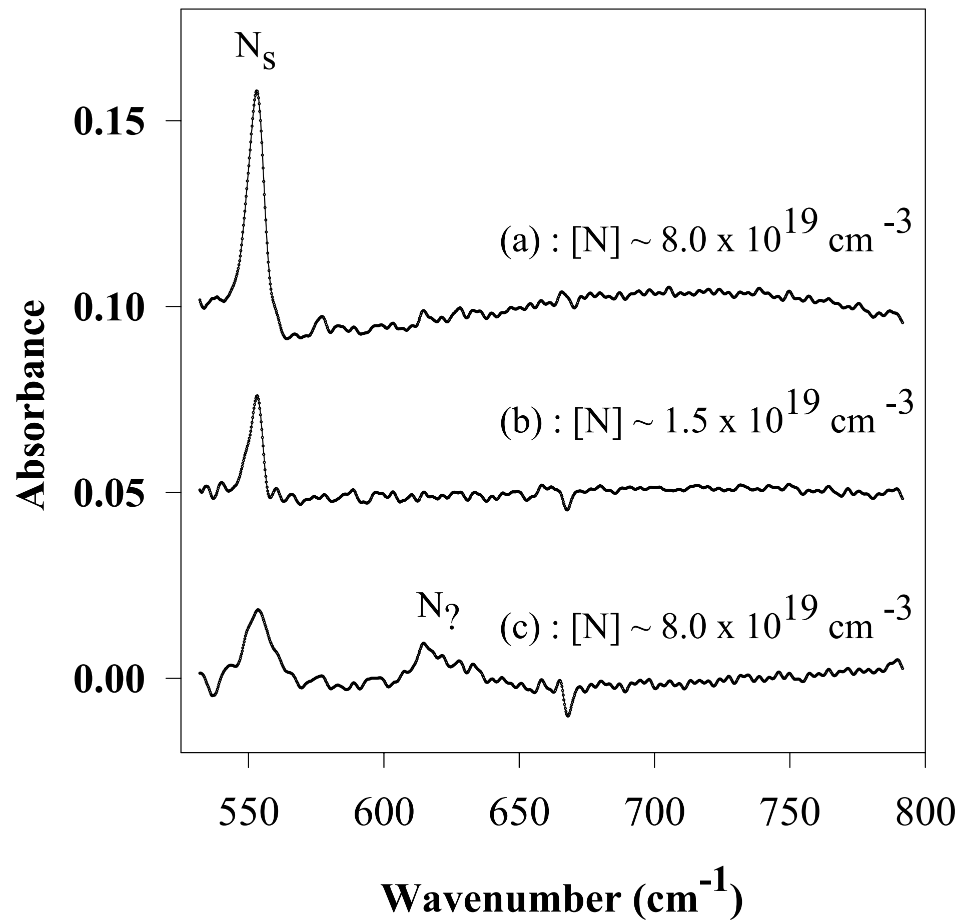

Fig. 5.1 Room-temperature FTIR spectrum of (a) ZnSe:N, (b) ZnSe:N and (c) ZnSe:N,D. Spectra are arbitrarily shifted along the absorbance axis for display.

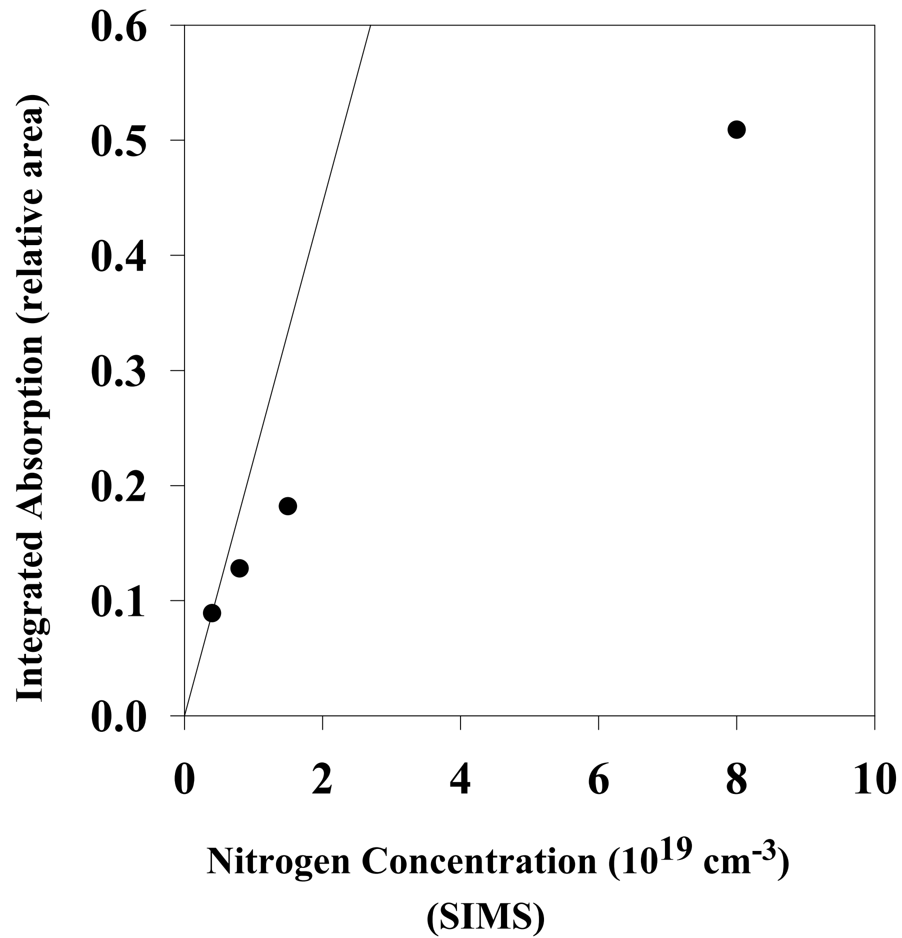

Fig. 5.2 Integrated absorption *vs.* nitrogen concentration in ZnSe:N. Dots represent experimental values while the line is a projection for a linear increase in integrated absorption as nitrogen concentration increases.

site. The absorption at 620 cm^{-1} may be associated with structural rearrangement around the nitrogen site, which could occur either due to the implantation process in the previous study[155] or due to lattice relaxation related to N-H bond formation.

Notice that the peak intensity at 2368 cm^{-1} of the N-D bond is about 0.004 (Fig. 4.4) in the ZnSe sample with a cross-section of $8x10^{15}$ atoms cm^{-2} of nitrogen and $3x10^{16}$ deuterium atoms cm^{-2}. It seems that contributions from each N-D oscillator to the absorption band is much less than that from a N-H oscillator (greater than factor of 5). This might explain why the N-D band was not observed from the N and D coimplanted ZnSe despite the high level of D concentration in Stein's study.[155]

Comparison of Fig. 5.1(a) and (b) indicate that the absorption band at 553 cm^{-1} increases with increasing nitrogen concentration. However, the relative increase in area under the absorption curve does not increase proportionate to the increase in nitrogen concentration. Based on the integrated area under the peak shown in Fig. 5.1(b), one would have expected the absorption peak shown in Fig. 5.1(a) to be approximately twice as large. Fig. 5.2 shows the integrated absorption *vs*. nitrogen concentration in the ZnSe:N layers. The nitrogen concentration was measured by SIMS, and the absorption has been normalized to take into account the sample thickness variations. The dots are experimental values, while the line is drawn to indicate the linear increase in integrated absorption expected to occur if all nitrogen atoms in the layer are in substitutional sites, passing through zero and the first data point. The nonlinear increase in the integrated absorption indicates that a significant proportion of the incorporated nitrogen may not occupy a substitutional site in very high nitrogen concentration ZnSe:N samples, or more likely, is in a different charge state such as would occur with defect complex formation.

5.1.2 PL Measurements

Detailed PL measurements have been made by M. Moldovan under the direction of Prof. Giles on the samples grown as part of this dissertation. Some of the results are included here in an attempt to develop a self-consistent picture of compensation. PL spectra of the heavily doped ZnSe show a broad emission peak in the range of 2.5 to 2.65 eV. Those features do not appear in PL spectra of low and medium doping level ZnSe:N where DAP emissions from both shallow and deep donors to nitrogen acceptors were observed.[85,87] The D^sAP emission at 2.696 eV is related to a shallow donor with an ionization energy of ~26 meV, and D^dAP at 2.677 is related to a deep donor with an ionization energy of ~46 meV.[87] However, these donors were not able to account for the transitions in the heavily nitrogen-doped ZnSe.[85,145] Although the broad feature in heavily nitrogen-doped ZnSe is significantly different from the DAP features normally observed in low-compensated ZnSe:N, it is still typically referred as DAP. Detailed investigation on the nature of this feature is limited.[145] Fig. 5.3 shows the PL spectra for a ZnSe:N sample with a nitrogen concentration of 1.5×10^{19} cm^{-3}. Curve (a) is the emission with above-bandgap light (325 nm) excitation at 4.8 K. The broad peak is composed of two components with center emission at 2.54 eV and 2.58 eV, respectively. Curve (b) is the emission with below bandgap (457 nm) excitation at 4.8 K. The high energy shoulder at 2.58 eV is now gone while the lower energy peak at 2.54 eV continues to be observed. This result, comparing PL with different excitation wavelengths suggests that the 2.58 eV peak actually originates from a shallow-donor to nitrogen-acceptor transition. The shallow donor, however, is not the same as the one with ionization energy of 26 meV in the lightly-doped ZnSe:N since this indicates a donor energy of about 110 meV. Curve (c) is the emission with below bandgap (457 nm) excitation at 85 K. The 2.54 eV peak is observed to shift to lower energy due to bandgap narrowing with temperate increasing. An enhanced first-order phonon replica of the 2.54 eV peak is

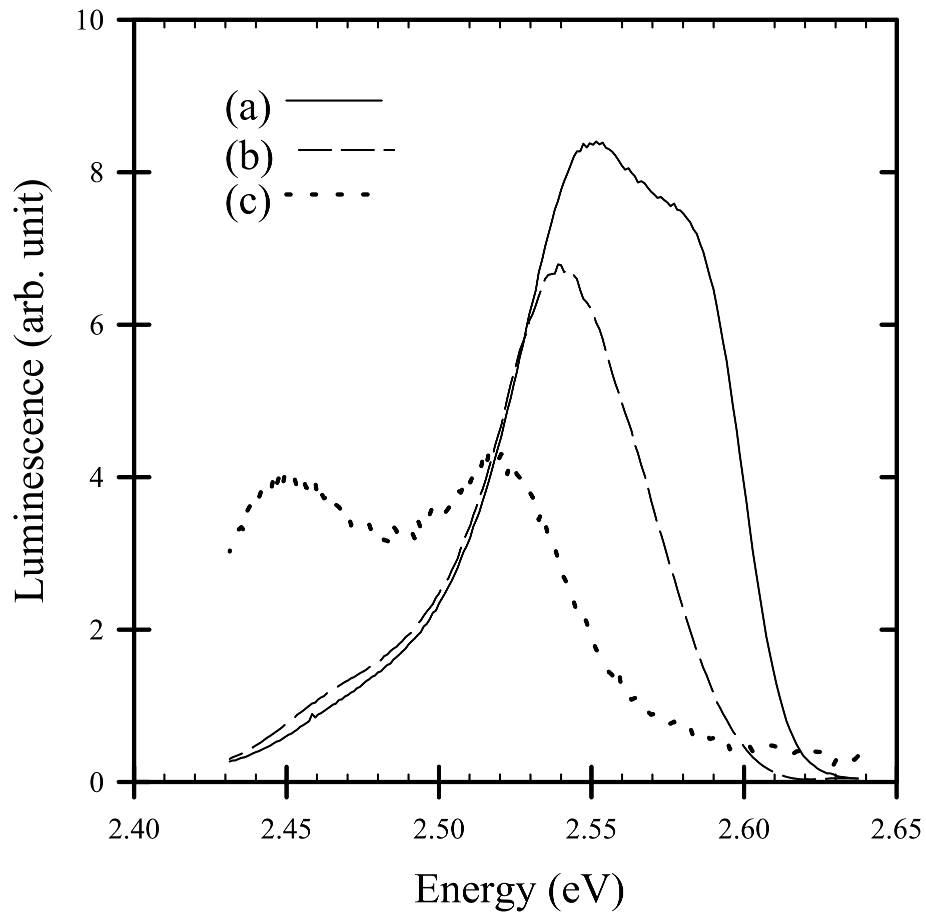

Fig. 5.3 Photoluminescence spectra of ZnSe:N for (a) above bandgap excitation (325 nm line) at 4.8 K, (b) below bandgap excitation (457 nm line) at 4.8 K and (c) below bandgap excitation (457 nm line) at 85 K.

also observed with a phonon energy about 70 meV, in contrast to the 32 meV of normally observed ZnSe phonon. The 2.54 eV peak, if it is the transition from a deep donor to the valence band, would relate to a deep donor at a level of about 0.3 eV below the conduction band.[163] The emission peak of the heavily-doped ZnSe:N shifts for samples with different nitrogen concentrations, indicating that the emission peak is doping-related. This observation could lead to the following speculations: (1) The nature of both shallow and deep donors are modified by the nitrogen concentration in the film in a form that the binding energy (or ionization energy) of the donors are effectively affected, which may need modifications of existing defect models; (2) The shallow and deep donors may still preserve their defect structures at high nitrogen concentration levels, however, lattice contraction and band perturbation[145] due to heavy doping will impose additional effects on the donors, which will in turn result in the change of their levels in the bandgap.

The investigation on the PL features of ZnSe:N samples, though preliminary, reveals that deep level defects may be involved in the compensation process in heavily nitrogen-doped ZnSe. The deep level defects could be related to vacancies, lattice distortions, or similar mechanisms which can effectively alter the localized states to the extent that a change in the phonon energy is observed. Further investigation on this structure will be reported by Moldovan *et al*.[164]

5.1.3 EPR Measurements

One of the popular defect models for nitrogen doping compensation in ZnSe is the donor complex (V_{Se}-Zn-N_{Se}) associated with a Se vacancy and substitutional nitrogen (Fig. 1.7).[13,97] A DAP of 2.678 eV has been attributed to this complex donor which corresponds a deep level of about 44 meV below the conduction band.[13] It is clear that high concentrations of nitrogen can be incorporated in ZnSe. Therefore, to compensate

nitrogen by a complex like V_{Se}-Zn-N_{Se}, a high concentration of Se vacancies must also exist. An ODMR signal was observed with a g=1.38, and was associated with the deep complex donor.(92) Se vacancy concentrations have been estimated indirectly by C-V measurement and PL changes due to vacancy diffusion over a period of time(156) and have not been measured directly in as-grown ZnSe layers.

Under the direction of Prof. Halliburton, S. Setzler used EPR to probe the Se vacancies in ZnSe. Fig. 5.4 shows the EPR spectra from four different ZnSe samples. Among the samples investigated, those grown under more Zn flux show the strongest EPR signal. Samples 9601 and 9602 are undoped ZnSe. Sample 9601 was grown with a Zn/Se ratio of about 0.46 while sample 9602 was grown with a Zn/Se ratio of about 0.63. Samples 9603 and 9609 are nitrogen-doped ZnSe. Sample 9603 was grown with a Zn/Se ratio of 0.494, which is slightly higher than that for sample 9609. An isotropic signal with $g \approx 2.0027$ was detected in both undoped (9602) and nitrogen-doped (9603) ZnSe samples. By analogy to the S vacancy in ZnS which has a g value of $g = 2.0034$,(158,165) this $g \approx 2.0027$ signal was assigned to the Se vacancy in ZnSe. The vacancy concentration was estimated to be ~ 2×10^{18} cm^{-3} in sample 9602, and ~ 7×10^{19} cm^{-3} in sample 9603.

Notice that in ODMR(92,93) and Raman(94) measurements, three signals were generally detected. While the g = 1.11 signal only appeared in lightly doped samples, the g = 1.38 and g = 2 peaks were observed in both low and high doping level samples. It seems that three types of donors are competing for the p-type compensation in nitrogen-doped ZnSe.(86) Interestingly, the strongest peak in ODMR measurements at 9.32 GHz was the g =2 signal, which is same as the g value of the EPR signal observed in this study. As the g = 1.38 donor has been attributed to the deep DAP of 2.678 eV and associated with the V_{Se}-Zn-N_{Se} complex, the g = 2 donor is attributed to a V_{Se}-impurity complex by Kennedy *et al.*(93) The complex is a single donor as a result of doubly

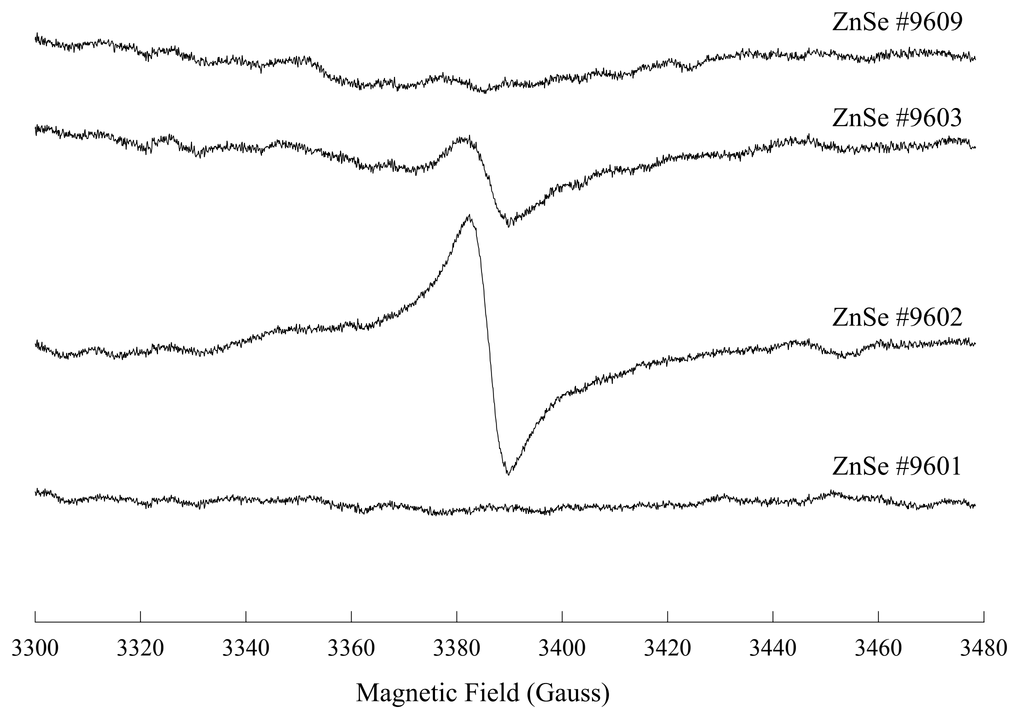

Fig. 5.4 Electron paramagnetic resonance signal of ZnSe samples. Samples 9601 and 9602 are undoped, while 9603 and 9609 are nitrogen-doped. The Se vacancies are estimated to be $2x10^{18}$ cm^{-3} and $7x10^{17}cm^{-3}$ in samples 9602 and 9603, respectively.

charged Se vacancy paired with a single acceptor such as Cu or Ag.[93] Since all singly charged Se vacancies can contribute to the EPR signal, EPR can not distinguish between isolated vacancies and vacancies which are part of a complex. The level of Se vacancies

in ZnSe, however, is very important in determining the compensation mechanism. Systematic investigations on a complete set of samples may give more useful trends.

5.2 Discussion of Compensation Processes in ZnSe

It has been shown above that levels of 10^{17} to 10^{18} cm^{-3} Se vacancies can occur in both undoped and nitrogen-doped ZnSe, and a significant amount of incorporated nitrogen does not incorporate in equivalent sites. The compensation mechanism in ZnSe is so complicated that no one convincing model can account for all aspects. One of the difficulties is due to the lack of direct data related to defect models. In this aspect, the results obtained from the as grown ZnSe layers by MBE is very useful and can be directly related to the compensation processes in ZnSe.

For the nitrogen related V_{Se}-Zn-N_{Se} model, a doubly charged V_{Se} combines with a next near neighboring substitutional nitrogen to form a singly charged complex, which acts as a single donor. Therefore, one such donor will compensate two nitrogen atoms in the net carrier concentration. The major source of compensation in this mechanism is the Se vacancy. With increasing Se vacancies, the compensation will increase if these vacancies are effectively activated in this process. Calculations based on vacancy models are not very successful in predicting p-type doping of ZnSe, mainly due to the fact that the estimation of vacancy levels is inaccurate.[86] If the Se vacancy level is in the range of 10^{17} to 10^{18} cm^{-3} as estimated according to the EPR measurement in this study, a p-type compensation will be in the low 10^{18} cm^{-3}. For a nitrogen doping concentration of 10^{18} to 10^{19} cm^{-3}, a hole concentration of 10^{17} to 10^{18} cm^{-3} is obtained.[75,86,88] As nitrogen concentration further increases, however, hole concentration saturates. The compensation due to Se vacancy complex would not be able to account for the level higher than 10^{18} cm^{-3}, since there are not enough Se vacancies to contribute to. Other compensating sources must dominate at the high doping level.

The lattice location of nitrogen atom in nitrogen-doped ZnSe has been studied using ion beam scattering.[88,97,98] It is found that nitrogen does locate in the substitutional site,[88,97] which is consistent with the observation of absorption band for substitutional nitrogen in FTIR measurements. A recent study using a combination of ion beam scattering and recoiling spectrometry techniques by Kubo[98] indicates that the optimal doped nitrogen atoms are located in the Se sites but excess nitrogen atoms locate in the interstitial sites. While the quantitative data of the substitutional and interstitial nitrogen in ZnSe:N samples is not available from these techniques, the correlation between the FTIR integrated absorbance of the substitutional nitrogen signal and the nitrogen concentration in the ZnSe:N layer (Fig. 5.2) provides strong evidence that nitrogen is in at least two inequivalent states at very high nitrogen concentration levels. The saturation of substitutional nitrogen signal implies that either nitrogen will not incorporate in the Se site or the nitrogen in Se site will not have its original localized properties in ZnSe:N. PL studies on ZnSe:N samples indicate that deep level defects exist and are the main source for the PL emissions in the very high doping level layers. The localized phonons exist in the heavily nitrogen-doped ZnSe that are significantly different from that of typically observed in ZnSe, indicating different lattice geometries for the lightly and heavily doped samples. This implies that nitrogen atoms at inequivalent sites perform differently in ZnSe.

A solubility theory was proposed to explain the difference in p-type doping of ZnSe and ZnTe.[100-102] It is found that p-type dopants (such as Li, Na, As and N) have much higher solubilities in ZnTe than in ZnSe.[101,102] The solubility of nitrogen in ZnSe is calculated to be $2x10^{19}$ cm^{-3} in ZnSe at a growth temperature of 250° by MBE.[101] Although the integrated absorbance of substitutional nitrogen signal in Fig. 5.2 is not able to estimate the number of net substitutional nitrogen atoms, it shows a characteristic of reaching nitrogen solubility limit as the nitrogen concentration increasing. One possible

solubility-limiting phase of nitrogen in ZnSe is the formation of Zn_3N_2, similar to the formation of Li_2Se for lithium doping in ZnSe.[102]

Based on results from FTIR, PL and EPR measurements, we suggest that the compensation process in nitrogen-doped ZnSe could result from different mechanisms at different doping levels. When nitrogen doping concentration is lower than 10^{18} cm^{-3}, Se vacancy related complex donor is the main compensating source, while at very high doping levels (greater than 10^{18} cm^{-3}), nitrogen solubility is the limiting effect on the p-type doping efficiency. Instead of "precipitating out", perhaps a second "phase" consisting of complexes, nitrogen-nitrogen pairing, different charge states of nitrogen, or nitrogen clustering is formed at the very high doping levels since nitrogen concentration above 10^{20} cm^{-3} can be easily achieved, which is much higher than the calculated solubility.[101] The second phase nitrogen is in sites not equivalent to substitutional site, resulting in the same phenomenon as compensation.

CHAPTER VI

CONCLUSIONS

In this study, ZnSe films were grown by MBE to investigate the effects of hydrogen and compensation processes. Through systematic growth and characterization of a variety of samples with different growth parameters, important results are obtained in reducing defect densities and understanding the hydrogen incorporation in ZnSe as well as the compensation process in nitrogen-doped ZnSe. To summarize,

(1) A significant reduction of micro-defects in both undoped and nitrogen-doped ZnSe was achieved using atomic hydrogen cleaning of GaAs substrate prior to ZnSe growth without any other treatment. The twin features defect density was less than 1×10^4 cm^{-2} in layers grown with atomic hydrogen cleaning, while it was greater than 1×10^7 cm^{-2} in layers grown with conventional thermal cleaning.

(2) Nitrogen-doped ZnSe films grown with atomic hydrogen cleaning and with conventional thermal cleaning are similar in photoluminescence emission feature, which is typical of heavily doped and highly compensated ZnSe:N. Therefore, p-type doping of ZnSe does not show much relation with the micro-defect density in the films, which implies that the nitrogen compensation in ZnSe is not related to this type of defect.

(3) Hydrogen incorporation in ZnSe was achieved using a thermally-cracked atomic hydrogen source. It is found that significant hydrogen incorporation occurred only when both atomic hydrogen and atomic nitrogen were present during growth. For other growth conditions, i.e., ZnSe:H, ZnSe:N,H_2, or ZnSe:N_2,H samples, hydrogen is found in a very low level of incorporation in ZnSe. Therefore, hydrogen incorporation in ZnSe is strongly nitrogen related.

(4) One mode of hydrogen incorporation was indicated by the observation of a vibrational absorption band for N-H bond in nitrogen-doped ZnSe grown with an atomic

hydrogen flux. Signals at 3193 cm^{-1} and 783 cm^{-1} of the absorption bands were assigned to N-H stretching mode and wagging mode, respectively. These results were observed for first the time in MBE grown ZnSe layers.

(5) Deuterium was used to replace hydrogen for the isotopic effect investigation. An absorption band at 2368 cm^{-1} was observed in nitrogen-doped ZnSe grown with an atomic deuterium flux. The isotope shift agreed with the prediction for N-D bond from a harmonic oscillator approximation, which was used to verify the formation of a vibrational bond. The results unambiguously identified that N-H bonding is occurring in the ZnSe:N,H samples.

(6) It is found that the incorporation of hydrogen was insignificant in nitrogen-doped ZnSe when it is in a molecular from. The hydrogen incorporation was estimated to be ~ 10^{14} cm^{-3} in a ZnSe:N layer grown by conventional MBE using a plasma atomic nitrogen source and high purity nitrogen gas. Therefore, the normally observed compensation in heavily nitrogen-doped ZnSe can not be caused by hydrogen.

(7) Substitutional nitrogen signal was first observed by FTIR in nitrogen-doped ZnSe layers grown by MBE. The increase in integrated absorbance, however, was not proportionate to the increase of nitrogen concentration in ZnSe. The discrepancy indicates that a very large amount of nitrogen was not in the substitutional sites in heavily doped ZnSe:N samples.

(8) PL of ZnSe:N samples is typical of heavily nitrogen-doped ZnSe with a broad feature ranging from 2.5 to 2.65 eV. A deep donor about 0.3 eV below the conduction band is proposed for the deep level PL according to PL measurements using different excitation wavelengths. Localized phonons with energies different from the typical ZnSe phonons were observed in ZnSe:N samples, indicating different lattice geometries in those samples.

(9) Se vacancy signal was observed by EPR in ZnSe with a g value of $g \approx 2$. The vacancy concentration was estimated to be in 10^{17} to 10^{18} cm^{-3} range. It is suggested that the compensation process in nitrogen-doped ZnSe was due to a Se vacancy related complex at doping levels less than 10^{18} cm^{-3}, and was dominated by the solubility limit of nitrogen in ZnSe at very high doping levels ($> 10^{18}$ cm^{-3}). Although mechanisms related to other defect models can not be ruled out, direct evidence for such has not been observed.

To conclude, atomic hydrogen has been demonstrated effective in cleaning GaAs substrate for the MBE growth of ZnSe. Micro-defect density lower than 10^4 cm^{-2} were obtained in both undoped and nitrogen-doped ZnSe using atomic hydrogen cleaning compared with that above 10^7 cm^{-2} using the conventional thermal cleaning. It is found that the reduction of micro-defects in nitrogen-doped ZnSe will not affect the compensation property. Hydrogen incorporation in ZnSe is strongly nitrogen-related and is significant only when both atomic hydrogen and atomic nitrogen are present. The hydrogen passivation of nitrogen in ZnSe occurred in other growth techniques is not observed during a conventional MBE growth. Therefore, the hydrogen background during a normal MBE growth of ZnSe will not introduce new compensating sources for nitrogen doping. Se vacancy concentration in ZnSe is estimated to be in a range between 10^{17} to 10^{18} cm^{-3} using EPR measurements, thus the defect model related to Se vacancy is supported for doping levels up to 10^{18} cm^{-3}. For very high doping level samples, not all nitrogen atoms are in equivalent substitutional sites. The discrepancy is the result of nitrogen solubility in ZnSe. A second phase may be formed where nitrogen complexes, nitrogen pairs, new charge states of nitrogen, or nitrogen clusters can occur at the very high doping levels. Thus, the compensation is dominated by the second phase form of nitrogen solubility in ZnSe.

REFERENCES

1. D. F. Shriver, P. Atkins, and C. H. Langford, Inorganic Chemistry, 2nd ed, New York: W. H. Freeman and Company, 1994.

2. M. Aven and J. S. Prener, editor, Physics and Chemistry of II-VI Compounds, Amsterdam: North-Holland Publishing Company, 1967.

3. R. L. Gunshor and A. V. Nurmikko, MRS Bulletin **20**, 15 (July 1995).

4. G. F. Neumark, R. M. Park, and J. M. DePuydt, Physics Today **47**, 26 (June 1994).

5. L. A. Kolodziejski, R. L. Gunshor, and A. V. Nurmikko, in Annu. Rev. Mater. Sci. **25**, 711 (1995).

6. R. L. Gunshor and A. V. Nurmikko, Laser Focus World, **31**, 97 (March 1995).

7. J. W. Cook Jr. and J. F. Schetzina, Laser Focus World, **31**, 101 (March 1995).

8. M. A. Metzger, Compound Semiconductors **1**, 26 (Jul/Aug 1995).

9. E. H. C. Parker, editor, The Technology and Physics of Molecular Beam Epitaxy, New York: Plenum Press, 1985.

10. R. L. Gunshor, L. A. Kolodziejski, A. V. Nurmikko, and N. Otsuka, in Semiconductors and Semimetals, vol **33**, edited by T. Pearsall, New York: Academic Press, 1990.

11. R. M Park, M. B. Troffer, C. M. Rouleau, J. M. DePuydt, and M. A. Haase, Appl. Phys. Lett. **57**, 2127 (1990).

12. K. Ohkawa, T. Karasawa, and O. Yamazaki, Jpn. J. Appl. Phys. **30**, L152 (1991).

13. I. S. Hauksson, J. Simpson, S. Y. Wang, K. A. Prior, and B. C. Cavenett, Appl. Phys. Lett. **61**, 2208 (1992).

14. D. B. Laks, C. G. Van de Walle, G. F. Neumark, and S. T. Pantelides, Phys. Rev. Lett. **66**, 648 (1991).

15. A. Garcia and J. E. Northrup, Phys. Rev. Lett. **74**, 1131 (1995).

16. D. J. Chadi and K. J. Chang, Appl. Phys. Lett. **55**, 575 (1989).

17. D. J. Chadi, Appl. Phys. Lett. **59**, 3589 (1991).

18. C. J. Park and D. J. Chadi, Phys. Rev. Lett. **75**, 1134 (1995).

19. D. J. Chadi, J. Cryst. Growth **138**, 295 (1994).

20. W. Xie, D. C. Grillo, R. L. Gunshor, M. Kobayashi, H. Jeon, J. Ding, A. V. Nurmikko, G. C. Hua, and N. Otsuka, Appl. Phys. Lett. **60**, 1999 (1992).

21. H. Luo and J. K. Furdyna, Semicond. Sci. Technol. **10**, 1041 (1995).

22. J. I. Pankove and N. M. Johnson, editor, Hydrogen in Semiconductors, Semiconductors and Semimetals, Vol **34**, Academic Press, 1991.

23. S. J. Pearton, J. W. Corbett, and M. Stavola, editor, Hydrogen in Crystalline Semiconductors, Springer Series in Materials Science **16**, Springer-Verlag, 1992.

24. B. Clerjaud, Physica B **170**, 383 (1991).

25. G. G. DeLeo, Physica B **170**, 295 (1991).

26. E. J. Petit and F. Houzay, J. Vac. Sci. Technol. B **12**, 547 (1994).

27. T. Sugaya and M. Kawabe, Jpn. J. Appl. Phys. **30**, L402 (1991).

28. M. Yamada, Y. Ide, and K. Tone, Jpn. J. Appl. Phys. **31**, L1157 (1992).

29. Y. Okada, T. Fujita, and M. Kawabe, Appl. Phys. Lett. **67**, 676 (1995).

30. H. Shimomura, Y. Okada, and M. Kawabe, Jpn. J. Appl. Phys. **31**, L628 (1992).

31. H. Shimomura, Y. Okada, H. Matsumoto, M. Kawabe, Y. Kitami, and Y. Bando, Jpn. J. Appl. Phys. **32**, 632 (1993).

32. Y. J. Chun, Y. Okada, and M. Kawabe, Jpn. J. Appl. Phys. **32**, L1085 (1993).

33. A. Kamata, H. Mitsuhashi, and H. Fujita, Appl. Phys. Lett., **63**, 3353 (1993).

34. E. Ho, P. A. Fisher, J. L. House, G. S. Petrich, L. A. Kolodziejski, J. Walker, and N. M. Johnson, Appl. Phys. Lett., **66**, 1062 (1995).

35. M.A. Haase, J. Qiu, J.M. DePuydt, and H. Cheng, Appl. Phys. Lett. **59**, 1272 (1991).

36. http://www.sony.co.jp/CorporateCruise/News/ and Compound Semiconductor **2**, 7 (Mar/Apr 1996).

37. J. M. Gaines, R. R. Drenten, K. W. Haberern, T. Marshall, P. Mensz, and J. Petruzzello, Appl. Phys. Lett. **62**, 2462 (1993).

38. R. M. Park and H. A. Mar, J. Mater. Res. **1**, 543 (1986).

39. R. M. Park, H. A. Mar, and J. Kleiman, J. Cryst. Growth **86**, 335 (1988).

40. N. Mino, M. Kobayashi, M. Konagai, and K. Takahashi, J. Appl. Phys. **58**, 793 (1985).

41. R. D. Bringans, D. K. Biegelsen, L. E. Swartz, F. A. Ponce, and J. C. Tramontana, Phys. Rev. B **45**, 13400 (1992).

42. L. T. Romano, R. D. Bringans, J. Knall, D. K. Biegelsen, A. Garcia, and J. E. Northrup, Phys. Rev. B **50**, 4416 (1994).

43. Y. Hishida, K. Yoneda, N. Matsunami, and N. Itoh, J. Appl. Phys. **62**, 4460 (1987).

44. M. H. Jeon, L. C. Calhoun, and R. M. Park, J. Electron. Mater. **24**, 177 (1995).

45. Z. Yu, D. B. Eason, C. Boney, J. Ren, W. C. Hughes, W. H. Rowland, Jr, J. W. Cook, Jr, and J. F. Schetzina, J. Vac. Sci. Technol. B **13**, 711 (1995).

46. D. B. Eason, Z. Yu, W. C. Hughes, C. Boney, J. W. Cook, Jr, J. F. Schetzina, D. R. Black, G. Cantwell, and W. C. Harsch, J. Vac. Sci. Technol. B **13**, 1566 (1995).

47. Z. Yu, C. Boney, W. C. Hughes, J. W. Cook, Jr, J. F. Schetzina, G. Cantwell, and W. C. Harsch, Electron. Lett. **31**, 1341 (1995).

48. G. Sato, T. Numai, M. Hoshiyama, I. Suemune, H. Machida, and N. Shimoyama, J. Cryst. Growth **150**, 734 (1995).

49. J. Suda, Y. Kawakami, Shizuo Fujito, and Shigeo Fujito, J. Cryst. Growth **150**, 738 (1995).

50. M. Imaizumi, Y. Endoh, K. Ohtsuka, and T. Isu, Jpn. J. Appl. Phys. **33**, 3505 (1994).

51. T. Ohtsuka, K. Horie, and N. Akiyama, J. Appl. Phys. **78**, 6006 (1995).

52. J. M. DePuydt, H. Cheng, J. E. Potts, T. L. Smith, and S. K. Mohapatra, J. Appl. Phys. **62**, 4756 (1987).

53. J. Lilja, J. Keskinen, M. Hovinen, and M. Pessa, J. Vac. Sci. Technol. B **7**, 593 (1989).

54. R. L. Gunshor, L. A. Kolodziejski, M. R. Melloch, M. Vaziri, C. Choi, and N. Otsuka, Appl. Phys. Lett. **50**, 200 (1987).

55. Zhonghai Yu, S. L. Buczkowski, N. C. Giles, and T. H. Myers, to appear in the July issue of Appl. Phys. Lett.

56. L. H. Kuo, L. Salamanca-Riba, B. J. Wu, G. Hofler, J. M. DePuydt, and H. Cheng, Appl. Phys. Lett. **67**, 3298 (1995).

57. S. Guha, H. Munekata, and L. L. Chang, J. Appl. Phys. **73**, 2294 (1993).

58. P. J. Parbrook, M. Ishikawa, Y. Nishikawa, S. Saito, M. Onomura, and G. Hatakoshi, J. Cryst. Growth **150**, 749 (1995).

59. Z. Zhu, T. Ebisutani, K. Takebayashi, K. Tanaka, and T. Yao, J. Cryst. Growth **138**, 397 (1994).

60. M. C. Tamargo, R. E. Nahory, B. J. Skromme, S. M. Shibli, A. L. Weaver, R. J. Martin, and H. H. Farrell, J. Cryst. Growth **111**, 741 (1991).

61. J. Qiu, Q. D. Qian, R. L. Gunshor, M. Kobayashi, D. R. Menke, D. Li, and N. Otsuka, Appl. Phys. Lett. **56**, 1272 (1990).

62. L. H. Kuo, K. Kimura, T. Yasuda, S. Miwa, C. G. Jin, K. Tanaka, and T. Yao, Appl. Phys. Lett. **68**, 2413 (1996).

63. D. Li, J. M. Gonsalves, N. Otsuka, J. Qiu, M. Kobayashi, and R. L. Gunshor, Appl. Phys. Lett. **57**, 449 (1990).

64. J. Qiu, D. R. Menke, M. Kobayashi, R. L. Gunshor, Q. D. Qian, D. Li, and N. Otsuka, J. Cryst. Growth **111**, 747 (1991).

65. J. F. Schetzina, Appl. Surf. Sci. **79/80**, 171 (1994).

66. M. Ohishi, H. Saito, H. Torihara, Y. Fujisaki, and K. Ohmori, J. Cryst. Growth **111**, 792 (1991).

67. N. Matsumura, T. Fukada, K. Senga, Y. Fukushima, and J. Saraie, J. Cryst. Growth **111**, 787 (1991).

68. S. Ichikawa, N. Matsumura, K. Yamawaki, K. Senga, and J. Saraie, J. Cryst. Growth **138**, 14 (1994).

69. J. Simpson, S. J. A. Adams, J. M. Wallace, K. A. Prior, and B. C. Cavenett, Semicond. Sci. Technol. **7**, 460 (1992).

70. D. A. Cammack, K. Shahzad, and T. Marschall, Appl. Phys. Lett. **56**, 845 (1990).

71. H. Cheng, J. M. DePuydt, M. A. Haase, and J. E. Potts, J. Vac. Sci. Technol. B **8**, 181 (1990).

72. M. Migita, A. Taike, and H. Yamamoto, J. Cryst. Growth **111**, 776 (1991).

73. K. Ohkawa, T. Mitsuyu, and O. Yamazaki, J. Appl. Phys. **62**, 3216 (1987).

74. J. M. DePuydt, H. Cheng, M. A. Haase, and J. E. Potts, Mat. Res. Soc. Symp. Proc. **161**, 97 (1990).

75. T. Yao and Z. Zhu, phys. stat. sol. (b) **187**, 387 (1995).

76. Z. Zhu, K. Takebayashi, and T. Yao, Jpn. J. Appl. Phys. **32**, 654 (1993).

77. M. A. Haase, H. Cheng, J. M. DePuydt, and J. E. Potts, J. Appl. Phys. Lett. **67**, 448 (1990).

78. S. M. Shibli, M. c. Tamargo, B. J. Skromme, S. A. Schwarz, C. L. Schwarz, R. E. Nahory, and R. J. Martin, J. Vac. Sci. Technol. B **8**, 187 (1990).

79. T. Yao and Y. Okada, Jpn. J. Appl. Phys. **25**, 821 (1986).

80. R. M. Park, H. A. Mar, and N. M. Salansky, J. Appl. Phys. **58**, 1047 (1985).

81. Y. Hishida, T. Yoshie, K. Yagi, K. Yodoshi, and T. Niina, Appl. Phys. Lett. **67**, 270 (1995).

82. R. P. Vaudo, J. W. Cook, Jr, and J. F. Schetzina, J. Cryst. Growth **138**, 430 (1994).

83. S. Ito, M. Ikeda, and K. Akimoto, Jpn. J. Appl. Phys. **31**, L1316 (1992).

84. Y. Kawakami, T. Ohnakado, M. Tsuka, S. Tokudera, Y. Ito, Sz. Fujita, and Sg. Fujita, J. Vac. Sci. Technol. B **11**, 2057 (1993).

85. J. Qiu, J. M. DePuydt, H. Cheng, and M. A. Haase, Appl. Phys. Lett. **59**, 2992 (1991).

86. K.A.Prior, Phys. Stat. Sol. (b) **187**, 379 (1995).

87. Z.Zhu, K.Takebayashi, K.Tanaka, T.Ebisutani, J. Kawamata, and T. Yao, Appl. Phys. Lett. **64**, 91 (1994).

88. E.Kurtz, S.Einfeldt, J.Nurnberger, S.Zerlauth, D.Hommel and G.Landwehr, Phys. Stat. Sol.(b),**187**, 393 (1995).

89. M. Karai, K. Kido, H. Naito, K. Kurosawa, and M. Okuda, J. Appl. Phys. **69**, 291 (1991).

90. Z. Zhu, G. D. Brownlie, P. J. Thompson, K. A. Prior, and B. C. Cavenett, Appl. Phys. Lett. **67**, 3762 (1995).

91. K. Ohkawa, A. Tsujimura, S. Hayashi, S. Yoshii, and T. Mitsuyu, Physica B **185**, 112 (1993).

92. B. N. Murdin, B. C. Cavenett, C. R. Pidgeon, J. Simpson, I. Hauksson, and K. A. Prior, Appl. Phys. Lett. **63**, 2411 (1993).

93. T. Kennedy, E. R. Glaser, B. N. Murdin, C. R. Pidgeon, K. A. Prior, and B. C. Cavenett, Appl. Phys. Lett. **65**, 1112 (1994).

94. P. J. Boyce, J. J. Davies, D. Wolverson, K. Ohkawa, and T. Mitsuyu, Appl. Phys. Lett. **65**, 2063 (1994).

95. J. J. Davices, D. Wolverson, and P. J. Boyce, phys. stat. sol. (b) **187**, 497 (1995).

96. J. Petruzzello, J. Gaines, P. van der Sluis, D. Olego, and C. Ponzoni, Appl. Phys. Lett. **62**, 1496 (1993).

97. T. Yao, T. Matsumoto, S. Sasaki, C. K. Chung, Z. Zhu, and F. Nishiyama, J. Cryst. Growth **138**, 290 (1994).

98. M. Kubo, J. Appl. Phys. **78**, 7088 (1995).

99. Y. Fan, J. Han, L. He, R. L. Gunshor, M. S. Brandt, J. Walker, N. M. Johnson, and A. V. Nurmikko, Appl. Phys. Lett. **65**, 1001 (1994).

100. Y. Fan, J. Han, R. L. Gunshor, J. Walker, N. M. Johnson, and A. V. Nurmikko, J. Electron. Mater. **24**, 131 (1995).

101. D. B. Laks, C. G. Van de Walle, G. F. Neumark, and S. T. Pantelides, Appl. Phys. Lett. **63**, 1375 (1993).

102. C. G. Van der Walle and D. B. Laks, Solid State Comm. **93**, 447 (1995).

103. J. M. DePuydt, M. A. Haase, H. Chang, and J. E. Potts, Appl. Phys. Lett. **55**, 1103 (1989).

104. J. A. Work, J. W. Ager III, K. J. Duxstad, E. E. Haller, N. R. Taskar, D. R. Dorman, and D. J. Olego, Appl. Phys. Lett., **63**, 2756 (1993).

105. S. Guha, J. M. DePuydt, M. A. Haase, J. Qiu, and H. Cheng, Appl. Phys. Lett. **63**, 3107 (1993).

106. S. Guha, H. Cheng, M. A. Haase, J. M. DePuydt, J. Qiu, B. J. Wu, and G. E. Hofler, Appl. Phys. Lett. **65**, 801 (1994).

107. G. C. Hua, N. Otsuka, D. C. Grillo, Y. Fan, J. Han, M. D. Ringle, R. L. Gunshor, M. Hovinen, and A. V. Nurmikko, Appl. Phys. Lett. **65**, 1331 (1994).

108. M. Hovinen, J. Ding, A. V. Nurmikko, G. C. Hua, D. C. Grillo, L. He, J. Han, and R. L. Gunshor, Appl. Phys. Lett. **66**, 2013 (1995).

109. G. D. U'Ren, G. M. Haugen, P. F. Baude, M. A. Haase, K. K. Law, T. J. Miller, and B. J. Wu, Appl. Phys. Lett. **67**, 3862 (1995).

110. H. T. Lin, D. H. Rich, and D. B. Wittry, J. Appl. Phys. **75**, 8080 (1994).

111. G. M. Williams, A. G. Gullis, K. Prior, J. Simpson, B. C. Cavenett, and S. J. Adams, Inst. Phys. Conf. Ser. **134**, 671 (1993).

112. J. Tanimura, O. Wada, T. Ogama, Y. Endoh, and M. Imaizumi, J. Appl. Phys. **77**, 6223 (1995).

113. G. C. Hua, D. C. Grillo, T. B. Ng, C. C. Chu, J. Han, R. L. Gunshor, and A. V. Nurmikko, J. Electron. Mater. **25**, 263 (1996).

114. L. H. Kuo, L. Salamanca-Riba, J. M. DePuydt, H. Cheng, and J. Qiu, Appl. Phys. Lett. **63**, 3197 (1993).

115. Y. Qiu, A. Osinsky, A. A. El-Emawy, E. littlefield, H. Temkin, and N. Faleev, J. Appl. Phys. **79**, 1164 (1996).

116. L. H. Kuo, L. Salamanca-Riba, J. M. DePuydt, H. Cheng, and J. Qiu, J. Electron. Mater. **23**, 275 (1994).

117. Y. Fan, J. Han, L. He, J. Saraie, and R. L. Gunshor, Appl. Phys. Lett. **61**, 3160 (1992).

118. Y. Lansari, J. Ren, B. Sneed, K. A. Bowers, J. W. Cook, and J. F. Schetzina, Appl. Phys. Lett. **61**, 2554 (1992).

119. Z. Yang and J. F. Schetzina, J. Electron. Mater. **23**, 1071 (1994).

120. C. T. Walker, J. DePuydt, M. Haase, J. Qiu, and H. Cheng, Phys. B **185**, 27 (1993).

121. M. Onomura, M. Ishikawa, Y. Nishikawa, S. Saito, P. J. Parbrook, et al, Electron. Lett. **29**, 2114 (1993).

122. Basic Vacuum Pratice, 3rd, Varian Associates, Inc. (Lexington, MA), 1989

123. Atomic/Radical Beam Source, Model CARS25, Operating and Service Mnual, Oxford Applied Research Ltd., March 1994.

124. Atomic Hydrogen Source: User's Guide, EPI (Minneapolis, MN), February 1995; EPI Application Note, August/September, 1994.

125. M. G. Legally and D. E. Savage, MRS Bulletin **18**, 24 (Jan. 1993).

126. B. E. Warren, X-ray Diffraction, New York: Dover Publications, Inc., 1990.

127. P. K. Larsen and P. J. Dobson, editor, Reflection High-Energy Electron Diffraction and Reflection Electron Imaging of Surfaces, Plenum Press, 1987.

128. KSA RHEED 300: User Manual, k-Space Associates, Inc. (Ann Arbor, MI), 1994.

129. UTI Model 100C Precision Mass Analyzer Operating and Service Manual, UTI Instruments Company, 1990.

130. S. Perkowitz, D. G. Seiler, and W. M. Duncan, J. Res. Natl. Inst. Stand. Technol. **99**, 605 (1994).

131. B. J. Skromme, Annu. Rev. Mater. Sci. **25**, 601 (1995).

132. Y. Zhang, W. Liu, B. J. Skromme, H. Cheng, S. M. Shibli, M.C. Tamargo, J. Cryst. Growth **138**, 310 (1994).

133. S. M. Sze. Physics of Semiconductor Devices, 2nd, John Wiley & Sons, 1981.

134. D. Rugar and P. Hansma, Physics Today **43**, 23 (October, 1990).

135. C. M. Rouleau and R. M. Park, J. Appl. Phys. **73**, 4610 (1993).

136. S. V. Hattangady, R. A. Rudder, M. J. Mantini, G. G. Fountain, J. B. Posthill, and R. J. Markunas, J. Appl. Phys. **68**, 1233 (1990).

137. N. Kondo and Y. Nanishi, Jpn. J. Appl. Phys. **28**, L7 (1989).

138. Y. Luo, D. A. Slater, and R. M. Osgood, Jr., Appl. Phys. Lett. **67**, 55 (1995).

139. D. Kinosky, R. Qian, A. Mahajan, S. Thomas, P. Munguia, J. Fretwell, S. Banerjee, and A. Tasch, Mat. Res. Soc. Symp. Proc. **315**, 219 (1993).

140. B. J. Wu, G. M. Haugen, J. M. DePuydt, L. H. Kuo, and L. Salamanca-Riba, Appl. Phys. Lett. **68**, 2828 (1996).

141. R. Ruppert, D. Hommel, T. Behr, H. Heinke, A. Waag, and G. Landwehr, J. Cryst. Growth **138**, 48 (1994).

142. K. Shahzad, J. Petruzzello, D. J. Olego, D. A. Cammack, and J. M. Gaines, Appl. Phys. Lett. **57**, 2452 (1990).

143. S. Myhajlenko, J. L. Batstone, H. J. Hutchinson, and J. W. Steeds, J. Phys. C: Solid States Phys. **17**, 6477 (1984).

144. K. Shahzad, D. J. Olego, and D. A. Cammack, Phys. Rev. B **39**, 13016 (1989).

145. C. Kothandaraman, G. F. Neumark, and R. M. Park, Appl. Phys. Lett. **67**, 3307 (1995).

146. Zhonghai Yu, S. L. Buczkowski, M. C. Petcu, N. C. Giles, and T. H. Myers, Appl. Phys. Lett. **68**, 529 (1996).

147. see Ref. 104 and the references there in.

148. B. Pajot, B. Clerjaud, and J. Chevallier, Physica B **170**, 371 (1991).

149. J. Neugebauer and C. G. Van de Walle, Appl. Phys. Lett. **68**, 1829 (1996).

150. J. Tatarkiewicz, A. Breitschwerdt, A. M. Witowski, and H. Hartmann, Solid State Comm., **68**, 1081 (1988).

151. K. Ohkawa, T. Karasawa, and T. Mitsuyu, J. Cryst. Growth **111**, 797 (1991).

152. E. D. Bourret-Courchesne, Appl. Phys. Lett. **68**, 2418 (1996).

153. S. Matsumoto, H. Tosaka, T. Yoshida, M. Kobayashi, and A. Yoshikawa, Jpn. J. Appl. Phys. **32**, L229 (1992).

154. K. Nishimura, Y. Nagao, and K. Sakai, J. Cryst. Growth **138**, 114 (1994).

155. H. J. Stein, Appl. Phys. Lett. **64**, 1520 (1994).

156. K. A. Prior, B. Murdin, C. R. Pidgeon, S. Y. Wang, I. Hauksson, J. T. Mullins, G. Horsburgh, and B. C. Cavenett, J. Cryst. Growth **138**, 94 (1994).

157. J. A. Weil, J. R. Bolton, and J. E. Wertz, Electron Paramagenic Resonance: Elementary Theory and Practical Applications, New York: John Wiley & Sons, Inc., 1994.

158. J. W. Allen, Semicond. Sci. Technol. **10**, 1049 (1995).

159. M. S. Brandt, J. W. Ager III, W. Gotz, N. M. Johnson, J. S. Harris, Jr., R. J. Molnar and T. D. Moustakas, Phys. Rev. B **49**, 14758 (1994).

160. J. Ren, K. A. Bowers, S. Hwang, J. W. Cook, and J. F. Schetzina, J. Cryst. Growth **111**, 772 (1991).

161. H. Cheng, J. M. DePuydt, J. E. Potts, and T. L. Smith, Appl. Phys. Lett. **52**, 147 (1988).

162. K. Ohkawa, T. Mitsuyu, J. Appl. Phys. **70**, 439 (1991).

163. Zhonghai Yu, S. L. Buczkowski, M. Moldovan, N. C, Giles, and T. H. Myers, Sixth Conference on Computational Research on Materials, Morgantown, WV (May, 1996).

164. M. Moldovan, N. C. Giles, L. E. Halliburton, S. Setzler, T. H. Myers, and Zhonghai Yu, MRS 1996 Fall Meeting, Boston, MA, (1996).

165. J. Schneidr and A. Rauber, Solid State Commun. **5**, 779 (1967).

166. N. C. Giles, Jaesun Lee, T. H. Myers, Zhonghai Yu, B. K. Wagner, R. G. Benz II, and C. J. Summers, J. Electron. Mater. **24**, 691 (1995).

167. Zhonghai Yu, S. G. Hofer, N. C. Giles, T. H. Myers, and C. J. Summers, Phys. Rev. B **51**, 13789 (1995).

168 K. Diels and R. Jaeckel, Leybold Vacuum Handbook, Pergamon Press, (Oxford) 1996.

169 G. L. Weissler and R. W. Carlson, editor, Vacuum Physics and Technology, Vol 14, Academic Press, (New York) 1979.